

Lane and Road Marking Detection with a High Resolution Automotive Radar for Automated Driving

Zur Erlangung des akademischen Grades eines

DOKTOR-INGENIEURS

von der KIT-Fakultät für
Elektrotechnik und Informationstechnik,
des Karlsruher Instituts für Technologie

genehmigte

DISSERTATION

von

M.Sc. Zhaofei Feng

geb. in Zhejiang, China

Tag der mündlichen Prüfung:

30.07.2019

Hauptreferent: Prof. Dr.-Ing. Dr.h.c. Dr.-Ing. E.h. mult. Werner Wiesbeck

Korreferent: Prof. Dr.-Ing. Wolfgang Menzel

Abstract

The automotive industry is currently undergoing an unprecedented revolution, and the advanced driver assistance and automated driving technologies are the most influencing factors that are pushing this transformation forward. Automated driving system consists mainly of three steps: environmental perception, route planning, and driving action. As the first stage of the whole system, the perception step that extracts relevant information from the driving environment, plays an essential role for the subsequent stages and the whole system performance. With a good perception, the vehicle is able to accomplish functions like Adaptive Cruise Control, Automatic Emergency Braking, Lane Change Assist, etc. For the lane-related functions, the video camera sensors are mainly employed in most of the production vehicles nowadays. However, such sensor works reliably only under optimal lighting conditions. When the vehicle encounters a scenario with a sudden change of the lighting strength, a low illuminated environment, or limited visibility, such video sensors may be blinded. To complement the shortcomings of the video camera sensors, this dissertation tries to find out the feasibility of lane detection with automotive radar sensor—a sensor that is not influenced by any lighting conditions and is already massively equipped in production vehicles. To detect the lanes, the road marking painted with color is an important component for video camera sensors. However, such road markings are not able to provide sufficient reflection power to the radar sensors, indicating that an appropriate modification of such road marking is necessary in order to be able to detect them with radar sensors. To accomplish this task, this dissertation aims to analyze the scattering properties of various radar reflectors, both with simulation and on-road measurements, and to propose the most suitable reflector type that can be integrated into the road marking or the road. As machine learning enables the vehicle to understand the environment with image-like data collected by video camera sensors, this dissertation proves the capability and potential of such methods for radar data, especially for radar-based lane determination.

Zusammenfassung

Die Automobilindustrie erlebt gerade einen beispiellosen Wandel, und die Fahrerassistenz und das automatisierte Fahren spielen dabei eine entscheidende Rolle. Automatisiertes Fahren System umfasst hauptsächlich drei Schritte: Wahrnehmung und Modellierung der Umgebung, Fahrtrichtungsplanung, und Fahrzeugsteuerung. Mit einer guten Wahrnehmung und Modellierung der Umgebung kann ein Fahrzeug Funktionen wie intelligenter Tempomat, Notbremsassistent, Spurwechselassistent, usw. erfolgreich durchführen. Für Fahrfunktionen, die die Fahrspuren erkennen müssen, werden gegenwärtig ausnahmslos Kamerasensoren eingesetzt. Bei wechselnden Lichtverhältnissen, unzureichender Beleuchtung oder bei Sichtbehinderungen z.B. durch Nebel können Videokameras aber empfindlich gestört werden. Um diese Nachteile auszugleichen, wird in dieser Doktorarbeit eine „Radar-taugliche“ Fahrbahnmarkierungserkennung entwickelt, mit der das Fahrzeug die Fahrspuren bei allen Lichtverhältnissen erkennen kann. Dazu können bereits im Fahrzeug verbaut Radare eingesetzt werden. Die heutigen Fahrbahnmarkierungen können mit Kamerasensoren sehr gut erfasst werden. Wegen unzureichender Rückstreueigenschaften der existierenden Fahrbahnmarkierungen für Radarwellen werden diese vom Radar nicht erkannt. Um dies zu bewerkstelligen, werden in dieser Arbeit die Rückstreueigenschaften von verschiedenen Reflektortypen, sowohl durch Simulationen als auch mit praktischen Messungen, untersucht und ein Reflektortyp vorgeschlagen, der zur Verarbeitung in heutige Fahrbahnmarkierungen oder sogar für direkten Verbau in der Fahrbahn geeignet ist. Ein weiterer Schwerpunkt dieser Doktorarbeit ist der Einsatz von Künstliche Intelligenz (KI), um die Fahrspuren auch mit Radar zu detektieren und zu klassifizieren. Die aufgenommenen Radardaten werden mittels semantischer Segmentierung analysiert und Fahrspurverläufe sowie Freiflächenerkennung detektiert. Gleichzeitig wird das Potential von KI-tauglichen Umgebungsverstehen mit bildgebenden Radardaten aufgezeigt.

Vorwort

Die vorliegende Arbeit entstand während meiner Zeit als Doktorand bei der Robert Bosch GmbH am Standort Leonberg in Kooperation mit dem Institut für Hochfrequenztechnik und Elektronik (IHE) des Karlsruher Instituts für Technologie (KIT). Hiermit möchte ich meinen besonderen Dank nachstehenden Personen entgegen bringen, ohne deren Mithilfe die Anfertigung dieser Promotionsarbeit niemals zustande gekommen wäre:

Mein besonderer Dank gilt zunächst meinem Doktorvater am IHE, Herrn Prof. Dr.-Ing. Dr.h.c. Dr.-Ing. E.h. mult. Werner Wiesbeck, der diese Arbeit wissenschaftlich betreut hat und mich durch seine fachliche Unterstützung, seine hilfreichen Ideen und außerordentliche Radarkompetenz immer zielgerichtet bei meinen Ausarbeitungen geleitet hat. Für den zugesprochenen Freiraum in der Ausgestaltung meiner Forschungsaktivitäten und die sehr freundliche Zusammenarbeit möchte ich mich herzlich bedanken.

Mein außerordentlicher Dank gilt auch meinem Betreuer bei der Robert Bosch GmbH, Herrn Dr.-Ing. Martin Kunert, der dieses neue und interessante Thema zusammen mit mir erschlossen hat und mir bei meinen Analysen, Untersuchungen und Messungen mit Rat und Tat zur Seite stand. Vielen Dank für diese einmalige Chance, in diesem aufregenden und interessanten Forschungsgebiet tätig zu sein.

Des Weiteren möchte ich mich bei Herrn Frank Meinl und Dr.-Ing. Eugen Schubert für die fachliche Unterstützung bedanken. Ohne deren mühevollen Geduld und Hilfe wäre diese Arbeit niemals gelungen.

Tief verbunden und dankbar bin ich auch meinen Kollegen, Martin Stolz und Mingkang Li, für ihre außerordentlich hilfreiche Unterstützung und sehr gute Zusammenarbeit.

Mein besonderer Dank geht auch an meine Eltern, die mir meine Arbeit in dieser Form ermöglicht haben und meine Entscheidungen immer unterstützt haben.

Leonberg, im Februar 2019
Zhaofei Feng

Contents

Abstract	i
Zusammenfassung	iii
Vorwort	v
Acronyms and Symbols	xi
1 Introduction	1
1.1 Motivation	1
1.2 State of the Art Technology	2
1.3 Goal and Methodology	4
1.4 Summary of the Goals of this Thesis	5
2 FMCW Radar	7
2.1 Concept of FMCW Radar	7
2.2 Raw Data Processing	8
2.2.1 Range of the Target	9
2.2.2 Velocity of the Target	13
2.2.3 CFAR Processing	15
2.2.4 Direction of Arrival (DOA): Maximum Likelihood Estimation	18
2.3 Summary	21
3 Radar Cross Section and Radar Reflectors	23
3.1 Radar Cross Section	23
3.1.1 Definition	23
3.1.2 Minimum Required Radar Cross Section	24

3.2	Radar Cross Section Dependencies: Influences, Effects, and Comparison of Typical and Relevant Targets	28
3.2.1	Spheres	28
3.2.2	Cylinder, Dihedral, and Symmetrical Trihedral	32
3.2.3	Other Promising Technologies	34
3.3	In-depth Reflector Analysis for Lane Detection with Automotive Radar	34
3.3.1	Particularity of Elevation Angle α with an Automotive Radar for Road Marking Detection	34
3.3.2	Symmetrical and Asymmetrical Trihedral (Type 1)	35
3.3.3	Influence of Signal Polarization on RCS	37
3.3.4	Asymmetrical Trihedral with Slanted Plates (Type 2)	39
3.3.5	Comparison Between Asymmetrical Reflector and Other Reflectors	41
3.4	Mounting Position of Automotive Radar for Lane Detection	41
3.4.1	Radar Mounting Height	42
3.4.2	Radar Mounting Orientation	45
3.5	Influence of Road Curve on RCS	47
3.5.1	Vertical Road Curve	47
3.5.2	Horizontal Road Curve	49
3.6	Dynamic Simulation of Radar-detectable Road Markings	50
3.6.1	Lateral Localization of the Vehicle	51
3.6.2	Determination of the Vehicle's Orientation	53
3.6.3	Oncoming Horizontal Road Curve	53
3.6.4	Summary	54
4	Radar Road Marking Reflection Measurements on Test Tracks	55
4.1	Measurement Setup and General Considerations	55
4.1.1	Samples under Measurement	55
4.1.2	Measurement Setup and Procedure	56
4.2	Evaluation of Measurement Results	57
4.2.1	Repeatability of the Measurements	57
4.2.2	Type 1	59
4.2.3	Type 1 and Type 3	61

4.2.4	Type 1 and Type 4	62
4.2.5	Reflector with Covering	63
4.2.6	Other Types	65
4.2.7	Summary	67
4.3	Deployment of Dedicated Radar Reflectors on the Road . . .	71
4.3.1	Single Shot Measurements	71
4.3.2	Radar Road Signature - a Radar Based Map for Accu- rate Localization	73
4.3.3	Roadside Construction Considerations	74
4.3.4	Encoding of Radar Road Markings	75
4.3.5	Guard Rails and Other Existing Roadside Infrastructure	76
4.4	Summary	77
5	Clustering and Classification of Radar-detectable Roadside Landmarks for Lane Course and Lane Border Determination	79
5.1	Clustering	79
5.1.1	Static Point Extraction	80
5.1.2	Distance Based Clustering	81
5.1.3	Spatial Distribution Characteristic of the Reflection Points - the Point Pattern	84
5.1.4	Traverse all Possible Paths	85
5.1.5	Utilize Reflection Magnitude to Increase the Cluste- ring Reliability	87
5.1.6	Summary	88
5.2	Pixel-wise Lane Segmentation with Neural Networks	88
5.2.1	Basics of Deep Learning - Steps Towards Semantic Segmentation	89
5.2.2	Deep Learning Framework	95
5.2.3	Grid Segmentation Neural Network Architecture . .	95
5.2.4	Input Dataset Preparation	97
5.2.5	Evaluation Metrics	99
5.2.6	Training Parameters	101
5.2.7	Guard Rail Based Lane Segmentation on the Highway	101
5.2.8	Radar Road Marking Based Lane Segmentation . . .	106

5.2.9	Summary	116
5.3	Point Cloud Lane Segmentation with Neural Networks . . .	117
5.3.1	Classification with Support Vector Machine (SVM) .	118
5.3.2	PointNet and PointNet++	119
5.3.3	Guard Rail Based Lane Segmentation	121
5.3.4	Radar Road Marking Based Lane Segmentation . . .	128
5.3.5	Summary	130
6	Summary and Outlook	131
	Bibliography	133
	Own publications	139
	Journal publications	139
	Conference publications	139

Acronyms and Symbols

Acronyms

ACC	Adaptive Cruise Control
ADAM	Adaptive Moment Estimation
ADMA	Automotive Dynamic Motion Analyzer
ADC	Analog-to-Digital Converter
AEB	Autonomous Emergency Breaking
ANN	Artificial Neural Network
AP	Average Precision
CAN	Controller Area Network
CFAR	Constant False Alarm Rate
CNN	Convolutional Neural Network
DFT	Discrete Fourier Transform
DL	Deep Learning
FCN	Fully Convolutional Network
FCW	Forward Collision Warning
FFT	Fast Fourier Transform
FMCW	Frequency-Modulated Continuous Wave
FN	False Negative
FP	False Positive

FPS	Farthest Point Sampling
GNSS	Global Navigation Satellite System
GPR	Ground Penetrating Radar
GPU	Graphics Processing Unit
HT	Hough Transform
HP	Horizontal Polarization
kNN	k Nearest Neighbors
LCA	Lane Change Assist
LDW	Lane Departure Warning
LiDAR	Light Detection and Ranging
LKS	Lane Keeping System
LSTM	Long Short Term Memory
MIMO	Multiple-Input and Multiple-Output
MLP	Multilayer Perceptron
MRG	Multi-Resolution Grouping
MSG	Multi-Scale Grouping
NN	Neural Network
R-CNN	Region-based CNN
RCS	Radar Cross Section
ReLU	Rectified Linear Unit
RFID	Radio-Frequency Identification
RGB	Red Green Blue
SBR	Shooting-and-Bouncing-Rays
SLAM	Simultaneous localization and mapping
SNR	Signal to Noise Ratio

SVM	Support Vector Machine
TN	True Negative
TP	True Positive
TPU	Tensor Processing Units
VP	Vertical Polarization
YOLO	You Only Look Once

Constants

π	Pi: 3.14159 . . .
-------	-------------------

Symbols

Lower case letters

a	Normalized amplitude of the target reflection
$a_j^{(i)[l]}$	Value of feature j in the i^{th} training example in layer l
c	Number of classes
c_0	Speed of light in the air
d	Ground range from radar to object
d_r	Longitudinal ground distance from radar to object
d_a	Lateral ground distance from radar to object
d_p	Distance between reflection points
d_{ps}	Distance between the placed radar road markers

d_{pt}	Distance tolerance between the placed radar road markers
f	Signal frequency
f_{s}	Sampling frequency
g_1	Initial roadway grade
g_2	Final roadway grade
h	Radar mounting height
l	l^{th} layer in a neural network
m	Number of training examples
n	Number of reflection points
n_{min}	Minimum number of reflection points within one cluster
$n^{[l]}$	Number of features in layer l
$\mathbf{n}^{[l]}$	Feature depth in layer l
p_n	Single cycle prediction probability
q	Curve fitting parameter
r	Range of the target
t	Time
v	Relative radial velocity of the target
v_{EGO}	Velocity of the test vehicle
v_{G}	Velocity of the reflection points of ground clutter
$x^{(i)}$	Input variable of i^{th} training example
x_i	Input variable of i^{th} measurement cycle
x	Lateral distance
$y^{(i)}$	Output variable of i^{th} training example
y_i	Prediction propability of i^{th} measurement cycle

y	Longitudinal distance
$\hat{y}^{(i)}$	Hypothesis of i^{th} training example

Capital letters

B	Bandwidth
$C^{[l]}$	Number of features of a reflection point at layer l
H	Height of the standing plates of a trihedral
L	Extended length of the bottom plate of a trihedral (chapter 3, 4) / Number of layers (chapter 5)
M	Reflection magnitude
N	Number of reflection points (chapter 5)
N_{FFT}	Number of FFT bins (chapter 2)
P_n	Joint prediction probability
R	Radius of the metallic sphere / Radius of the circle to define the curved standing plate of the reflector through intersection with the rectangle
T	Period of the FMCW ramp signal
T_{RMP}	Time duration of a FMCW ramp signal
$W^{[l]}$	Weight matrix of layer l (chapter 5)
W	Width of the bottom plate of a trihedral (chapter 3, 4)
X	A vector containing all x values
Y	A vector containing all y values

Greek symbols

α	Elevation angle
β	Azimuth angle
γ	Slant angle of the standing plates of a trihedral
η	Threshold factor of CFAR
σ	Radar cross section
κ	Learning rate
λ	Wavelength (before chapter 5) / Regularization parameter (in chapter 5)
ϕ	Angle difference between edges connecting reflection points
ψ	Signal phase

Mathematical notation and symbols

\vec{E}	Electric field
\vec{H}	Magnetic field

1 Introduction

1.1 Motivation

Autonomous vehicles and the vehicles equipped with driver assistance systems are significantly shaping the automotive industry, the transportation system, and our daily life. An autonomous driving system is mainly comprised of three parts: environmental perception, planning and decision-making, vehicle control and action. Thus the environmental perception is a prerequisite for the following two parts. Within this part, the lane detection function, which provides the vehicle the drivable path information, is especially important. This is currently only implemented with camera sensors mounted behind the vehicle's windscreen by analyzing the pixel information of the collected image data. However, a lane detection system solely implemented with camera sensors is rather unreliable, for example, when the vehicle encounters adverse environmental conditions like oncoming traffic with dazzling head light, or in dense fog, or when the sun is low in the sky, or when the illumination strength changes suddenly at the entrance or exit of a tunnel, etc. In order to improve the robustness of the system, other redundant sensor technologies shall be added to complement such shortcomings of the camera sensors.

The automotive radar sensors, which are currently massively equipped in vehicles and are capable of detecting objects like poles and guard rails at the road side, can be such a solution. However, for a road with multiple lanes, it is not possible to detect the current road markings between the lanes with radar sensors since they are not color sensitive. So in order to make the lanes also detectable by radar sensors, the structure and material of the current road markings shall be appropriately adapted. Corresponding clustering and classification algorithms also need to be developed.

1.2 State of the Art Technology

By detecting the road markings painted in contrasting colors, camera sensors mounted behind the windscreens of the vehicles are widely employed for lane detection [SAC05], [dPJ13]. Functions like Lane Change Assist (LCA), Lane Departure Warning (LDW), and Lane Keeping System (LKS), etc. can be realized with such video sensors.

A few researches focus also on lane detection with Light Detection and Ranging (LiDAR) device. Ref. [ITS⁺09] uses high reflective lane markings for detection with LiDAR and proves that such high reflective lane markings can be successfully detected by LiDAR. Furthermore, [OT06] states that the detection range of the road marking with LiDAR is up to about 20 m. These research papers also provide corresponding clustering and curve fitting algorithms. The short, micrometer-scale wavelength of the laser (normally 905 nm or 1550 nm for automotive LiDAR) enables it to detect the objects very precisely, which however oppositely restricts its detection robustness when encountering airborne particles (like the atmospheric particles, dust, fly ash etc.) whose diameters are larger than its wavelength. Table 1.1 lists and compares the wavelength of the automotive LiDAR, the 77 GHz Radar and the sizes of normal encountered particles. Table 1.2 summarizes the performance of various sensor types under adverse environmental conditions. Concluding from these comparisons, the radar is found to be a good complement and “orthogonal” sensor type to cope with adverse environmental conditions. Additionally, the price of LiDAR is still more expensive than a radar. So it can be concluded that it is advantageous if the lane detection function can also be realized with automotive radar sensors.

Table 1.1: Compare wavelength of automotive LiDAR and 77GHz automotive Radar with particle sizes.

	LiDAR	Radar	Mist	Atmospheric dust
λ / particle size (μm)	~1–10	~3900	70–350	0.001–40
	Auto emission	Cement dust	Fog	
λ / particle size (μm)	1–150	3–100	10–15	

Table 1.2: Performance comparison between various sensor types under adverse environmental conditions [NU17].

Environmental condition	Camera	LiDAR	Radar
Rain	-	-	0
Fog or haze	--	-	0
Sunset or sunrise	--	-	+
Sudden illumination change	--	++	++
Night	0	+	+

With the state-of-the-art automotive radar sensors on the market, driver assistance functions like Adaptive Cruise Control (ACC), Forward Collision Warning (FCW), and Autonomous Emergency Braking (AEB) can be realized. With the recently achieved resolution improvement, objects like pedestrians and cyclists can also be detected and recognized with radar sensors by analyzing their specific Range-Doppler characteristics. Relevant research [GLM⁺01] proposes the combination of various sensor types for cooperative collision avoidance, where macroscopic corner reflectors with a dimension between 10 cm and 20 cm are arranged in distinctive patterns to identify various obstacles using radar sensor. These corners are placed with certain intervals, or in other words, the distances between them are “coded” to make the identification of various obstacles possible. Similar ideas are also in [VHJW] where the distance coding is exploited to help the Global Navigation Satellite System (GNSS) for the precise location of the vehicle. However, because of their relative large size, it is not possible to place such radar corner reflectors as part of the radar road markings on the road.

Besides the above mentioned sensor types, some further novel ideas for vehicle guidance, even without road markings are proposed. For example, the ones in [TMBP09], [KP17] realize that task with a high resolution map or navigation system. However, since such a system requires real-time and robust connection between vehicles and satellites or base transceiver stations under all circumstances, its reliability is lower than an “on-board” device like a radar. Totally different, patents [MWS16], [Bog12] try to integrate Radio-Frequency Identification (RFID) tags into the roads or road markings to deliver the road information to the vehicles. No practical test is however implemented to verify this idea and no information about the sensing range of such RFID tags

is specified. Patent [oT14] utilizes a Ground Penetrating Radar (GPR) whose wavelength is much larger than that of a 77GHz automotive radar to extract the structural features in the soil and compares that with pre-stored feature maps to determine the precise location of the vehicles. This idea is based on the assumption that the structural feature underground of every location is unique, like the fingerprints of a human. Ref. [CT03], [HK03] insert magnetic markers into the road after drilling holes in it. By analyzing the magnetic field distribution characteristics, the vehicle location can be determined. All these ideas are very interesting but they have a common disadvantage when compared with the massively equipped automotive radar sensors: new sensors need to be installed into the vehicles.

Deep Learning (DL) with Neural Networks (NN) is nowadays widely used for object- and pixel-level classification or semantic segmentation with optical sensors like video cameras or LiDAR sensors. Object-level NNs include conventional Convolutional Neural Networks (CNNs) and other variants based on it, like Region-based CNN (R-CNN) [GDDM14], Fast R-CNN [Gir15], Faster-RCNN [RHG17], and You Look Only Once (YOLO) [RDGF16], [JA17], etc. Pixel-level semantic segmentation NNs include CNN-based fully convolutional networks (FCN) [SLD16] and SegNet [BKC17], etc. Limited by its resolution, environmental perception, especially lane detection with automotive radar sensors using DL is still lacking research interest and focus. Ref. [CSSW17] implements semantic segmentation with NNs for lane segmentation based on the data of LiDAR sensors.

1.3 Goal and Methodology

Since color information can not be recognized by radar sensors, in order to differentiate adjacent lanes with radar sensors, the currently employed road markings shall be adapted both from the aspect of structure and material. For radar sensors, one very important object characteristic parameter to describe the detection performance is the so-called Radar Cross Section (RCS). The higher the RCS is, the easier the object can be detected. So objects, which are suitable to be integrated between adjacent lanes or into the road markings, shall be analyzed w.r.t. their RCS values. Besides providing enough RCS in wide azimuth angle range, the shapes of these objects shall also be optimized: their

height shall not be too large in order not to impede the driving comfort and the safety of the vehicles running over them during their lane change actions. So in this dissertation, the RCS of various types of reflectors is evaluated and compared over a wide angular and range geometry both by simulations and on-road tests. The simulation results are evaluated with respect to the view angle from the vehicle to the reflector and a best appropriate radar reflector suitable for the new type of radar road markings is proposed. For the on-road tests, clustering and classification algorithms are introduced, too. Furthermore, with the radar-detectable road markings, the determination of the lateral position of the vehicle with the help of Range-Doppler characteristics is also presented.

With a high-resolution prototype radar developed in the advanced department of the Robert Bosch GmbH, environmental perception, especially lane detection using DL or NNs are presented in this dissertation. Ref. [LLMHW17] utilizes FCN for parking space semantic segmentation with integrated radar detection points. In this dissertation instead, single-shot radar detection points are used for lane detection with the help of guard rails at the road side and the new type of radar road markings. The NNs are accordingly adjusted and tweaked for radar data as input and the output results are compared, analyzed and discussed.

1.4 Summary of the Goals of this Thesis

In order to increase the robustness of the lane detection function, automotive radar sensors can be used to complement the shortcomings of the video camera sensors. If the lane can be detected by several distinct sensor types, sensor data fusion can then be applied to increase the robustness and performance of the overall system. The main goals of this dissertation are:

- to find out and to verify the feasibility of lane and road marking detection with automotive radar sensors by appropriately adjusting the current road markings, i.e. to elaborate an optimal structure of the radar road marking with low height but enough RCS in a wide azimuth angle range, while using a simple fabrication process to keep the deployment cost still moderate;

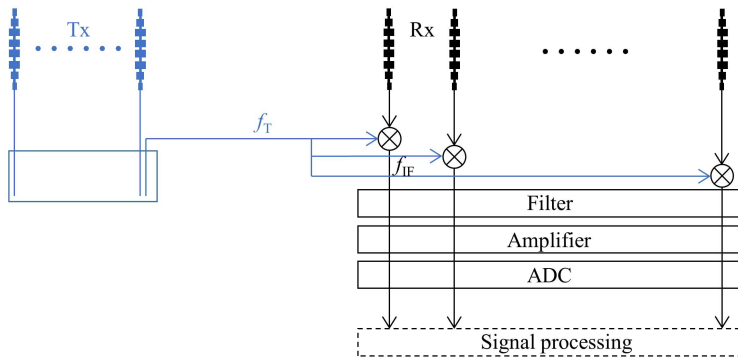
- to prove and to validate the RCS of various promising reflector types with both simulation and practical on-road tests, to simulate and to measure how the size of its structure influences the RCS values. To propose a new type of radar road marking based on the above verified optimal structure;
- to develop the corresponding clustering algorithms, with the focus on DL algorithms for lane classification and semantic segmentation based on the single-shot radar reflection points of the radar road markings and the guard rails on the highway.

2 FMCW Radar

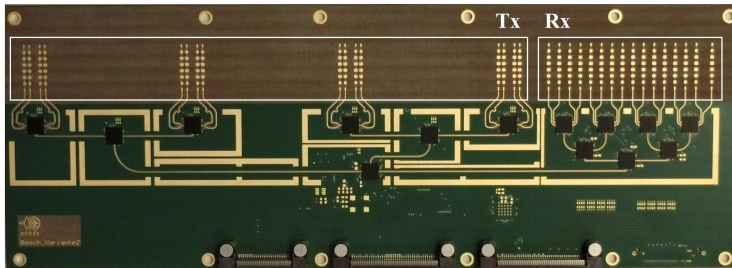
FMCW radar is used in this thesis for detecting objects. So this chapter summarizes briefly the working principle of the FMCW radar, including its signal processing procedure. In principle, this chapter is not novel but serves only for understanding how a FMCW radar works.

2.1 Concept of FMCW Radar

FMCW is the abbreviation for Frequency Modulated Continuous Wave and is a modulation approach of the radar signal where the information is carried in its frequency. Figure 2.1 (a) shows briefly the hardware architecture of a FMCW radar. Tx and Rx are abbreviations for transmitter and receiver separately and f_T is the frequency of the transmitted signal. As digital signal processors can not handle continuous signals, they need to be sampled with ADCs (Analog-to-Digital Converters) for further processing. Figure 2.1 (b) shows a corresponding front-end board developed in the advanced development department of the Robert Bosch GmbH in Leonberg. Figure 2.2 presents the corresponding signal model scheme—a sawtooth FMCW modulation that will be discussed in details in the following sections where f denotes the frequency of the signal, B the bandwidth, f_0 the middle of the bandwidth, T the period of a ramp signal, and T_{RMP} the time duration of a single ramp signal. In this figure, the ramp in blue color denotes the transmitted signal and the ramp in black is the corresponding received signal at the receiver side reflected by a certain target. After every cycle the signal is transmitted, a break is needed before another cycle to transmit the signal starts and Δf is the signal frequency difference between transmitted and received signals that can be obtained from the signal after the mixer and filter.



(a)



(b)

Figure 2.1: (a) Architecture of a FMCW radar hardware prototype. (b) A FMCW radar front-end board.

2.2 Raw Data Processing

This section is arranged according to the processing sequence of the radar signal: the first step is to determine the range of the targets; then the velocity is evaluated followed by the CFAR (Constant False Alarm Rate) algorithm to get the individual radar reflection points; at last the angle estimation algorithm is conducted.

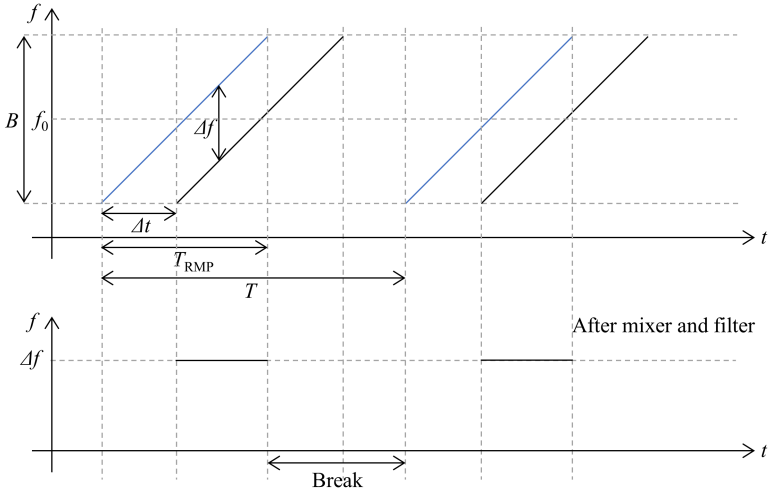


Figure 2.2: An example of a sawtooth FMCW modulation scheme.

2.2.1 Range of the Target

Like shown in Figure 2.2, the signal is transmitted from Tx, scattered back by a target and then received by the Rx and the range of the target is proportional to the time delay Δt of the transmitted and received signals. FMCW maps Δt into the frequency domain: the ramp signal with linear increment makes the signal frequency difference between transmitted and received signals Δf proportional to Δt . Assume the target is located at a range of r , then r can be represented by:

$$r = c_0 \Delta t / 2 \quad (2.1)$$

with c_0 denoting the propagation velocity of the electromagnetic wave in the air. This equation assumes that the target is located at a range that is much larger than the distance between Tx and Rx so that the propagation path lengths between Tx, Rx and the radar are both equal to r . From Figure 2.2, it can be seen that Δt can be represented by Δf according to:

$$\Delta t = \frac{T_{\text{RMP}}\Delta f}{B}. \quad (2.2)$$

Combine both equations (2.1) and (2.2), the relation between r and Δf can be expressed as follows:

$$r = \frac{T_{\text{RMP}}\Delta f c_0}{2B}. \quad (2.3)$$

So by knowing Δf , the range of the target can be very easily calculated according to equation (2.3). A critical component to get Δf is the mixer which multiplies the signal from the receiver with the signal from the transmitter. Assume the received signal $s_r(t)$ at time t with $f(t)$ is (assume unit amplitude and zero initial phase for simplicity):

$$s_r(t) = \cos(f(t)t), \quad (2.4)$$

and the signal of the transmitter $s_t(t)$ at time t is:

$$s_t(t) = \cos(f(t + \Delta t)t). \quad (2.5)$$

Then after the mixer, the signal with the frequency $\Delta f = f_{\text{IF}} = f(t + \Delta t) - f(t)$ can be derived after filtering out other signal parts with much higher frequencies according to:

$$s_r(t) \times s_t(t) = \cos((f(t + \Delta t) + f(t))t) + \cos((f(t + \Delta t) - f(t))t). \quad (2.6)$$

In short, the range information of the target is contained in the frequency of the output signal of the mixer. However, in order to be able to process this analog signal in a digital processor or computer, it needs to be converted into the digital signal. So the following section will introduce this part briefly.

If an analog signal of frequency f_a is sampled with a sampling frequency f_s , a corresponding digital frequency (normalized frequency) f_d can be represented by:

$$f_d = \frac{f_a}{f_s}. \quad (2.7)$$

In DFT (Discrete Fourier Transform) or FFT (Fast Fourier Transform)—a faster and more efficient algorithm to calculate the DFT, if N_{FFT} points are sampled, then the digital frequency f_d can be expressed by:

$$f_d(k) = \frac{k}{N_{\text{FFT}}}, \quad (2.8)$$

where k is the FFT bin index from 0 to $N_{\text{FFT}} - 1$. So combine equations (2.3), (2.7), and (2.8) with $f_a = \Delta f$, the range r calculated from the FFT is:

$$r(k) = \frac{T_{\text{RMP}} k f_s c_0}{2BN_{\text{FFT}_R}} (k = 0, 1, \dots, N_{\text{FFT}_R} - 1). \quad (2.9)$$

This is a discrete value, and errors from FFT (i.e. spectrum leakage) can be introduced into these results. The distance r_{bin} between two range bins then is:

$$r_{\text{bin}} = \frac{T_{\text{RMP}} f_s c_0}{2BN_{\text{FFT}_R}}. \quad (2.10)$$

When the condition $f_s T_{\text{RMP}} = N_{\text{FFT}_R}$ is fulfilled (which is the typical case as long as the sampling process goes through the whole ramp signal duration), equation (2.9) can then be simplified to $r(k) = \frac{k c_0}{2B}$. Under this condition, it is obvious that the range bin is no longer related to the sampling frequency any more, but is only inverse proportional to the bandwidth of the signal.

Range Resolution

Resolution describes the ability to distinguish two adjacent objects and equals normally to the width between the two half-power points of the main lobe of the signal spectrum. With various windowing functions, such resolution may change significantly. For example, Table 2.1 presents three such examples with various windowing functions. Normally, with a smaller (better) resolution, the side lobes become oppositely larger, indicating a trade-off between these two parameters. In order to improve the detection resolution with a defined windowing function, a higher bandwidth is required according to equation (2.10). Notice that with zero padding, the r_{bin} can be smaller, however, the resolution remains unchanged.

Table 2.1: Range resolution of the radar with various windowing functions (no zero padding).

Window function	First side lobe (dB)	Width of main lobe (m)	Resolution r_{res} (m)
No window (rectangle)	-13	$2r_{\text{bin}}$	$0.89r_{\text{bin}}$
Hann	-32	$4r_{\text{bin}}$	$1.44r_{\text{bin}}$
Hamming	-43	$4r_{\text{bin}}$	$1.30r_{\text{bin}}$

Figure 2.3 (a) shows one range detection example with several reflectors (which will be introduced in details in chapters 3 and 4) placed in front of the radar. The windowing function employed here is a Chebyshev window with 111 dB side lobe attenuation. Unlike the windowing functions in Table 2.1, the resolution of the Chebyshev window can manually be changed by varying its side lobe attenuation. All the related parameters of this example are summarized in Table 2.2.

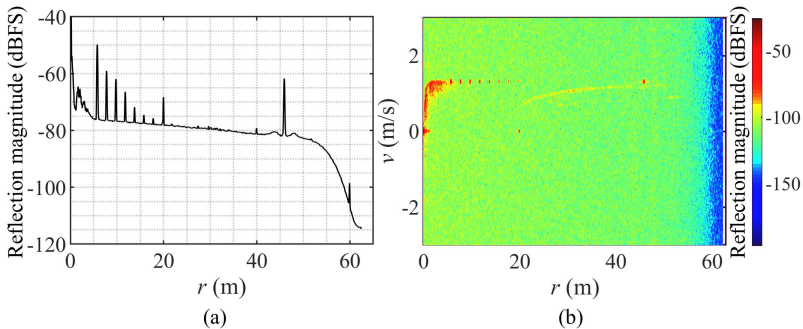


Figure 2.3: Signal processing of the FMCW radar. (a) Range from 1D FFT. (b) Range-Doppler from 2D FFT.

Table 2.2: Range detection parameters in Figure 2.3 (a).

B (GHz)	r_{bin} (m)	r_{res} (m)	N_{FFT_R}	f_s (MHz)
2.46	0.035 with 2 times zero padding	0.14 (about $2r_{\text{bin}}$ without zero padding)	2048	62.5

Maximum Detection Range

According to the Nyquist Theorem, the sampling frequency f_s shall be at least half of the signal frequency f_a , together with equation (2.3), the maximum detection range r_{\max} can then be expressed by:

$$r_{\max} = \frac{T_{\text{RMP}} f_s c_0}{4B}. \quad (2.11)$$

If a target is located at a range larger than r_{\max} , then its calculated range r from the FFT is not correct and folded back. In order to increase the r_{\max} , a higher sampling frequency f_s is required according to equation (2.11). Insert the parameters in Table 2.2 into this equation with $f_s T_{\text{RMP}} = N_{\text{FFT_R}}$, the resulting r_{\max} is 62.4 m.

2.2.2 Velocity of the Target

In the previous section to calculate the range of the target, a single Tx, Rx, and one signal ramp are required. To estimate the velocity of the object after estimating r by employing the first FFT—the 1D range FFT, multiple signal ramps are required through the second FFT processing—the 2D FFT. Remember in Figure 2.2 that the period of the ramp signal is T . Figure 2.4 (a) illustrates in principle how the velocity is determined. A blue brick in solid blue rectangle in Figure 2.4 (a) moves with various velocities directly to a static vehicle equipped with a radar at its front and the dashed blue rectangles show the positions of the brick after every time duration T . Because of this movement of the brick, the phase of the received signal at the receiver side of the radar also changes correspondingly. In the examples, when the object stays static, after every time interval T , the received phase of the signal stays unchanged and a signal with such a constant phase has a frequency f_v of 0 Hz. When the object moves $\lambda/16$ (λ is the wavelength of the signal) meters closer to the radar after every time slice T instead, the received phase changes 45° ($\lambda/16$ corresponds to 22.5° , it needs to be multiplied by a factor of 2 in consideration of the two way propagation: for- and backwards to the object from the radar), resulting in a f_v of $\frac{1}{8T}$. Similarly, when the brick moves two times faster, the f_v becomes also two times higher: $\frac{1}{4T}$. These examples illustrate in principle

how a FMCW radar works for velocity determination and it can be concluded from the illustration that the velocity information is also contained in the signal frequency. So similar to the range determination, the FFT algorithm can also be used for the velocity determination.

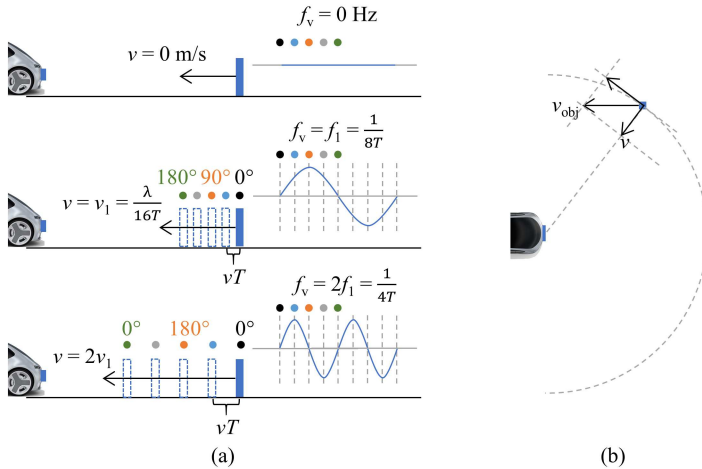


Figure 2.4: (a) Principle of velocity determination with FMCW radar. (b) Movement velocity of the object and its measured radial velocity.

Equation 2.12 describes the relation between the object velocity v and the corresponding signal frequency f_v :

$$f_v = \frac{2v}{\lambda}. \quad (2.12)$$

The explanation to calculate the velocity above also shows that the measured velocity v depends on the distance between the object and the radar, indicating that the v is a relative velocity of the object to the radar and if an object moves not directly to the radar, only the projection of the moved distance on the radar direction can be taken into account. In other words, the v of the object is the radial projection component of its real movement velocity on the direction to the radar (i.e. radial velocity). Figure 2.4 (b) illustrates such an example with a movement velocity v_{obj} and its detected velocity v —the projection of v_{obj} .

Similar to equation (2.10), the FFT bin of velocity v is:

$$v_{\text{bin}} = \frac{c_0}{2T f_0 N_{\text{FFT}_V}}, \quad (2.13)$$

with $f_s = 1/T$, $f_a = f_v$, and N_{FFT_V} the number of the signal ramps. The calculation of the resolution v_{res} and the maximum detection velocity v_{max} in equation (2.14) is similar to that in section 2.2.1 and is not repeated here.

$$|v_{\text{max}}| = \frac{c_0}{4T f_0} \quad (2.14)$$

Figure 2.3 (b) presents such an example with the vehicle moving towards several static radar reflectors and the color in the plot indicates the FFT magnitudes. Since such result contains both range and velocity of the objects, it is also called the Range–Velocity or Range–Doppler plot. Its corresponding parameters can be seen in Table 2.3.

Table 2.3: Velocity detection parameters in Figure 2.3 (b).

N_{FFT_V}	f_0 (GHz)	T (μs)	v_{bin} (m/s)	v_{res} (m/s)	v_{max} (m/s)
2048	77	48	0.02 without zero padding	About 0.045 ($2.25v_{\text{bin}}$ with a Chebyshev win- dow of 141.5 side lobe attenuation)	20.3

2.2.3 CFAR Processing

After calculating the range and velocity spectra with FFT processing, the relevant reflection peaks need to be extracted. These peaks stem not only from the target reflections, but may also come from the noise. To distinguish them, a threshold level needs to be defined and the reflection values above this threshold are thought to be the reflections of the targets. If a constant threshold level is defined, the noise above the threshold may be wrongly detected as targets when the threshold is set too low and the real targets may not be correctly detected if the threshold is set too high. Notice that the reflection power decreases (free space loss) and the filters like low pass filter in the radar can also lead to reflection magnitude variation with respect to r , indicating that a constant

threshold over the whole spectrum is not optimal. To cope with this challenge, a CFAR algorithm can be employed.

False alarm describes the false detection of a target that does not exist in reality and the CFAR algorithm can keep the corresponding false alarm rate constant by adjusting the threshold level accordingly—a non-constant adaptive threshold level. CFAR divides the cells (imagine them as the power of the reflections in the FFT bins) into three parts: the cell under test (CUT), the guard cells leading and lagging the CUT, and the remaining training cells. Figure 2.5 (a) illustrates such an example where the noise power P_{noise} of the CUT is calculated based on the training cells and the corresponding threshold power P_{TH} is proportional to this noise level by a scaling factor η which depends on the required false alarm rate:

$$P_{\text{TH}} = \eta P_{\text{noise}}. \quad (2.15)$$

Various methods to calculate the noise power P_{noise} of the CUT lead to various CFAR algorithms: if the average power of the cells at the left and right side of the CUT is separately calculated and the larger one is chosen as P_{noise} , then it is CAGO-CFAR (Cell Averaging Greatest Of-CFAR); if the smaller one is chosen as P_{noise} , then it is CASO-CFAR (Cell Averaging Smallest Of-CFAR); if P_{noise} equals to the average value of the power over all the training cells, then it is a CA-CFAR (Cell Averaging-CFAR); if all the training cells are firstly sorted in ascending power sequence and only the k^{th} rank element is selected as the P_{noise} , it is called OS-CFAR (Ordered Statistic-CFAR).

Figure 2.5 (b) presents an example of CFAR thresholding of the data in Figure 2.3 with its magnitude replaced by its power (through squaring). P_{noise} and P_{TH} of both CA-CFAR and OS-CFAR are plotted with 10 guard cells and 100 training cells. The false alarm rate for CA-CFAR is set to be 0.1 and the rank k of OS-CFAR is set to be 50. By comparing the results, it can be found that there are always two high plateaus at the two sides of the signal with CA-CFAR, whereas with OS-CFAR, this does not exist and its threshold level also fluctuates much less. So CA-CFAR is very sensitive when multiple targets simultaneously exist, especially when they are very close to each other. For example, the right plateau of the object at 6 m almost covers the object at the range of about 8 m in Figure 2.5 (b). From the perspective of this point,

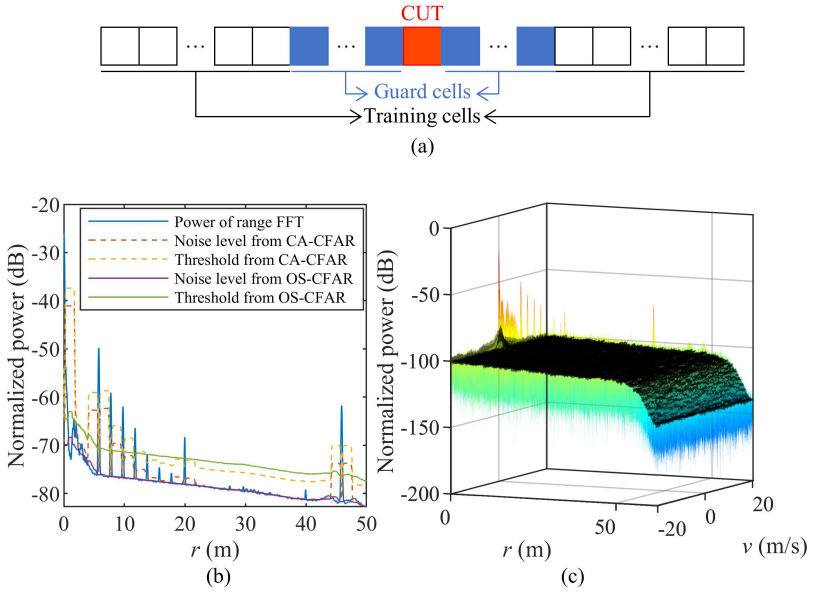


Figure 2.5: (a) CFAR: various operations employed to the training cells to estimate the noise level of the CUT (Cell Under Test). Guard cells are needed to avoid the influence of the signal on the estimation of the noise level. (b) Range from 1D FFT and the corresponding noise and threshold level from CA- and OS-CFAR. (c) Range-Doppler from 2D FFT and the corresponding threshold level (black layer) estimated from OS-CFAR.

OS-CFAR is preferred to CA-CFAR. Figure 2.5 (c) presents also the threshold of the Range-Doppler results with OS-CFAR.

After calculating the threshold with CFAR, the points with their power larger than this threshold are extracted to be the reflection points collected by the radar. The last information of these points—the angular information will be calculated in the following section.

2.2.4 Direction of Arrival (DOA): Maximum Likelihood Estimation

To calculate the range of a target, single Tx, Rx and one signal ramp are required. To determine the velocity of a target, single Tx, Rx, and multiple signal ramps are necessary. And to get the angle of a target in this section, a single Tx and multiple Rx are needed while additional Tx can be added to increase the angle detection resolution by utilizing the MIMO (Multiple-Input and Multiple-Output) concept.

Similar to the previous sections where the range and velocity of the targets can be calculated through the signal frequency, their angles can also be determined in a similar way. Refer to Figure 2.6 (a) where a target is located at an angle β of the Rx array which contains multiple horizontally equidistant arranged receiver antennas with a spacing of d_{array} , the phase difference $\Delta\psi$ between the signals received by these Rx is:

$$\Delta\psi = \frac{2\pi c_0 d_{\text{array}} \sin \beta}{f_0}, \quad (2.16)$$

and this phase difference corresponds to a sampling frequency f_s :

$$f_s = \frac{2\pi f_0}{\Delta\psi}. \quad (2.17)$$

Combine equations (2.7), (2.8), (2.16), and (2.17), the angle β after FFT processing equals to:

$$\beta(k) = \arcsin\left(\frac{k f_0}{d_{\text{array}} c_0 N_{\text{FFT_A}}}\right), (k = 0, 1, \dots, N_{\text{FFT_A}} - 1) \quad (2.18)$$

where $N_{\text{FFT_A}}$ is the number of Rx channels. If $d_{\text{array}} = \lambda/2$, equation (2.18) deduces to:

$$\beta(k) = \arcsin\left(\frac{2k}{N_{\text{FFT_A}}}\right). \quad (2.19)$$

$\lambda/2$ is the maximum allowed d_{array} between the Rx antennas since under this condition, the sampling frequency f_s is exactly two times the signal frequency

f_0 when $\beta = 90^\circ$. A larger d_{array} violates the Nyquist Theorem and a smaller d_{array} makes the angle resolution worse.

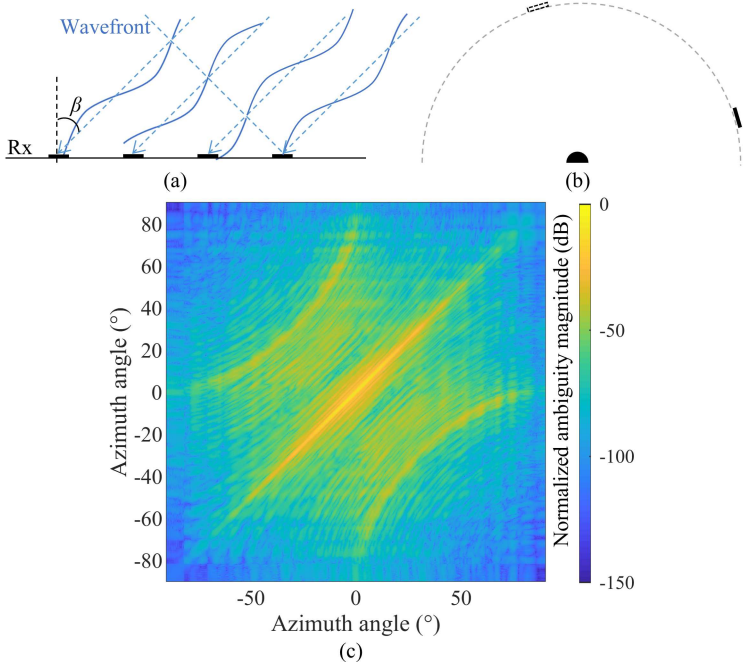


Figure 2.6: (a) Angle determination of the object from the phase difference across multiple receivers. (b) Radar sensor calibration. (c) Ambiguity matrix of a prototype automotive radar used in this dissertation.

However, the above description is only correct when $\Delta\psi$ comes from the length difference of the signal propagation path in the free air and when the r of the object is much larger than d_{array} (i.e. far field). In practice, this condition is not always fulfilled, both when the object is very close to the radar (i.e. near field) or when additional phase difference is introduced by the trace length difference of the radar signals and sampling clock signals in the radar board, etc [FKMW16]. One simple way to handle this is to cover all these phase differences by practical calibration and compare the phase difference of unknown β with the ones measured during the calibration. In this way, the most similar phase difference to the measured one indicates the angle of arrival of

the object. Figure 2.6 (b) illustrates such a calibration process: a target like a corner reflector moves around the radar, and the phase differences between all the Rx channels when the target is located at each β are recorded. Equivalently, instead of moving the target, the radar can be rotated along its origin point while keeping the object stationary. Assume the signal phase corresponding to the i^{th} Rx channel is ψ_i , then the signal phases of all the Rx channels when the object is at β can be expressed by (we ignore amplitude for simplicity):

$$\mathbf{S}_{\text{cal}}(\beta) = [e^{-j\psi_1} e^{-j\psi_2} \dots e^{-j\psi_{N_{\text{FFT}_A}}}], \quad (2.20)$$

Assume the signal phases of the Rx during tests are similarly expressed by \mathbf{S}_{test} , then the angle β which makes $|\mathbf{S}_{\text{test}}\mathbf{S}_{\text{cal}}^*(\beta)|$ the maximum value among all calibrated β is the angle of the target, where $\mathbf{S}_{\text{cal}}^*$ is the conjugate number of \mathbf{S}_{cal} . An ambiguity matrix comprised of $|\mathbf{S}_{\text{cal}}(\beta_1)\mathbf{S}_{\text{cal}}^*(\beta_2)|$ can be used to describe similarity of the phase differences across all Rx channels when the target is located at various β . The larger this value is when $\beta_1 = \beta_2$ and the smaller this value is when $\beta_1 \neq \beta_2$, the better the radar is to determine the angle of the target. Figure 2.6 (c) plots such a matrix of the prototype radar used in this dissertation.

If the antenna array of Rx is also geometrically arranged in the vertical direction, then an elevation angle of the target can also be determined [SWM⁺18] in addition to the azimuth angle.

2.3 Summary

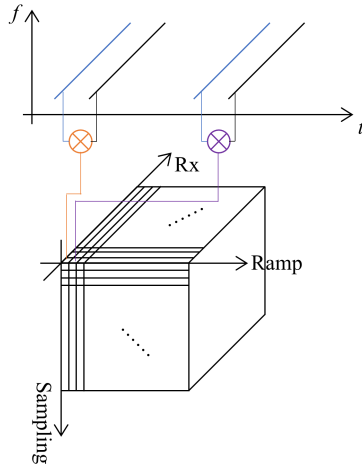


Figure 2.7: Signal processing of a FMCW radar to get the range r , velocity v , and angle β of the object.

This chapter presents briefly the signal processing procedure of a FMCW radar with fast chirp-sequence modulation. In summary, the range r , velocity v , and angle β can be determined by the 3D FFT like the one shown in Figure 2.7: the 1st FFT determines r , the 2nd FFT calculates the v , and the 3rd FFT evaluates the azimuth angle β . Because of the additional phase shifts, the last FFT to calculate the angle values is usually replaced by other algorithms e.g. the maximum likelihood estimation algorithm. The CFAR algorithm is employed to calculate an adaptive threshold level from the FFT spectrum to extract the reflection points. This chapter is not novel but serves only for understanding how a FMCW radar works.

3 Radar Cross Section and Radar Reflectors

A very basic and generic indicator to describe how easily an object can be detected by a radar is the Radar Cross Section (RCS). An object with a larger RCS is more likely to be detected by the radar than that with a smaller RCS. In this chapter, the basic concept of RCS will be introduced firstly. Then, the minimum required RCS of an object that needs to be detected by the radar is evaluated. After that, RCS values of several typical reflectors will be presented. RCS simulation results of the proposed reflector variants that can be used as radar-detectable road markings / markers will be given. Afterwards, the influence of the mounting position of the radar and the road curvature on the detection performance will be analyzed. At last, with such reflectors integrated on the road, a method to determine the movement status of a vehicle based on the Range-Doppler results will be discussed.

3.1 Radar Cross Section

3.1.1 Definition

Radar cross section, normally represented by σ , describes the scattering characteristic of an object. On the one hand, this value depends not only on the material, the physical shape and size of an object, but also on the incident and reflected angle, the polarization and wavelength of the signal, etc. On the other hand, RCS is the property of an object that does not depend on the distance between the radar and the object. Normally, this value is not equal to the physical cross section (i.e. the projected area orthogonal to the incident wavefront) of the object. If the transmitter and receiver antennas are located at the same position, it is also called the monostatic RCS, otherwise it is the

bistatic RCS. For an automotive radar to detect the road markings, the antennas are very close to each other compared to the distance between the radar and the reflectors, so if not otherwise specified, the RCS in this dissertation always refers to the monostatic RCS.

The definition of σ can be seen in equation (3.1) where $|\vec{E}^s|$ is the electric field scattered back from the object, and $|\vec{E}^i|$ is the incident electric field hitting the object. Both fields have two polarization directions: horizontal and vertical, leading to a $[\vec{\sigma}]$ including four combinations like in equation (3.2) [WR87] where σ_{vh} indicates a horizontal reflected and vertical incident polarized signal. As the radar used in this dissertation employs vertical–vertical polarization, σ_{vv} is simply represented by σ in the following sections if not otherwise specified.

$$\sigma = \lim_{r \rightarrow \infty} 4\pi r^2 \frac{|\vec{E}^s|^2}{|\vec{E}^i|^2} \quad (3.1)$$

$$\begin{bmatrix} \vec{\sigma} \end{bmatrix} = \begin{bmatrix} \sigma_{hh} & \sigma_{hv} \\ \sigma_{vh} & \sigma_{vv} \end{bmatrix} \quad (3.2)$$

3.1.2 Minimum Required Radar Cross Section

To evaluate the minimum required radar cross section σ_{\min} , a reference corner reflector (corner S, length of the edge is 0.10 m, maximum σ in boresight direction is about 14.4 dBsm) standing in front of a FMCW radar operating in the bandwidth from 77 GHz to 81 GHz [MSK15], [MSK17] is used. During the measurements, the radar is mounted at a height h of 0.15 m in the front of a test vehicle. The standing corner S that points directly to the direction of the radar and the driving direction of the test vehicle has a 0.35 m height above the ground. Three distinct tests are carried out with the vehicle driving directly towards corner S (azimuth angle $\beta = 0^\circ$). Together with the reflection from the ground and the system noise level, the reflection magnitudes of corner S during the movement of the test vehicle to the reflector are recorded and plotted in Figure 3.1.

Because of the multi–path reflection effect, the signal reflected from the corner S can both be constructive or destructive superimposed, resulting in a ma-

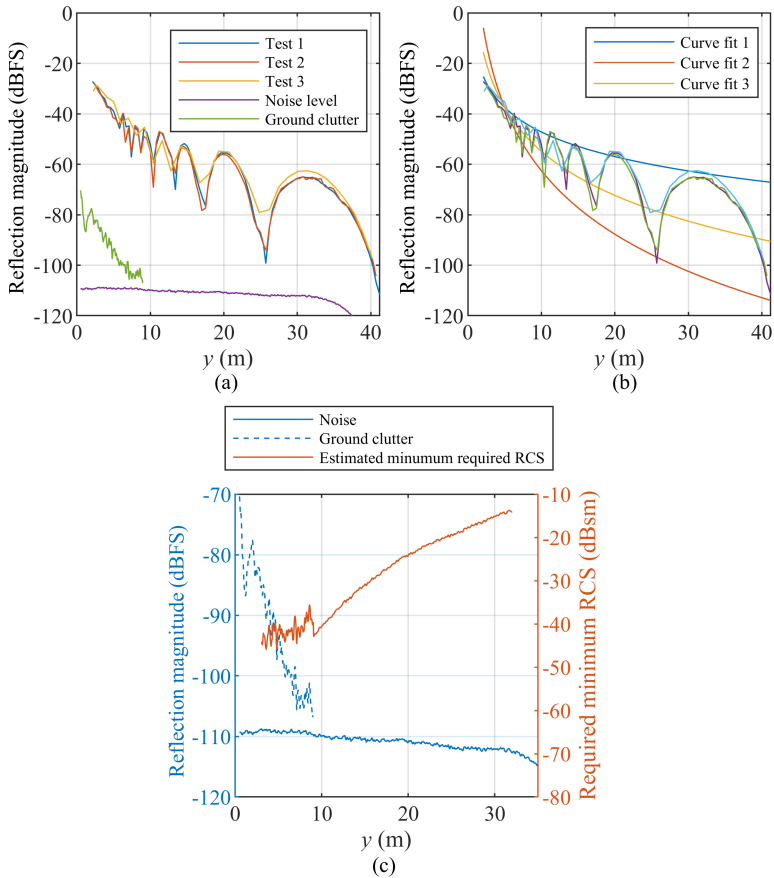


Figure 3.1: Estimation of σ_{\min} with respect to longitudinal distance y ($x = 0$ m). (a) Reflection magnitudes of a reference corner S in three separate tests and the corresponding magnitude of ground clutter and noise. (b) To estimate the reflection magnitude of the standing reference corner S from its fluctuant magnitudes caused by multi-path propagation effect, three curves are plotted: curve fit 1 fits the peaks of the magnitudes, curve fit 2 fits the troughs of the magnitudes, and curve fit 3 plots the mean value of curve fit 1 and 2 to represent the reflection magnitude of corner S without multi-path propagation. (c) Estimated σ_{\min} with respect to y .

gnitude fluctuation shown in Figure 3.1 (a). In order to estimate the reflection

magnitude without the multi-path effect, two curves are created to fit their peaks and troughs, like curve fit 1 and 2 in Figure 3.1 (b). Then, the average value of these two curves—the curve fit 3 is calculated as the reflection magnitude M_r of the corner S without multi-path reflection. Curves 1 and 2 are fitted according to equation (3.3) and for curve 1 and curve 2: $q_1 = 1.62$, $q_2 = 14.8$, and $q_1 = 4.18$, $q_2 = 21.06$ respectively.

$$\text{Reflection magnitude } M = 20 \log_{10} (1/y^{q_1}) + q_2. \quad (3.3)$$

Assume the magnitude of ground clutter is M_g and the noise level is M_n (in dB scale), then the σ_{\min} with respect to y can be calculated by:

$$\sigma_{\min}(y, SNR) = \sigma_{\text{corner S}}(y) - (M_r - \max(M_g, M_n + SNR)) + \text{Comp}_V, \quad (3.4)$$

where SNR stands for signal to noise ratio, and Comp_V is used to compensate the antenna gain difference between the standing reference corner S and the object located at the same position but is placed directly on the ground surface (like radar road marker or markings) because of their various elevation angle α . The corresponding relative antenna gain difference in elevation direction is shown in Figure 3.2 (b) and the calculated σ_{\min} is plotted in Figure 3.1 (c). This plot indicates that if one object laid on the ground needs to be detected by this radar at a distance of 30 m, it shall have at least a RCS of about -15 dBsm.

With the antenna gain difference in the azimuth β direction shown in Figure 3.2 (a), the above calculation can also be extended into 2D space:

$$\sigma_{\min}(r, SNR) = \sigma_{\min}(y, SNR) + \text{Comp}_A(r), \quad (3.5)$$

where Comp_A is needed to compensate the azimuth antenna gain difference with respect to $\beta = 0^\circ$. The calculation result is plotted in Figure 3.3 and in this plot, the minimum required RCS σ_{\min} at any arbitrary position can easily be determined. However, this plot depends also on many other parameters, meaning if e.g. the mounting position of the radar, the antenna gain, the number of FFT bins during signal processing (processing gain), etc. are changed, the results in this plot will also change accordingly. In chapter 3.4, the influence of the mounting position of the radar will be analyzed more in details.

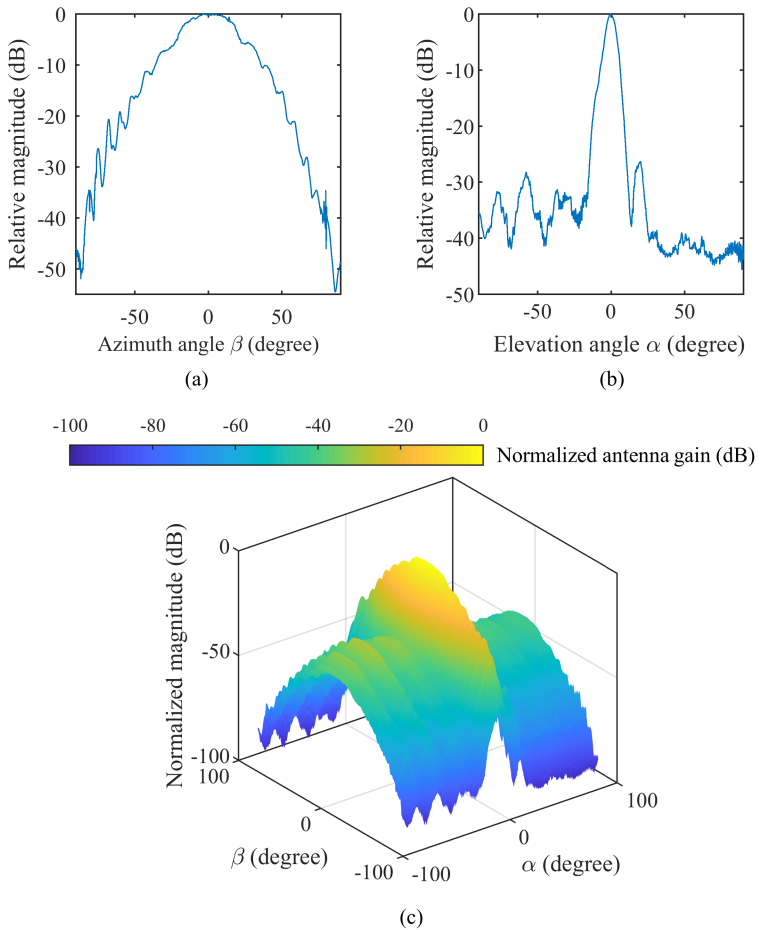


Figure 3.2: Relative antenna gain of a prototype FMCW automotive radar (a) in azimuth direction, (b) in elevation direction, and (c) in both azimuth and elevation directions.

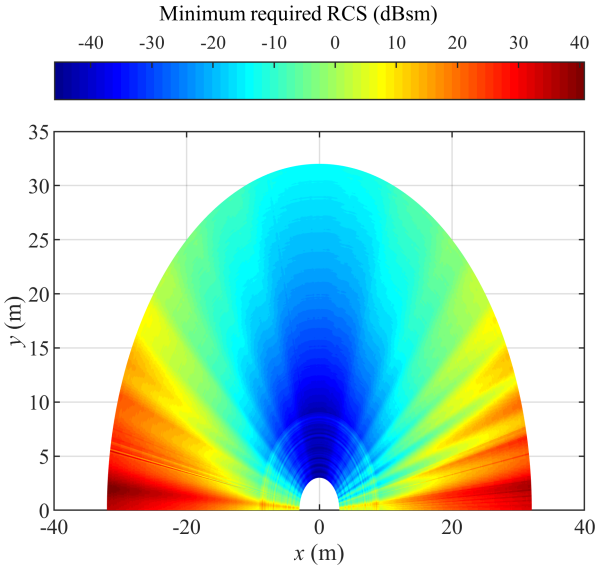


Figure 3.3: Estimated σ_{\min} with respect to x and y ($h = 0.15$ m, $N_{\text{FFT}_A} = N_{\text{FFT}_V} = 1024$).

3.2 Radar Cross Section Dependencies: Influences, Effects, and Comparison of Typical and Relevant Targets

In this chapter, a commercial software CST MICROWAVE STUDIO® is employed to speed up the RCS analysis procedure. The basic setup of the simulation environment can be seen in Table 3.1 where SBR is the abbreviation for Shooting-and-Bouncing-Rays.

3.2.1 Spheres

It is possible to add metallic balls to the current road markings to increase their σ [PKK⁺15], like the sample shown in Figure 3.4. For a single metallic ball, by changing its radius R , its scattering can be located in three distinct regions:

Table 3.1: CST MICROWAVE STUDIO[®] 2016 simulation environment setup.

Solver	Asymptotic solver (SBR Raytubes)
Signal frequency	77 GHz
Angle sweep step	0.1°
Polarization	Vertical –Vertical if not otherwise specified
Material	Aluminum (electric conductivity: 3.56×10^7 S/m)

Rayleigh region when R is much smaller than the signal wavelength λ ; MIE region when R is comparable to λ ; optical region when R is much larger than λ . In the Rayleigh region, $\sigma/\pi R^2$ increases linearly with respect to its radius R ; in the MIE region, this value fluctuates between peaks and troughs and a maximum $\sigma = 4\pi r^2$ appears when its circumference is equal to λ because of the constructive interference; in the optical region, the $\sigma/\pi R^2$ is always equal to 1 [Ruc70].

To estimate the total RCS of the metallic balls integrated in a road marking sample with a size of $0.15 \text{ m} \times 2 \text{ m}$ shown in Figure 3.4, a straightforward summation of all the single RCS values can be seen as an initial upper bound estimation since according to [Ric05], their total backscatter can be incoherently integrated if the balls are randomly distributed and are fully illuminated by the radar signal. The corresponding results are listed in Table 3.2 where the balls with resonance radii present a maximum result: -0.3 dBsm . If we compare this with the σ_{\min} plotted in Figure 3.1 (c), it can be inferred that this road marking can be detected at a range r larger than 30 m. However, during the practical tests, its maximum detection range is much smaller than that and the reasons can be analyzed from the following two aspects:

- assume the radar mounting height $h = 0 \text{ m}$, then the balls that can intercept the transmitted signal are only the ones that are closest to the radar, and the other balls standing behind are shielded by them. This indicates that the total area of the road marking are not appropriate for calculating the total RCS, instead, a projection area of that on the direction of the incident beam shall be utilized by multiplying the previous results with a factor $\sin \alpha = \sin(\arctan(h/d))$ where d is the ground range from radar to the road marking (d is much larger than the length of

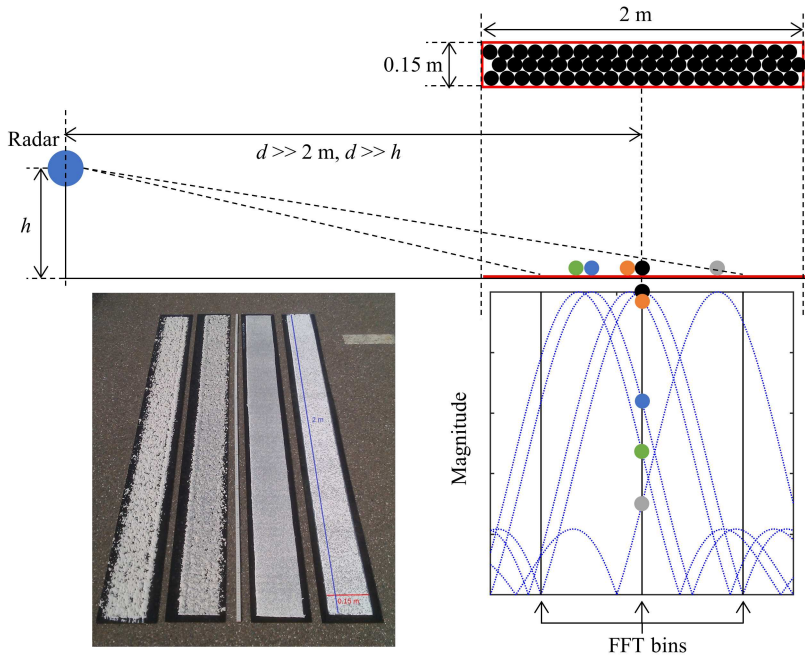


Figure 3.4: Reflection power of the spheres on a road marking are not located at the identical FFT bin, therefore their total RCS can be much smaller than the simple summation of their individual RCS values.

the road marking). With this correction, the maximum detection range ($\beta = 0^\circ, h = 0.15 \text{ m}$) decreases to about 22 m according to Figure 3.5;

- furthermore, the reflection power of all the balls are not located in a single FFT bin, but distributed across multiple bins. Refer to Figure 3.4 where five balls specified with various colors are located at different d , only part of their FFT magnitudes contribute to the total magnitude if d is not exactly at the discrete FFT bin positions. In this example, only the black ball contributes its total reflection power, while the other balls contribute only part of that instead. Additionally, as has been mentioned in section 2.2.1, this result depends also on the type of the employed

windowing function since various windowing functions have various lobe shapes.

Table 3.2: Estimation of the incoherent RCS summation of all the balls integrated in a road marking with a dimension of $0.15 \text{ m} \times 2 \text{ m}$.

R (mm)	Region	RCS (dBsm)	Number of balls	Total RCS (dBsm)
0.10	Rayleigh	-98.2	7.5×10^6	-29.4
0.20		-80.2	1.9×10^6	-17.5
0.40		-62.1	9.4×10^5	-2.4
0.62	MIE maximum	-53.2	2.0×10^5	-0.3
6.20	Optical	-39.2	1950	-6.3

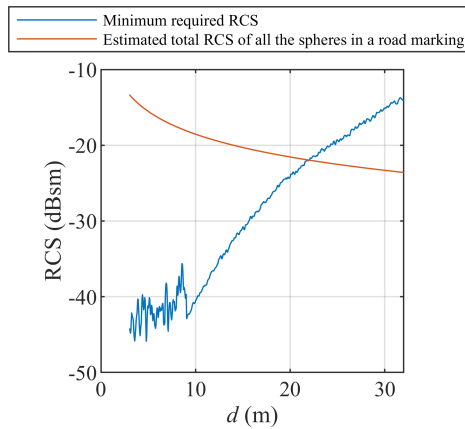


Figure 3.5: The total RCS of the metallic balls on a road marking and its corresponding maximum detection range at the intersection point with σ_{\min} ($h = 0.15 \text{ m}$).

However, adding metallic spheres has also advantages. For example, its height (diameter) is very small (only about 1.24 mm in this example); its reflection can be seen as azimuth angle independent; the fabrication is not so complicated—just add metallic balls into the road markings.

3.2.2 Cylinder, Dihedral, and Symmetrical Trihedral

Figure 3.6 (a) sketches the integration of dihedral and cylinder reflectors into the road making. The sketch shows the case where a maximum RCS of the dihedral (width of each plate: 6 mm) and cylinder (diameter: 6 mm) is achieved with the incident direction of the signal perpendicular to them and the polarization direction of the signal parallel to their geometric height direction (height is 0.15 m). Their corresponding RCS simulation results are plotted in Figure 3.6 (b) where the fluctuation of RCS can be observed when the incident signal moves away from the perpendicular direction (i.e. rotates in the propagation direction–electric field plane). For comparison, a conventional regular trihedral reflector is placed on the road marking with its hypotenuse length equal to 0.15 m.

The simulation results show that the cylinder and the dihedral present large RCS only when the incident wave is perpendicular to them, otherwise, the RCS decreases dramatically even with very small incident angle deviation. For instance, with an incident angle deviation of 10° , the RCS is already more than 30 dB smaller, indicating that when such reflectors are integrated into the road markings, a very exact incident signal direction is required. This is not feasible since the vehicle can be from any direction. It is possible to place such reflectors with all possible orientations and at any time, any one of them is perpendicular to the incident direction. However, such solution increases the fabrication complexity and requires higher fabrication precision, which also means higher cost.

Since it is not appropriate to place an up–standing trihedral between lanes, in the following sections, its bottom plate is always placed directly on the ground surface. In contrast to the dihedral and cylinder, even for a perpendicular incident angle, a trihedral presents a larger RCS than the other two. More important, with the variation of the incident angle, its RCS goes down to about 0 dBsm with an angle deviation of 40° (40 dB decrease within 40° deviation; the simulation goes up until to 45° , since above 45° , no trihedral exists any longer), which is comparable to the maximum RCS of the dihedral and the cylinder. However, the profile height of this trihedral is still too large: normally, in order not to affect the driving comfort and road safety, the height of a raised rib marking on the road is required to be between 8 mm to 11 mm on motorways and 5 mm to 8 mm on all–purpose roads [MH96]. If a

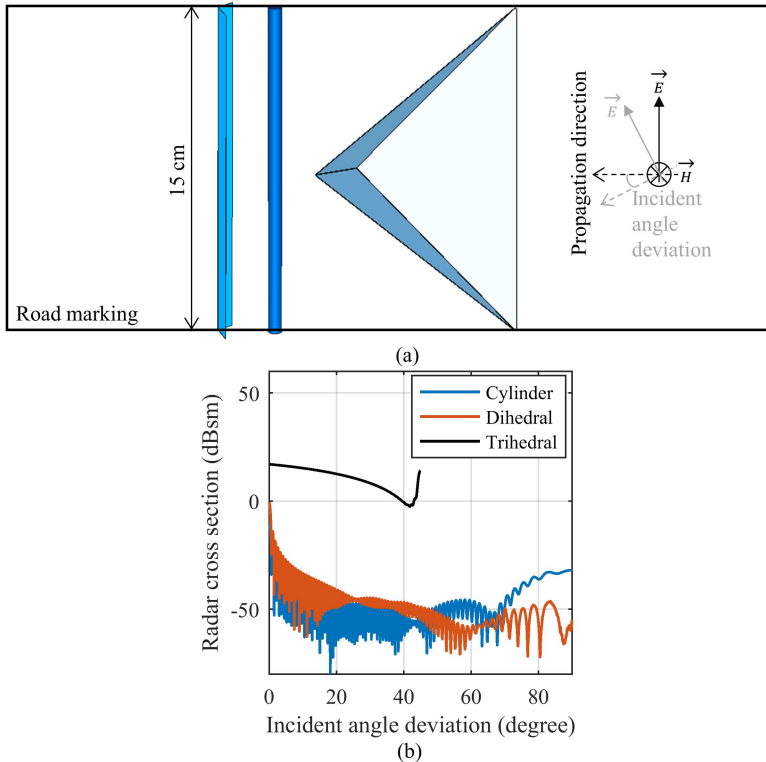


Figure 3.6: (a) Bird view: integration of dihedral, cylinder, and trihedral reflectors into road markings for radar detection. (b) Their corresponding RCS simulation results.

symmetrical trihedral with an edge length of 8 mm is employed, its maximum RCS is only about -29 dBsm. So a conventional symmetrical trihedral is also not appropriate to be used as radar road marking/marker. Fortunately, it can be seen in the following sections that with slight adjustments, a large RCS can also be achieved with a low-profile compressed trihedral.

3.2.3 Other Promising Technologies

A Van Atta Reflector contains an array of antennas (can be passive or active) that are interconnected to reradiate the received signal back in the incident direction. Ref. [Yau13] shows the simulated and measured RCS of a general planar Van Atta array with 16 and 64 elements. It can be seen from the results that for the α around 89° , which is most of the case ($h \ll d$), their RCS is about -15 dBsm to -20 dBsm. It can be seen later in section 3.3 that this RCS is smaller than that of the proposed reflector whose structure is even simpler.

The Capped Luneburg Lens is a specially fabricated spherical lens with a layer at its back spot made of radar reflective material. The incident radar beam will focus exactly on this layer and be reflected back in the parallel opposite direction of the input direction. However, this kind of reflector is expensive because of its fabrication complexity.

3.3 In-depth Reflector Analysis for Lane Detection with Automotive Radar

This section focuses on analyzing the proposed reflector in the last section—the trihedral reflector with small ingenious modifications to make it appropriate to be integrated into the road or road markings.

3.3.1 Particularity of Elevation Angle α with an Automotive Radar for Road Marking Detection

When a radar mounted at a height h is used to detect the road markings on the road surface with a ground range of d (or range r), h is much smaller than d or r at most of the time. A plot describing this can be seen in Figure 3.7 where the maximum mounting height h of the radar is assumed to be 1 m. The result proves that the focused elevation angle range for radar road marking detection is located in an elevation angle region that is close to zero degree (angle of interest) and the RCS property of the object in larger elevation angle regions can be neglected.

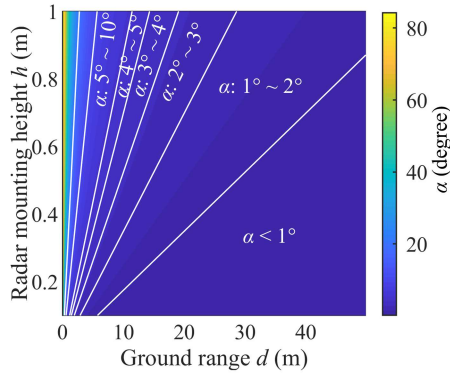


Figure 3.7: Particularity of road marking detection with automotive radar: small elevation angles dominate.

3.3.2 Symmetrical and Asymmetrical Trihedral (Type 1)

Figure 3.8 summarizes the important notations that will be frequently used in the following sections. For the reflector, its azimuth angle β denotes the azimuth angle from the symmetry axis of the bottom plate of the reflector and its elevation angle α denotes the elevation angle from its ground plate. The ground longitudinal distance from the radar to the object is d_r , the corresponding lateral distance is d_a , and their hypotenuse length—the ground range is d . For the radar sensor coordinate system, the β and α are the azimuth and elevation angles to its symmetry axis, respectively.

As been mentioned above, the height of the reflector is strictly constrained. However, its bottom area can be increased without limitation in this specific application. With the change of the ratio of the size of the standing plates to the size of the bottom plate, the angle of the maximum RCS of the trihedral in the elevation direction (denoted as α_{LP} , exclude the RCS of α at 0° and 90°) is also expected to change which will be verified in the following simulations. As an example, Figure 3.8 (b) shows such an asymmetrical trihedral with an enlarged bottom plate and minimized standing plates where the angle γ denotes whether its standing plates are perpendicular to its bottom plate, i.e. if $\gamma = 0^\circ$, they are mutually perpendicular. This condition is always fulfilled in the following description if not otherwise specified.

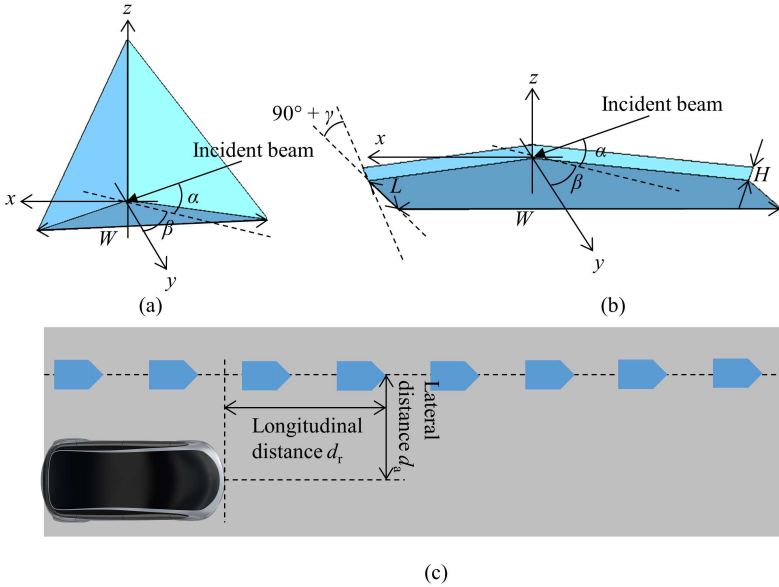


Figure 3.8: Width W , height H of the symmetrical trihedral and slant angle γ of the standing plates and length L of the extended bottom plate of the asymmetrical trihedral, azimuth angle β and elevation angle α of the incident signal. (a) Symmetrical trihedral. (b) Compressed asymmetrical trihedral. (c) Lateral distance d_a and longitudinal distance d_l between the reflectors and the radar (ground range $d^2 = d_l^2 + d_a^2$).

Figure 3.9 presents the RCS values of an asymmetrical trihedral by changing its height H with respect to the elevation angle α . The RCS of a conventional regular symmetrical trihedral with an identical bottom plate is also plotted for comparison. The results show that with reducing the size of the standing plates of the symmetrical reflector, its α_{LP} moves from about 35° to the direction of 0° . This phenomenon can also be found among the asymmetrical reflectors, for example, the one with the smallest standing plates ($H = 4 \text{ mm}$) has a α_{LP} closest to 0° . Recall the results in Figure 3.7 where small α dominates (angle of interest), compare them with the results in Figure 3.9, it can be found that this angle of interest region is located exactly at the trough RCS region of the symmetrical trihedral but at the peak RCS region of the asymmetrical trihedral, making a trihedral with smaller standing plates still have comparable or even better RCS values than the one with much larger standing plates.

This indicates that if these asymmetrical reflectors with much smaller standing plates are integrated into the road markings, they can still provide comparable RCS values compared to those with identical bottom plate but much larger standing plates. Similar conclusions can be also found in Figure 3.10 (a) and (b) where L and W are varied. Of course, the shapes of the standing plates can be further modified to fulfill specific application requirements.

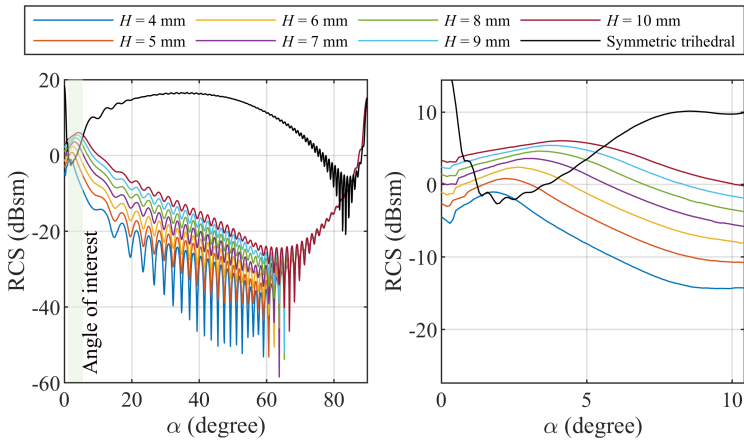
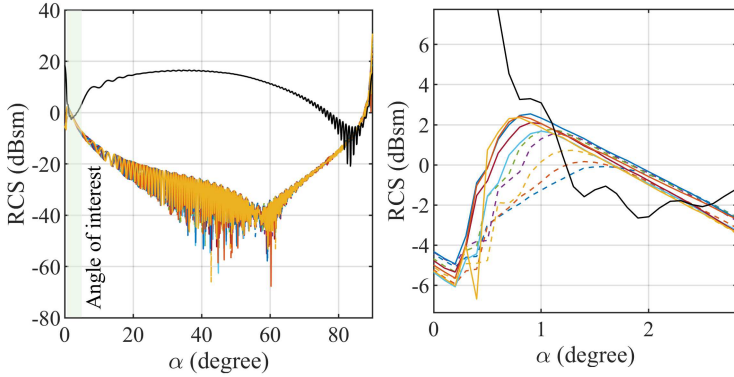
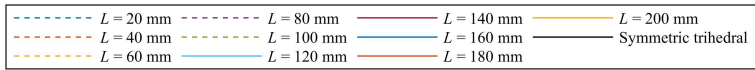


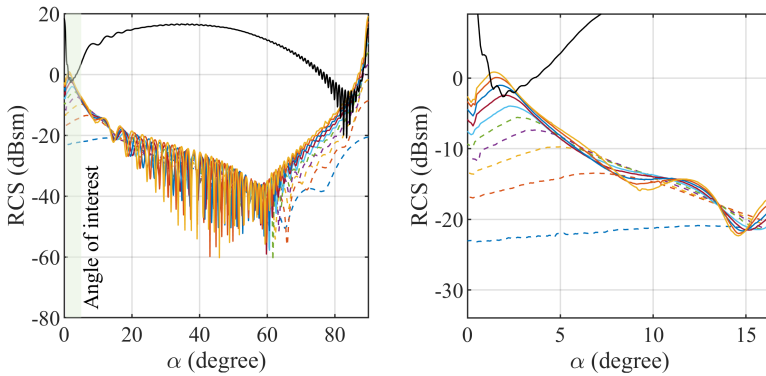
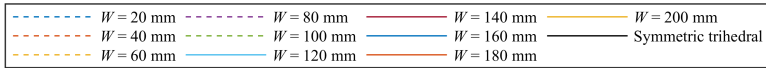
Figure 3.9: RCS of a symmetrical trihedral ($W = 160$ mm) and asymmetrical trihedrals with various H ($W = 160$ mm and $L = 0$ mm) when $\gamma = \beta = 0^\circ$. The plot at the right side zooms in the area with $\alpha < 10^\circ$ of the plot at the left side.

3.3.3 Influence of Signal Polarization on RCS

In order to figure out which signal polarization is optimal to detect the proposed reflectors, the RCS of the asymmetrical reflector ($W = 160$ mm, $H = 4$ mm, $L = 0$ mm, $\gamma = 0^\circ$, $h = 0.15$ m) under various signal polarization directions are simulated and the results are converted into d_r-d_a plots presented in Figure 3.11. From the plots, it can be concluded that the reflector poses maximum RCS when the polarization is vertical, minimum RCS when the polarization is horizontal, and values between them when the polarization direction is 45° .



(a)



(b)

Figure 3.10: RCS of a symmetrical trihedral with various (a) L ($H = 4$ mm, $W = 160$ cm) and (b) W ($H = 4$ mm, $L = 0$ mm) when $\gamma = \beta = 0^\circ$.

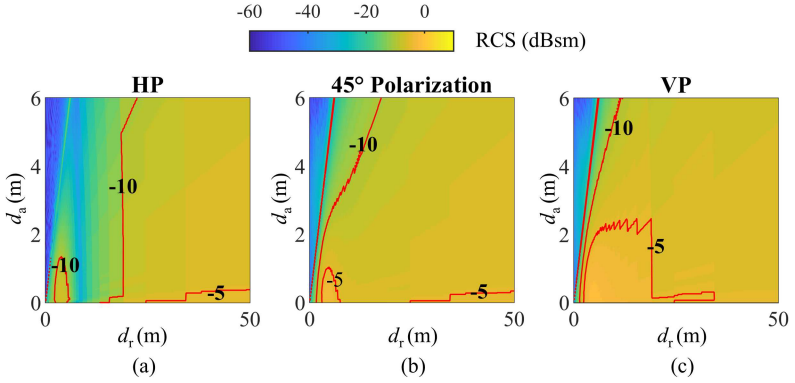


Figure 3.11: RCS comparison of an asymmetrical reflector ($W = 160$ mm, $H = 4$ mm, $L = 0$ mm, $\gamma = 0^\circ$) with various signal polarization directions ($h = 0.15$ m): (a) Horizontal polarization; (b) vertical polarization; (c) 45° polarization.

3.3.4 Asymmetrical Trihedral with Slanted Plates (Type 2)

Besides changing the shape of the standing plates, they can be also slanted ($\gamma \neq 0^\circ$). To observe how the RCS changes with various γ , corresponding simulation results are presented in Figure 3.12 with the highlighted red contours labelled with RCS values. It can be concluded from the results that the maximum RCS appears always when the three plates are mutually perpendicular and even with a small γ variation, the RCS decreases dramatically (like in the plot of $\gamma = 0^\circ$, RCS values larger than 10 dBsm dominate while in the plot of $\gamma = \pm 5^\circ$, RCS values smaller than -20 dBsm dominate). This is a very important information since these reflectors are integrated in the road markings between the lanes and they are frequently run over and pressed by the tires. From this conclusion, in order to get the optimal RCS, these reflectors are required to be fabricated as rigid as possible to avoid any structural deformation.

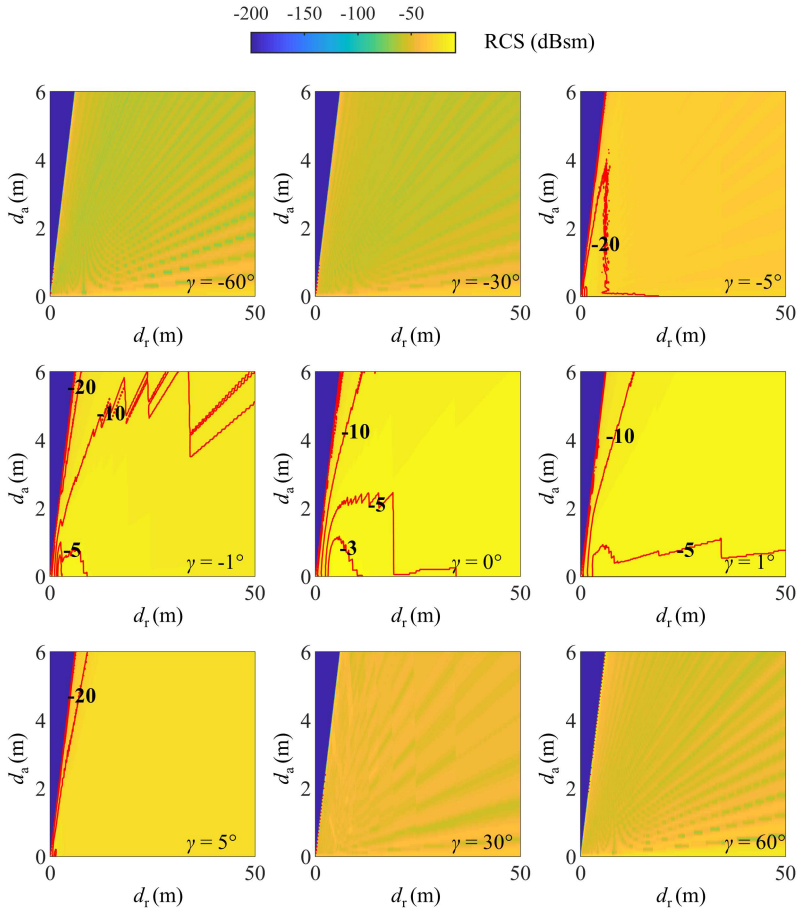


Figure 3.12: Influence of slanted standing plates on RCS with respect to d_a and d_r ($W = 160$ mm, $L = 0$ mm, $H = 4$ mm, $h = 0.15$ m).

3.3.5 Comparison Between Asymmetrical Reflector and Other Reflectors

In this section, the RCS of the metallic ball group (Type 3) that occupies the same bottom area as that of the asymmetrical trihedral ($W = 160$ mm, $H = 4$ mm, $L = 0$ mm) is calculated and represented in Figure 3.13 (b), whereas that of the asymmetrical trihedral is shown in Figure 3.13 (a). The total RCS of the spheres with their radii equal to 0.62 mm (maximum RCS in the MIE region) are calculated according to section 3.2 without considering spectrum leakage effect. Even so, its RCS in the plot is much smaller than that of the proposed asymmetrical trihedral.

Another reflector with the standing plates of Type 1 replaced by curved standing plate (Type 4) is also evaluated and presented in Figure 3.13 and its structure is illustrated in Figure 3.13 (f) with the curved standing plate created by intersecting a circle of radius R with the bottom plate. For the presented results, their height H , width W , and the total bottom length are identical to the reflector in Figure 3.13 (a). The corresponding RCS with R equal to 100 mm, 500 mm, and 1000 mm are given in Figure 3.13 (c), (d), and (e). By observing these results, it can be concluded that with a larger R , its maximum RCS at $d_a = 0$ m ($\beta = 0^\circ$) increases, however, its scattering beam width becomes smaller (RCS decreases faster at $d_a \neq 0$ m with larger R). This conclusion makes sense since if R is infinite, the standing plate can be seen as a flat and rectangular plate. So if both maximum RCS and wide backscattering beam width are required, the asymmetrical reflector (Type 1) is a better choice.

3.4 Mounting Position of Automotive Radar for Lane Detection

In this section, the influence of radar mounting position is analyzed and the reflector of Type 1 ($W = 160$ mm, $H = 4$ mm, $L = 0$ mm) is used.

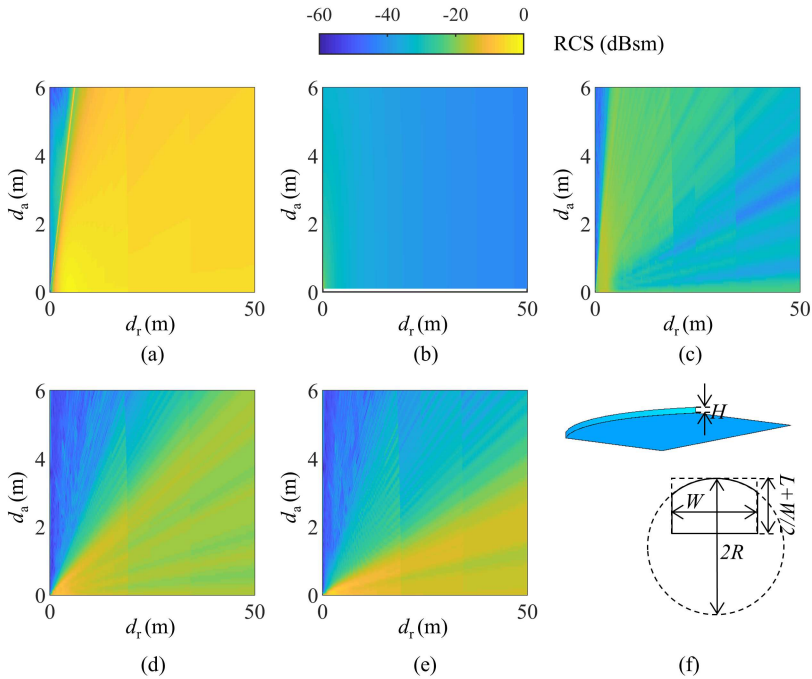


Figure 3.13: RCS comparison of various reflectors that are appropriate to be integrated into road markings for radar detection ($h = 0.15$ m). (a) Asymmetrical trihedral ($W = 160$ mm, $L = 0$ mm, $H = 4$ mm) (Type 1). (b) Metallic spheres with their occupied area equal to the bottom area of Type 1 (Type 3). (c) (d) (e) Reflector with the standing plates of Type 1 replaced by curved plates (Type 4) whose structure can be seen in (f), their R equal to 100 mm (c), 500 mm (d), and 1000 mm (e).

3.4.1 Radar Mounting Height

Figure 3.3 shows the σ_{\min} when the radar mounting height h is 0.15 m. As the antenna gain of the radar depends on α according to Figure 3.2 (b), while changing the mounting height h , the σ_{\min} also changes. Figure 3.14 (a), (b), and (c) present the σ_{\min} with larger h up to 5 m (which is actually not possible for the mounting height of an automotive radar). Figure 3.14 (d) observes the minimum required RCS at the position $x = 0$ m and $y = 30$ m when the

mounting height h is swept from 0 m to 8 m. It can be concluded from these results that with a higher mounting position, the σ_{\min} tends to become larger.

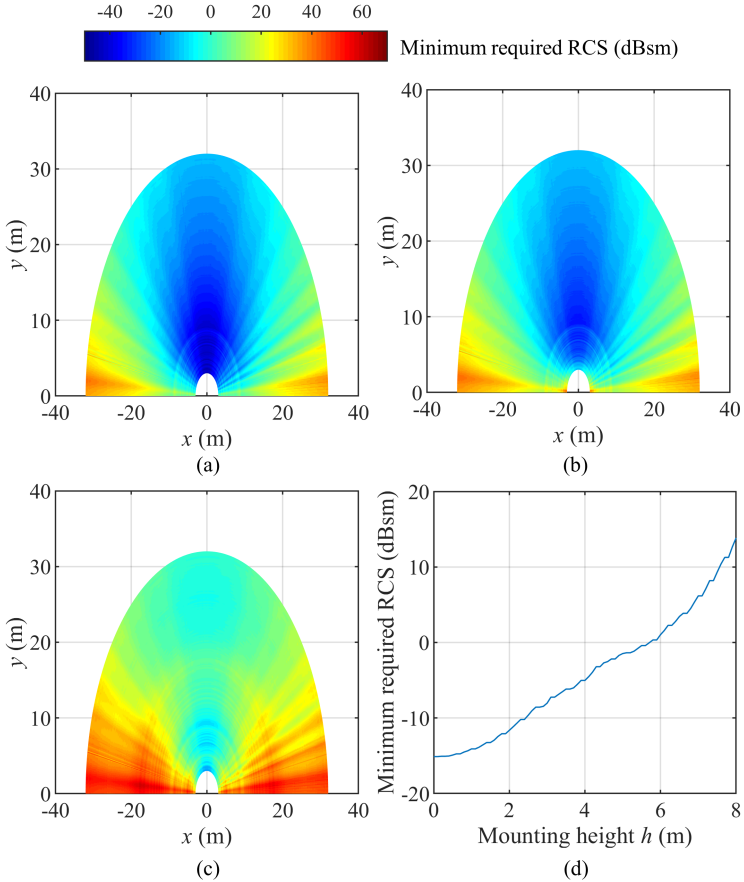


Figure 3.14: Minimum required RCS with respect to radar mounting height h . (a) $h = 0.15$ m. (b) $h = 1$ m. (c) $h = 5$ m. (d) h is swept from 0 m to 8 m ($x = 0$ m, $y = 30$ m).

Not only σ_{\min} depends on the mounting height h because of the antenna gain in vertical direction, but also the RCS of the reflector viewed from the radar depends on h . This is because the RCS of a trihedral depends on the incident angle and with various h , the elevation angle α at the identical position also

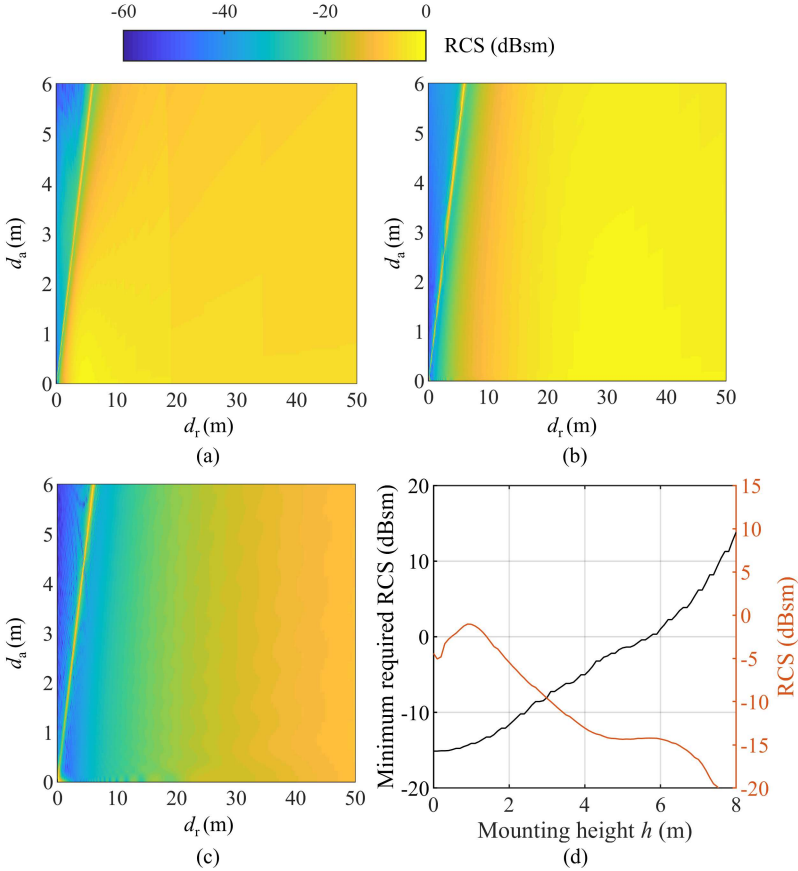


Figure 3.15: RCS of the reflector with respect to the radar mounting height h : (a) $h = 0.15$ m. (b) $h = 1$ m. (c) $h = 5$ m. (d) h is swept from 0 m to 8 m ($x = 0$ m, $y = 30$ m). The σ_{\min} (black curve) is also plotted in (d), its intersection point at $h = 2.8$ m indicates the maximum allowed radar mounting height if the reflector at $x = 0$ m and $y = 30$ m needs to be detected.

varies from the view point of the radar. Figure 3.15 (a), (b), and (c) present the RCS values that the reflector can provide to the radar with h equal to 0.15 m, 1 m, and 5 m respectively. Similar to the example above, the RCS of the reflector at the position $x = 0$ m and $y = 30$ m is plotted in Figure 3.15 (d)

in red curve. Opposite to the σ_{\min} which tends to become larger with larger h , the RCS tends to become smaller, indicating that a smaller h is always better than a larger h . Combining the σ_{\min} in black curve and the RCS of the reflector in red curve in Figure 3.15 (d), the maximum allowed h can be calculated from their intersection point, meaning that if such a reflector at this position needs to be detected by this radar, the mounting height of the radar shall be smaller than this limit, i.e., about 2.8 m in this example.

3.4.2 Radar Mounting Orientation

This section focuses on the influence of radar orientation on the σ_{\min} . Figure 3.16 depicts the orientation variation of the radar in both elevation (α') and azimuth (β') directions.

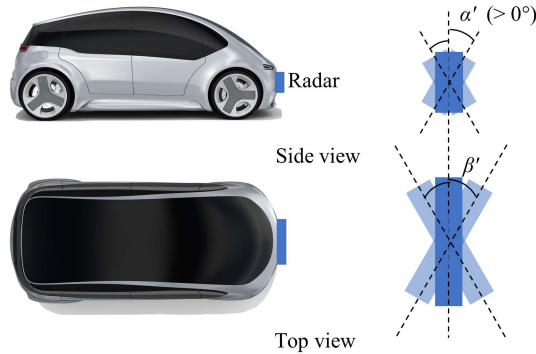


Figure 3.16: Change of the radar orientation both in elevation (α') and azimuth direction (β').

Figure 3.17 (a) to (e) present the σ_{\min} when α' equals to -80° , -30° , 0° , 30° and 80° respectively. Figure 3.17 (f) shows the same result but with the α' sweeping from -89° to 90° together with the RCS that the reflector can provide at the position $x = 0$ m and $y = 30$ m. The results indicate that no matter the radar is orientated to top or bottom, the σ_{\min} always tends to increase. For a reflector (Type 1, $W = 160$ mm, $H = 4$ mm, $L = 0$ mm) at the position $x = 0$ m and $y = 30$ m, the maximum allowed orientation variation in elevation direction is about $\pm 7^\circ$.

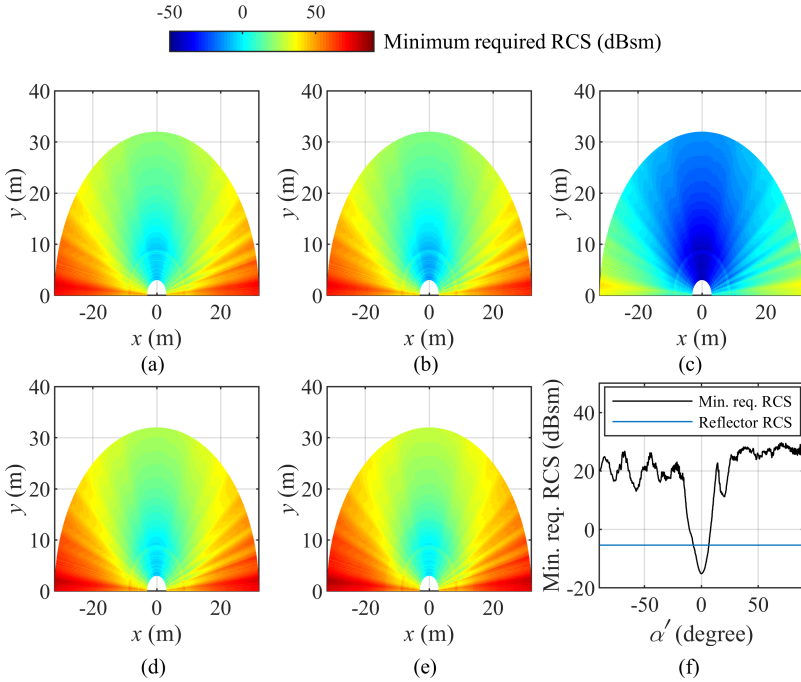


Figure 3.17: Influence of α' on σ_{\min} : (a) $\alpha' = -80^\circ$; (b) $\alpha' = -30^\circ$; (c) $\alpha' = 0^\circ$; (d) $\alpha' = 30^\circ$; (e) $\alpha' = 80^\circ$. (f) σ_{\min} (black curve) and the RCS of the reflector (blue curve) at the position of $x = 0$ m and $y = 30$ m with respect to α' ($h = 0.15$ m).

Restricted by its smaller antenna gain in larger azimuth angle, σ_{\min} with larger β also gets larger. To solve this problem, multiple radar sensors can be simultaneously mounted into the car and when the radar road marking is detected by any of these mounted radars, it is recognized to be detected, meaning in the overlapped area of the individual σ_{\min} of all these radar sensors, their minimum one is the actual σ_{\min} . Figure 3.18 (a) shows a vehicle of 2 m width equipped with three radar sensors: one front radar mounted in the middle of the front bumper and two corner radar sensors mounted at two sides of the vehicle bumper with a distance of 2 m and the azimuth orientation β' of 40° . With this configuration, the radar road marking can be detected in a wider azimuth angle

range. Figure 3.18 (b) plots the corresponding σ_{\min} considering the individual σ_{\min} of all the three sensors.

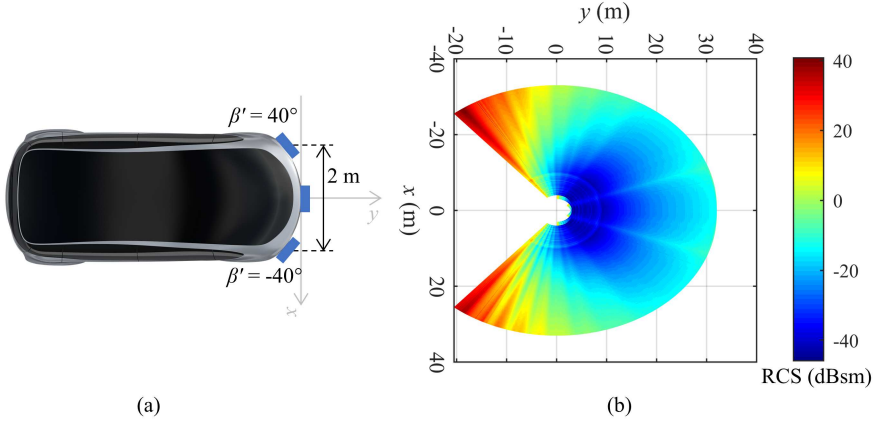


Figure 3.18: Combine three radar sensors for road marking detection: (a) two corner radar sensors with $\beta' = \pm 40^\circ$ and a front radar sensor with $\beta' = 0^\circ$; (b) its consequent σ_{\min} .

3.5 Influence of Road Curve on RCS

3.5.1 Vertical Road Curve

Preceding sections consider only the vehicles and the reflectors on a flat surface. However, in reality, the vehicle can encounter roads with vertical curved profile like the one illustrated in Figure 3.19 (a). Normally, the road vertical profile can be described by the following equation:

$$\text{Height} = g_1 y + \frac{(g_2 - g_1)y^2}{2L_c} \quad (3.6)$$

where g_1 and g_2 are the initial and end grades of the curved road and L_c the length of the curve. When the curve tends to be flat, its behavior is close to that of a flat road that has been discussed previously. In the following part, another extreme case—the maximum curvature will be evaluated, like the one

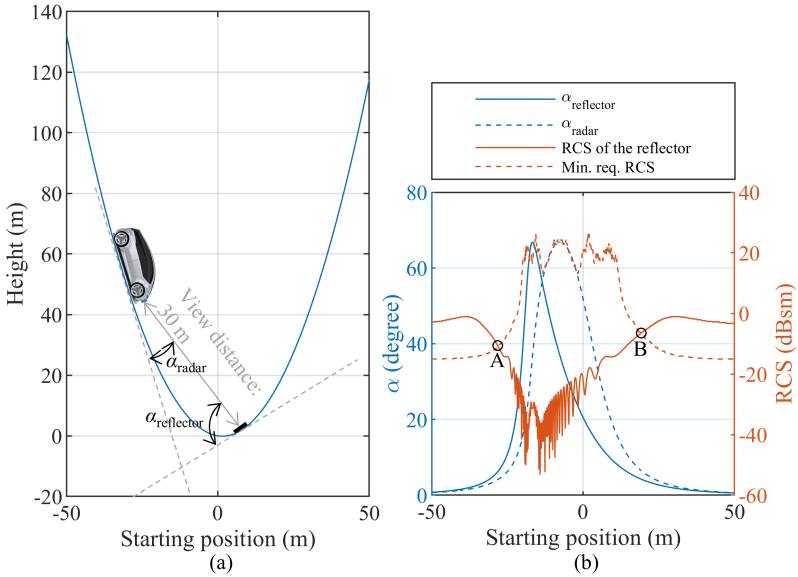


Figure 3.19: (a) Illustration of a vehicle and radar road marking on a road with vertical curved profile. (b) Corresponding σ_{min} and the RCS of the reflector at a view distance of 30 m to the radar when the vehicle is located at different positions in (a). This result indicates that between points A and B, a reflector at a view distance of 30 m to the radar is not able to be detected.

in Figure 3.19 (a) where $L_c = K|g_1 - g_2|$ with $K = 10$, $g_1 = -15\%$, and $g_2 = 15\%$ [oSHO04], [FOTb], [FOTa]. A position in front of the radar with the view distance of 30 m ($\beta = 0^\circ$) is selected to be observed. The calculation result of the RCS of the reflector (solid red curve) and the σ_{min} (dashed red curve) are plotted in Figure 3.19 (b) correspondingly, which indicates that in this extreme situation, i.e. when the vehicle moves to the trough region, the σ_{min} increases whereas the RCS of the reflector decreases, leading the reflector not to be capable of being detected. Figure 3.19 (b) shows that the radar can not detect the reflector at a view distance of 30 m between the positions A and B. Consequently, the detection of the radar road marking can be restricted under certain road structure conditions and it is always necessary to calculate to check its feasibility when they are built.

3.5.2 Horizontal Road Curve

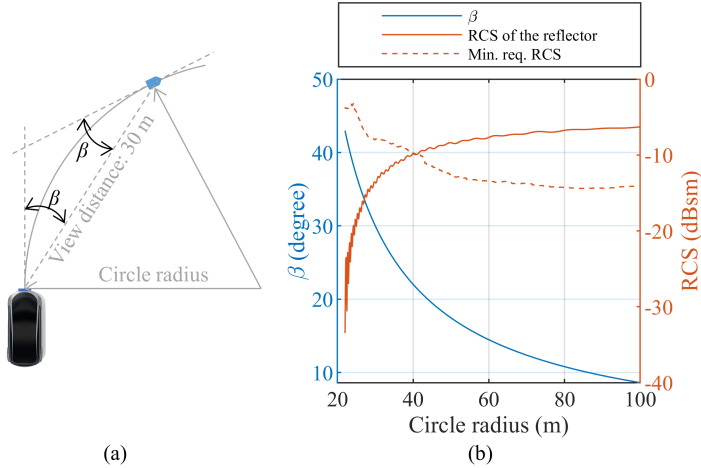


Figure 3.20: (a) Illustration of a vehicle and radar road marking on a road with horizontal curved profile. (b) Corresponding σ_{\min} and the RCS of the reflector at a view distance of 30 m to the radar with respect to the radius of the road. The result shows that when the radius of the road is smaller than 40 m, the reflector at a view distance of 30 m to the radar is not able to be detected.

The vehicle can also frequently encounter horizontal road curves like the one shown in Figure 3.20 (a). In this example, the horizontal road curve is modeled with a circle defined by its radius. The orientations of the reflector and the radar are both tangential to this circle. Similarly, the detection of the reflector at the view distance of 30 m is observed with changing the radius of the circle from 22 m to 100 m. The corresponding β (both for radar and reflector), RCS of the reflector (solid red curve), and the σ_{\min} (dashed red curve) are calculated and plotted in Figure 3.20 (b). It is obvious that a horizontal road curve with smaller radius will make the reflector undetectable by the radar. This is influenced by two factors: with smaller radius, the β of the radar and the reflector both get larger, which indicates a smaller horizontal antenna gain and a smaller reflector RCS. In this example, if the radar wants to detect the reflector at its view distance of 30 m, the radius of the circle shall be at least larger than 40 m (intersection points between solid and dashed red curves). To make the detection more robust, as has been mentioned in section 3.4.2, several

radars with various orientations can simultaneously be mounted into the car, and the orientation of the reflectors located at the horizontal road curve can also be adjusted i.e. to combine several reflectors with various orientations, this will be introduced more in details in section 4.3.3.

3.6 Dynamic Simulation of Radar-detectable Road Markings

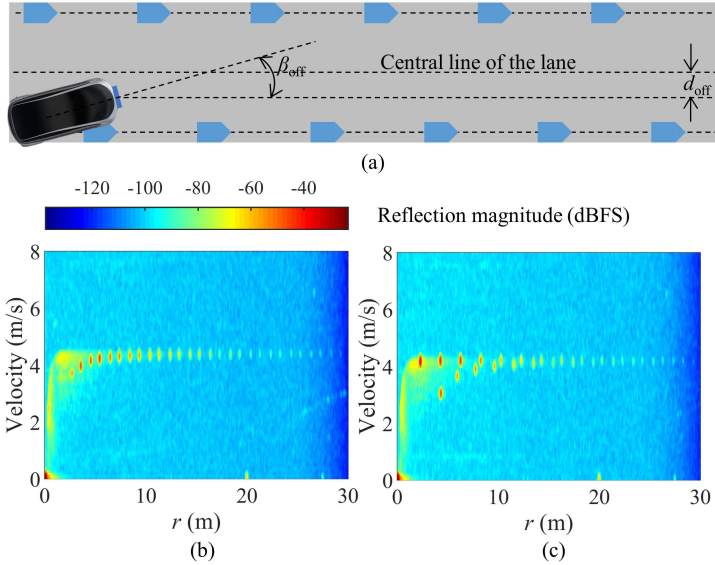


Figure 3.21: (a) Parameter definition: offset distance d_{off} from the central line of the lane and orientation deviation β_{off} from the lane direction. (b) Range-Doppler plot with $d_{\text{off}} = 0$ m and $\beta_{\text{off}} = 0^\circ$. (c) Range-Doppler plot with $d_{\text{off}} = 1.5$ m and $\beta_{\text{off}} = 0^\circ$ (lane width: 3 m).

Figure 3.21 (b), (c) present the measurement results when the vehicle equipped with a radar at its front drives along the lane defined by the reflectors positioned at both lane borders (lane width: 3 m) with $d_{\text{off}} = 0$ m, $\beta_{\text{off}} = 0^\circ$ and $d_{\text{off}} = 1.5$ m, $\beta_{\text{off}} = 0^\circ$ (d_{off} is the offset distance from the central line of the lane and β_{off} is the orientation deviation of the vehicle from the lane direction as

illustrated in Figure 3.21 (a)). Two curves are formed by their reflection points in the Range–Doppler plots: in Figure 3.21 (b), the two curves overlap with each other; in Figure 3.21 (c), the two curves diverge from each other. This characteristic can be exploited to indicate whether the vehicle departs from the lane and will be discussed more in details with the help of the simulation data in the following part.

3.6.1 Lateral Localization of the Vehicle

Figure 3.22 shows a vehicle driving along the lane direction ($\beta_{\text{off}} = 0^\circ$) with a velocity of 10 m/s and two different d_{off} : one with $d_{\text{off}} = 0$ m in Figure 3.22 (b), (c) and the other with $d_{\text{off}} = 1$ m in Figure 3.22 (d), (e). The radial velocity of the reflectors and their Range–Doppler plots are both presented. Since the results of Range–Doppler and radial velocity results match with each other (it makes sense since the velocity measured by the radar is actually the radial velocity), in the following section, only the radial velocity plots will be used. It can be easily concluded from these results that with a certain driving velocity, the separation of the curves with larger d_{off} is also larger. When the vehicle drives perfectly along the middle line of the lane (radar is mounted in middle of the front bumper), these curves overlap perfectly with each other. This can be very useful for functions like LDW, LKS, etc. to determine whether the vehicle is running exactly in the middle of the lane or not. Besides, in order to know to which side of the lane the vehicle is closer to, the intervals of the reflectors at both sides of the lane can be set differently (the side corresponding to the curve with higher velocity in the Range–Doppler plot indicates the side that the vehicle is closer to).

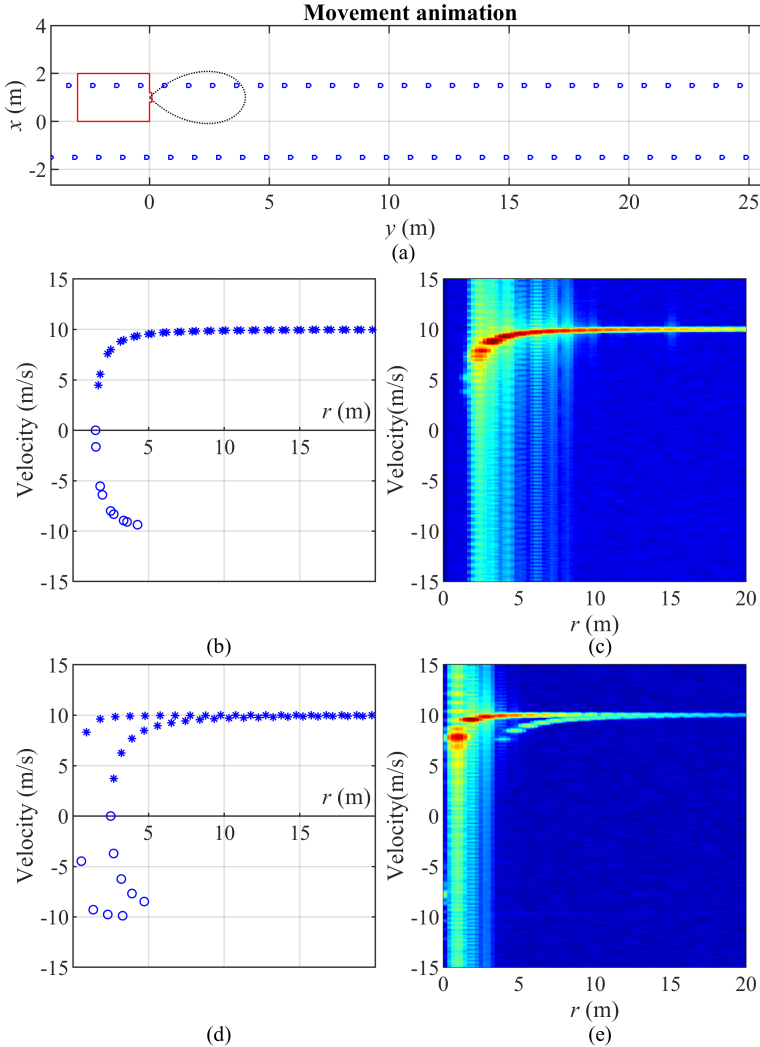


Figure 3.22: (a) Movement animation with $d_{\text{off}} = 1$ m and $\beta_{\text{off}} = 0^\circ$. Radial velocity of every reflector (b) with $d_{\text{off}} = 0$ m and $\beta_{\text{off}} = 0^\circ$, (d) with $d_{\text{off}} = 1$ m and $\beta_{\text{off}} = 0^\circ$, and (c) (e) their corresponding Range-Doppler results from signal processing. The circles in (b) and (d) come from the reflectors behind the radar.

3.6.2 Determination of the Vehicle's Orientation

When the vehicle does not drive along the lane direction ($\beta_{\text{off}} \neq 0^\circ$), the curves in the Range–Doppler plot behave differently: a peak coming from the reflector that is directly located at the driving direction appears in the curve, and with changing β_{off} , the position of this peak changes accordingly. Figure 3.23 presents the results with $\beta_{\text{off}} = 30^\circ, 45^\circ,$ and 60° . The peak, which has the same velocity as the vehicle moves to the direction of smaller r with larger β_{off} . Besides, the curve slope at the peak also gets larger with a larger β_{off} . So by observing the shape of this curve, the driving orientation of the vehicle can also be inferred.

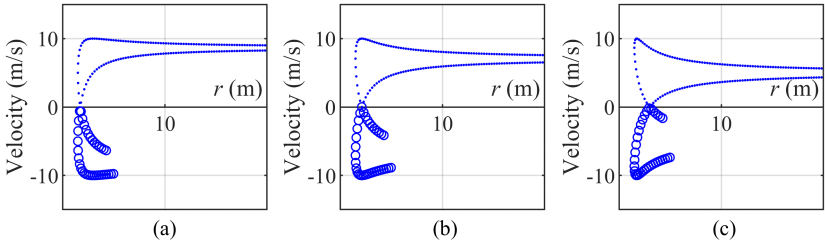


Figure 3.23: Radial velocity of the reflectors with respect to β_{off} : (a) 30° , (b) 45° , and (c) 60° . The circles in the plots come from the reflectors behind the radar.

3.6.3 Oncoming Horizontal Road Curve

The Range–Doppler characteristics can additionally also be used to indicate the oncoming road curve and its curvature. Figure 3.24 shows the plots when the vehicle is approaching a horizontal road curve with various radii. Different to a straight lane where the curves in the Range–Doppler plot tend to converge as r increases, an approaching road curve makes them to diverge oppositely. Furthermore, the divergence of the curves depends on the road curvature itself if the velocity and the lane width are already known. This can be used to indicate the oncoming road curve and to estimate the radius of the road curve, which is a very important information for velocity and steering adjustment of a vehicle before approaching a road curve.

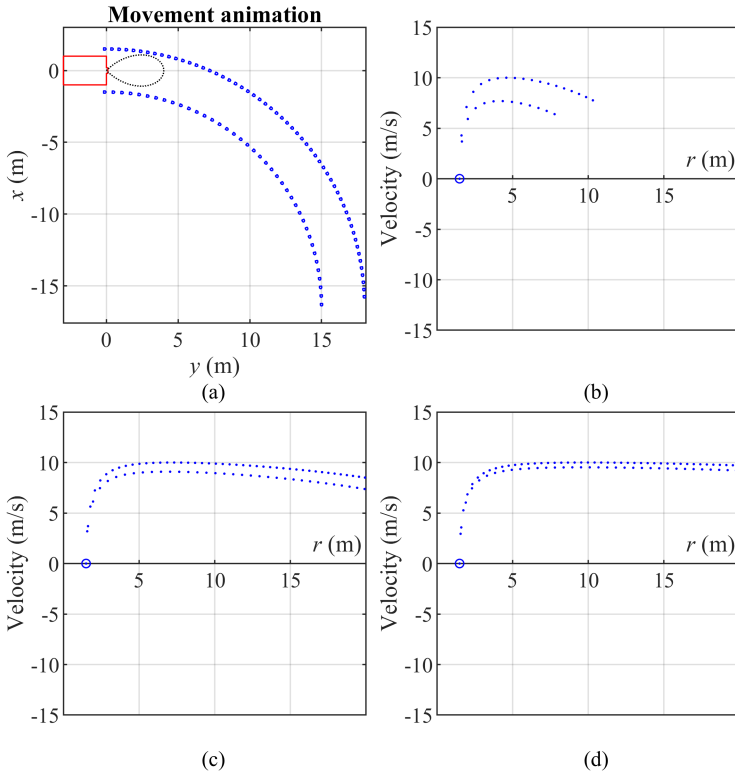


Figure 3.24: (a) The vehicle with a radar mounted at its front drives towards the road with horizontal curvature and the influence of the radius of the road on the radial velocity characteristic of the reflectors. The radii are (b) 5 m, (c) 15 m, and (d) 30 m.

3.6.4 Summary

It is not possible to list all possible scenarios and their corresponding Range–Doppler characteristics, but even the most complex ones can be decomposed into several simpler ones. Tools like pattern recognition or neural network can be employed to determine the vehicle lateral position, orientation or oncoming road curve by utilizing the Range–Doppler results as their input.

4 Radar Road Marking Reflection Measurements on Test Tracks

The preceding chapter presents the minimum required RCS of the radar and the simulated RCS values of various reflectors. In this chapter instead, corresponding on-road measurement results are presented.

4.1 Measurement Setup and General Considerations

4.1.1 Samples under Measurement

According to the results of the analysis in chapter 3, the preferred reflector type in this chapter is focused on Type 1. Such a specimen for on-road measurement can be seen in Figure 4.1 (a) whose surface is made of 0.2 mm thick aluminum foil and is glued on styrofoam as the carrier. Specimens of various dimensions of Type 1 are measured in order to evaluate the influence of H , W , and L on the reflection magnitude. In order to make the following description more compact, these specimens are divided into 3 groups and are represented by $\text{GH}(N)$, $\text{GW}(N)$, and $\text{GL}(N)$ where N is used to denote their variations in height (i.e. GH), width (i.e. GW), and length (i.e. GL) correspondingly. An additional group $\text{G}(N)$ including specimens with identical dimension is used to verify the repeatability of the measurements. Table 4.1 summarizes all the dimensions of these specimens and as an example, a specimen represented with $\text{GW}3$ has a height H of 4.3 mm, W of 140 mm and L of 117 mm.

Figure 4.1 (b) shows one specimen of Type 3 whose area of the bottom plate is identical to that of the specimen $\text{G}(N)$, but with its aluminum foil and standing plate replaced by aluminum balls. Figure 4.1 (c) shows one specimen

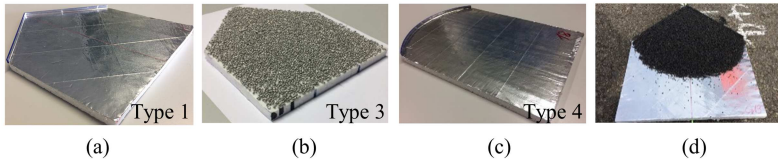


Figure 4.1: Specimens for on-road measurements: (a) Type 1, (b) Type 3, (c) Type 4, and (d) Type 1 with its corner region covered by gravel.

Table 4.1: Dimension of the specimens (Type 1) under on-road measurements.

Sample	H (mm)	W (mm)	L (mm)
$GH(N)$	N	160	117
$GW(N)$	4.3	$100+20(N-1)$	117
$GL(N)$	4.3	160	$20(N-1)$
$G(N)$	4.3	160	117

of Type 4 with the standing plates of Type 1 replaced by curved standing plate with an identical height. In practice, the road markings can also be covered by other materials like water, gravel, and leaves, etc. In order to investigate this influence, specimens of Type 1 covered by various materials are measured and Figure 4.1 (d) shows such a specimen with its corner region fully covered by gravel with the diameter between 0.7 mm and 1.2 mm.

4.1.2 Measurement Setup and Procedure

During the measurements, the specimens are placed in a line on a flat ground one after the other and oriented towards the driving direction of the test vehicle. The test vehicle is equipped with a radar at its front ($h = 0.15$ m) and drives towards the specimens with $d_a = 0$ m (thus, $d = d_r$). To measure the orientation influence of the specimens on the reflection power, they are rotated by an angle β away from the driving direction of the vehicle like shown in Figure 4.2. The reflection magnitudes of all the specimens are extracted from the Range-Doppler results. The corner S of Figure 3.1 and its reflection magnitude

$M_{\text{corner S}}$ are reused. With all the above information, the RCS of the specimens under measurement can be calculated according to:

$$\sigma_s(d, \beta) = \sigma_{\text{corner S}} - (M_{\text{corner S}}(d) - M_s(d, \beta)) + \text{Comp}_V(d) \quad (4.1)$$

where $\sigma_{\text{corner S}}$ is the RCS of the reference corner S, $M_{\text{corner S}}(d)$ is the reflection magnitude of corner S with respect to d after eliminating multi-path reflection (curve fit 3 in Figure 3.1 (b)), and Comp_V is used to compensate the antenna gain difference between the standing reference corner S and the measured specimen placed directly on the ground surface at the distance d according to Figure 3.2.

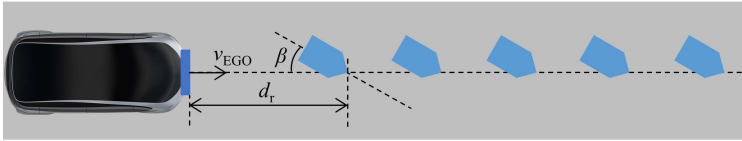


Figure 4.2: Top view of the measurement setup.

4.2 Evaluation of Measurement Results

In this section, the repeatability of the measurements is verified at first. Based on this, the measurement results of Type 1, 3, 4, etc and the influence of external coverings will then be presented and discussed. The last part summarizes the SNR and maximum detection range of the reflectors during the measurements.

4.2.1 Repeatability of the Measurements

In order to verify the repeatability of the measurements, four separate tests of the specimens in group $G(N)$ with identical dimension and orientation ($\beta = 0^\circ$) are conducted. Their reflection magnitudes and the corresponding averaged one over all these measurements and specimens are plotted in Figure 4.3. For the same specimen under separate and repeated measurements, the amplitude variation is below 3 dB. However, the reflection magnitude difference between different specimens, even with identical dimensions, can be up to 6 dB. This

difference can be caused by the specimens themselves since it can not be guaranteed that all these specimens are perfectly identical because errors can be introduced during the handcrafted fabrication process. When calculating their RCS, their averaged reflection magnitude (black curve in Figure 4.3) is used. Together with the reflection magnitude of the reference corner S, the estimated RCS of specimen $G(N)$ is plotted in Figure 4.4 in red solid curve. Simultaneously, its simulated RCS is also plotted in red dashed curve for comparison.

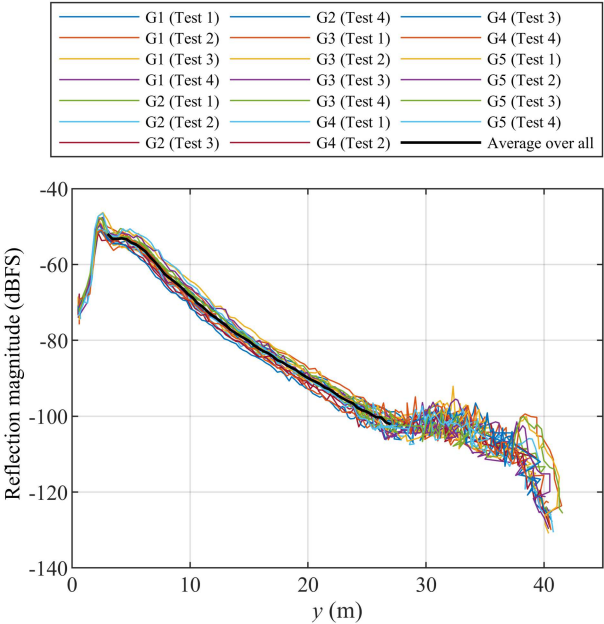


Figure 4.3: Reflection magnitudes of specimens $G(N)$ under various tests and their corresponding average magnitude.

In Figure 4.4, the simulated and measured RCS are very close to each other although small discrepancy is still visible. Such discrepancy can be caused by the following reasons: 1) the large ground of the test field shall be seen as part of the bottom plate of the reflector, regardless of its much smaller permittivity when compared with that of the aluminum foil. This effect is however not considered in the simulation; 2) in an on-road measurement,

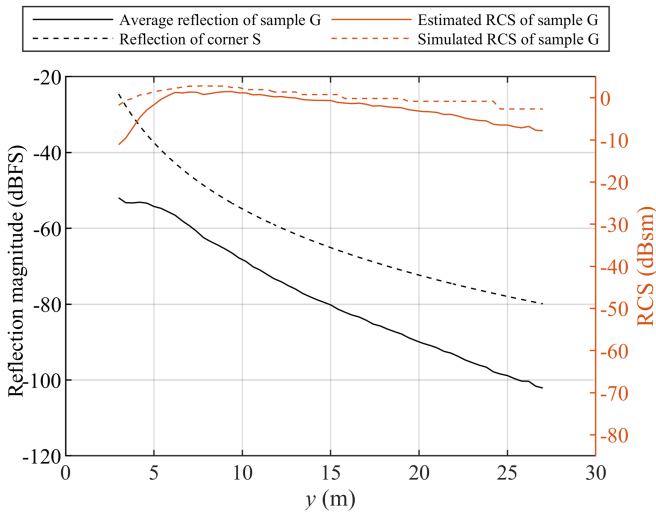


Figure 4.4: Estimated RCS of specimen $G(N)$ from the on-road measurement and its simulated RCS.

it can not be guaranteed that the ground is perfectly flat and small elevation angle deviations can be introduced to the tested specimens at various positions, because their RCS is very elevation angle sensitive, this may also contribute to the discrepancy between estimated and simulated values. To summarize, except such small discrepancies, all the results match very well with each other and with the simulation results (the theoretic results), so the measurements can be seen both reliable and repeatable.

4.2.2 Type 1

Different to chapter 3.3 where the influences of H , L , and W on the RCS are simulated, in this section, the corresponding results from the on-road measurements are presented in Figure 4.5 and Figure 4.6. W in the measurements are set to be larger than 100 mm which is normally the minimum width of a road marking. All the results are normalized with respect to the maximum reflec-

tion magnitude in its group, i.e., that with maximum H , L , W (Figure 4.5), and $\beta = 0^\circ$ (Figure 4.6) is set to be 0 dB.

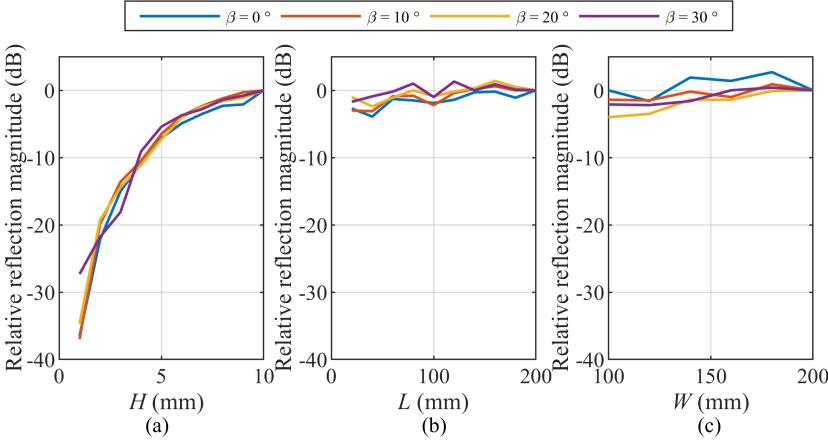


Figure 4.5: On-road measurement results: influence of the dimension of Type 1 on the reflection magnitude with various (a) H , (b) L and (c) W .

For the specimens in group $GH(N)$, with H increasing from 1 mm up to 10 mm (Figure 4.5 (a)), the reflection magnitude increases about 35 dB. However, the rate of the increment gets smaller with larger H , for example, the magnitude increases about 15 dB when H changes from 1 mm to 2 mm, but only 1 dB when H changes from 9 mm to 10 mm. It can be expected that with further increased H , its reflection performance will not really become better. The reflection dependency of these specimens on β in Figure 4.6 (a) indicate that with a β smaller than 20° and 30° , the decrease of the reflection magnitude is smaller than 3 dB and 9 dB, respectively. A simulation of the influence of β on the reflection magnitude of $G(N)$ is also plotted in the black curve for comparison with its elevation angle α being swept from 0° to 5° with a step size of 0.1° (the plotted curve is the averaged value across all the α).

Figure 4.5 (b), (c) present the influences of L and W on the reflection magnitude. Different to that of H in (a), the magnitude difference with larger L and W is relative small: 5 dB either when L changes from 20 mm to 200 mm or when W changes from 100 mm to 200 mm. So for the reflector of Type 1, since its standing plates are much smaller than its bottom plate ($W \gg H$ even

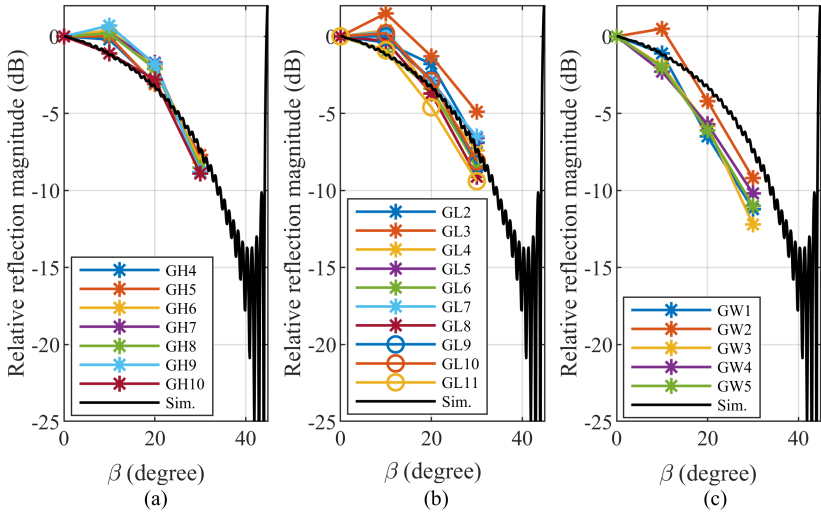


Figure 4.6: On-road measurement results: azimuth angle dependency of the reflection magnitude of (a) $G(N)$, (b) $GL(N)$ and (c) $GW(N)$. Simulation results in black curves are plotted for comparison.

when $L = 0$ mm), H has the largest impact on its reflection magnitude when compared with L and W and such impact also gets smaller when H increases. In contrast, changing the signal incident angle β of all these specimens result in a similar reflection magnitude decrement that is not so dramatic, which also proves the advantage of such kind of reflector for radar-based lane detection.

4.2.3 Type 1 and Type 3

Figure 4.7 shows the reflection magnitude of specimen $G(N)$ of Type 1 and specimen of Type 3 shown in Figure 4.1 (b) with the identical bottom plate of $G(N)$ occupied fully with aluminum balls (1.3 mm diameter). The plotted results show that the reflection magnitude of $G(N)$ is about 15 dB larger than that of Type 3. As mentioned previously, one advantage of Type 3 comes from its isotropic reflection characteristic, by taking the results of Figure 4.6 into account, a reflection magnitude decrease of 15 dB corresponding to an incident angle β up to 40° shall be considered. So this advantage of Type 3

over Type 1 is not so obvious any more whereas the reflection of Type 1 can be much larger than that of Type 3. Another advantage of Type 3 is its smaller height (diameter of one single ball): when the height of Type 1 gets smaller, its reflection magnitude is also smaller. However, the RCS of the balls have already reached their maximum value according to Table 3.2 whereas that of Type 1 can be even higher with a larger H .

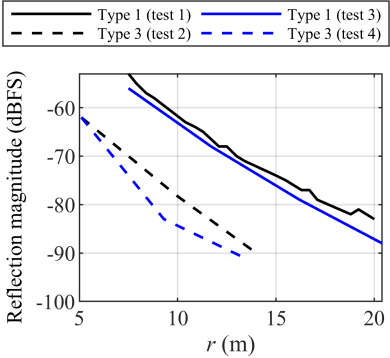


Figure 4.7: Reflection magnitude difference between Type 1 and Type 3. Four separate testes are carried out ($\beta = 0^\circ$).

4.2.4 Type 1 and Type 4

Figure 4.8 presents three measurement results of specimen 1 of Type 1 (a), specimen 2 of Type 4 with $R = 100$ mm (b), and specimen 3 of Type 4 with $R = 500$ mm (c) and all these specimens have identical height $H = 4.3$ mm, width $W = 160$ mm and bottom length $L + W/2 = 197$ mm.

It can be seen from these measurement results that with $\beta = 0^\circ$, the reflection magnitude of specimen 2 is about 10 dB smaller than that of specimen 3, whose reflection magnitude is close to that of specimen 1. However, as β gets larger, the reflection magnitude of specimen 2 keeps nearly unchanged whereas that of specimen 3 presents a dramatic decrease of about 20 dB. This decrease with respect to β exists also for specimen 1 which is however more moderate. This moderate decrease makes the reflection magnitude of specimen 1 close to that of specimen 2 at $\beta = 20^\circ$ and for even larger β , the reflection

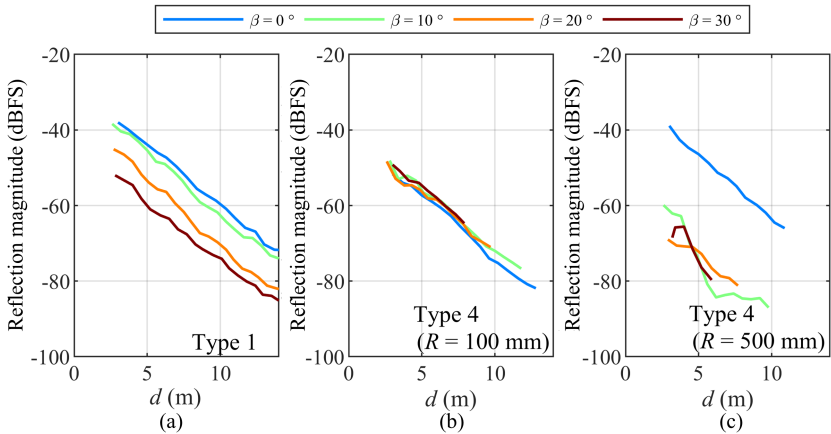


Figure 4.8: Reflection magnitude difference between (a) specimen 1 (Type 1), (b) specimen 2 (Type 4 with $R = 100$ mm), and (c) specimen 3 (Type 4 with $R = 500$ mm). All these specimens have identical height $H = 4.3$ mm, width $W = 160$ mm and bottom length $L + W/2 = 197$ mm.

magnitude of specimen 2 is larger than that of specimen 1. Both results in Figure 3.13 and the measurement results in Figure 4.8 indicate that with a larger curvature, the maximum RCS of Type 4 gets smaller but its reflection angle range gets large and with smaller curvature, its maximum RCS gets larger but its reflection angle range becomes very small. So it is possible to integrate Type 4 with an appropriate curved standing plate into road markings for radar detection. However, from the perspective of fabrication process, a curved plate is more complex than a straight plate since its curvature needs to be precisely controlled. And it can be seen later that by combining two specimens of Type 1 with opposite orientations, four reflectors are created, whereas for Type 4, only two reflectors are created which is less efficient from the perspective of material usage.

4.2.5 Reflector with Covering

When the road marking is integrated on the road surface, it is possible that it is covered by certain materials like water, graves, leaves, etc. Table 4.2

presents the measurement results of the specimens $G(N)$ that are covered by these materials and all the results are normalized to the one without covering. To measure the influence of water coverage, three specimens with identical dimensions are employed with the first one without covering, the second one covered with a dry sponge in the corner region, and the last one covered with a sponge containing water, like shown in the illustration of Figure 4.9. From the measurements, the reflection magnitude from the empty reflector and the one with dry sponge present nearly no difference, and for the one covered with sponge including 20 g and 30 g water, the reflection magnitude decreases about 23 dB and 25 dB, respectively. This is not desirable and can be avoided by raising the corner side of the reflector with a small angle α_{raise} to prevent water accumulating in the corner region like the one shown in Figure 4.10 (a). Figure 4.10 (b), (c), and (d) give the corresponding RCS of the same reflector when α_{raise} equals to 0° , 1° , and 2° . It can be seen from the results that with this small raise, the reflector still delivers very similar RCS values compared to the one without raise. Other coverings like gravel and leaves also cause large reflection magnitude decrease according to Table 4.2, for which a good and feasible solution is still needed.

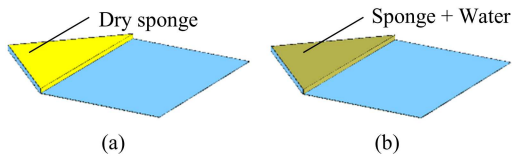


Figure 4.9: Water coverage measurement setup. (a) Reflector with its corner region covered by dry sponge as reference. (b) Reflector with its corner region covered by sponge containing water.

Table 4.2: Influence of coverings on reflection magnitude.

Sample	Relative reflection (dB)	Sample	Relative reflection (dB)
No covering	0	+ 54 g Water	-30
+ 50 g Gravels	-27	+ 8 g Leaves	-27
+ 20 g Water	-23	+ 16 g Leaves	-32
+ 30 g Water	-25		

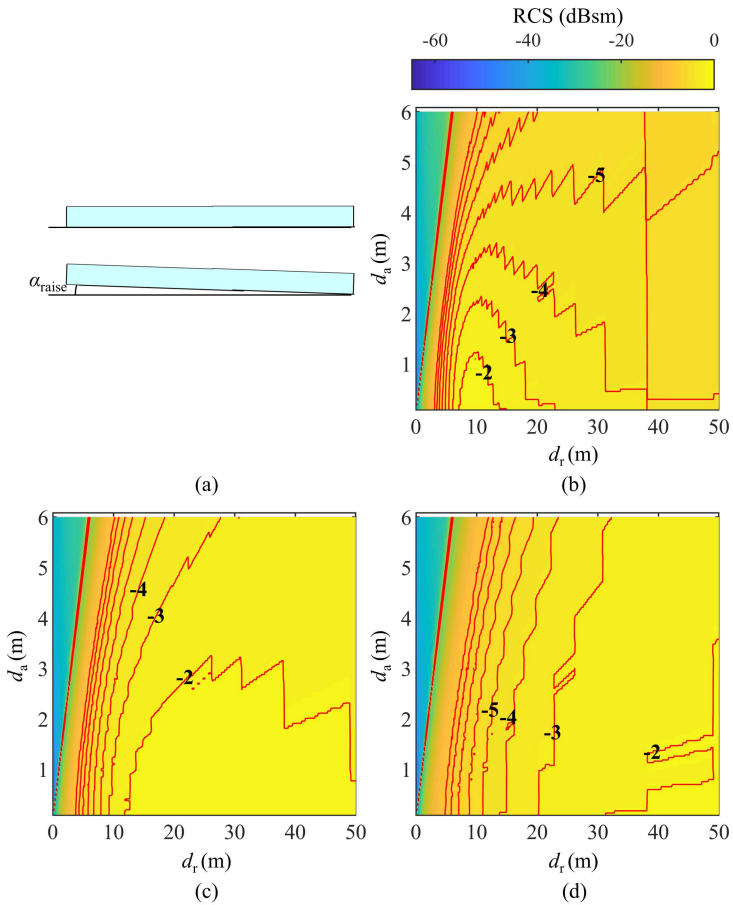


Figure 4.10: (a) Raise the corner side of the reflector with a small angle α_{raise} to prevent water accumulating and its corresponding RCS with α_{raise} equal to (b) 0° , (c) 1° , and (d) 2° .

4.2.6 Other Types

In addition to all the specimens presented in the previous sections, more types are measured. Figure 4.11 shows 6 such types. Figure 4.11 (a) is comprised

of parallel metallic stripes with their width and interval equal to half of the wavelength of the radar signal ($\lambda/2$) in order to create a resonance structure. This however provides very narrow reflection angle range: one reason is that the single stripes behave like cylinders whose reflection depends strongly on the incident angle like the one shown in Figure 3.6; the other reason is that the resonance structure is also incident direction dependent, meaning with changing the incident direction, the interval projection of the stripes on the signal propagation path will change and could be different from $\lambda/2$. Similarly, an improved version of (a) with the stripes integrated both in two orthogonal directions in (b) does not improve the reflection performance obviously.

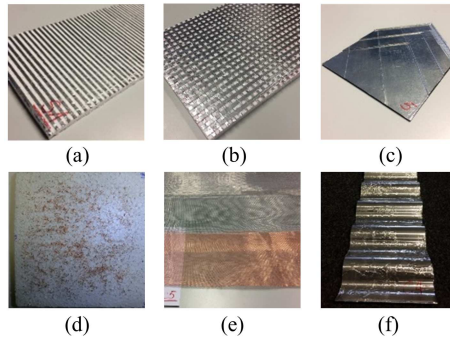


Figure 4.11: Other measured reflector types. (a) Metallic stripes with their width and interval equal to $\lambda/2$. (b) Metallic stripes with their width and interval equal to $\lambda/2$ in both two orthogonal directions. (c) Modified Type 1 with the standing plates divided into multiple steps. (d) Chaff with the length of single metallic wire equal to $\lambda/2$. (e) Metallic mesh. (f) Metallic wave-shaped reflector.

Figure 4.11 (c) divides the standing plate of Type 1 into multiple smaller steps with the length of each step equal to integer times of $\lambda/2$ to create resonance structure. From both measurement and simulation results, with all other conditions unchanged, such reflectors with smaller steps present always smaller reflection magnitude or RCS than the specimen with only one step, i.e. the Type 1 (notice that the corner reflector of Type 1 itself is a resonant structure with the single propagation path difference equal to zero). It also can be found that with more and more steps (thus with the height of the signal smaller steps becoming smaller and smaller), the reflection magnitude also

becomes smaller and smaller. So the Type 1 with only one single step is the best reflector.

Figure 4.11 (d) presents the chaff specimen. Chaffs are very thin, small metallic (sometimes also include other materials like thin glass fiber) wires with their length equal to $\lambda/2$. By deploying them extensively in the air, they are frequently used in electronic radar warfare countermeasures of air combat fighters to create large reflection magnitude without the existence of real objects to mislead or confuse the opponents. Figure 4.11 (e) and (f) are metallic mesh and wave-shaped reflectors. All these specimens provide very small RCS when they are integrated on the road surface compared with Type 1.

4.2.7 Summary

With knowing the reflection magnitude of the specimens and the noise floor with respect to d , their SNR and maximum detection range can be estimated. For example, Figure 4.12 shows that for the specimens in group $\text{GH}(N)$ with $\beta = 0^\circ$, the SNR of the specimens decreases almost linearly (about 2 dB/m) with respect to d and the curves of various specimens are nearly in parallel. The decrease of the SNR stems from the free space loss of the signal, the change of the antenna gain and RCS of the specimens in elevation direction. The specimens with larger H have larger RCS and thus also larger SNR and can be detected in a larger range. However, this increment becomes smaller as H increases. For the specimen G10, the maximum detection range can be up to 40 m. If a larger FFT size is used during the signal processing, a higher detection range can be expected due to the improved SNR obtained from the FFT processing gain. However, this also increases the required processing power of the processing unit. Similarly, the maximum detection range of other specimens with various β are summarized in Table 4.3.

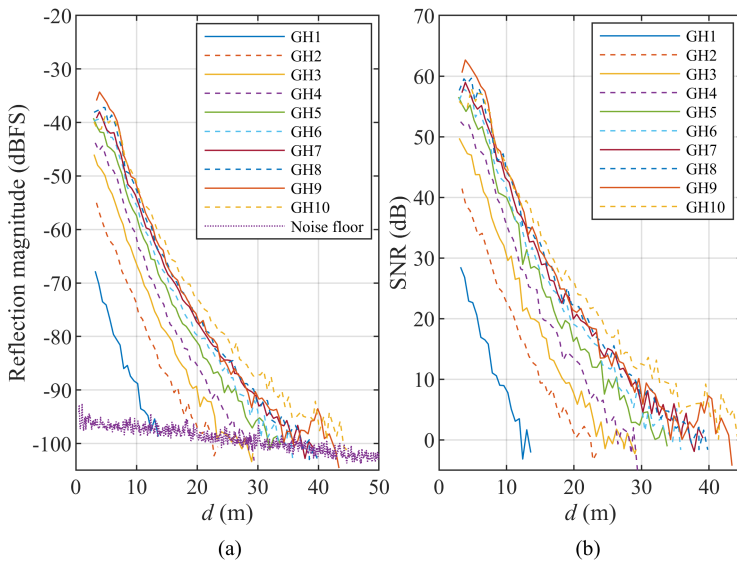


Figure 4.12: (a) Reflection magnitude of $\text{GH}(N)$ with respect to d and the noise floor ($\beta = 0^\circ$). (b) SNR of $\text{GH}(N)$ with respect to d ($\beta = 0^\circ$).

Table 4.3: Maximum detection range (m) of the specimens according to the measurement results.

Type	Sample	β			
		0°	10°	20°	30°
1	GH1	13	11	11	10
	GH5	33	31	29	25
	GH10	42	41	37	34
	GL2	23	24	23	20
	GL6	28	26	24	21
	GL10	29	28	26	22
	GW1	27	27	24	20
	GW4	28	28	24	20
	GW9	30	30	26	22
3	Aluminum spheres	18			
4	$R = 100$ mm	19	21	21	20
	$R = 500$ mm	25	13	13	9
1 with covering	G(N)	29			
	G(N) + 50g Gravel	16			
	G(N) + 100g Gravel	15			
	G(N) + 150g Gravel	15	/		
	G(N) + 20g Water	16			
	G(N) + 30g Water	15			
	G(N) + 54g Water	11			

Table 4.4 summarizes the advantages and disadvantages of the main reflectors discussed in this chapter. Table 4.5 summarizes the main advantages of radar versus camera in road marking and lane detection and indicates the necessity to combine radar and camera data for the function like lane detection. Since the reflectors of Type 1 are the most appropriate specimens among all the reflectors, the reflectors used in the following chapters are all of Type 1 if not otherwise specified.

Table 4.4: Comparison of various reflector types as radar road markings.

Type	Description	Pros	Cons
1	Low-profile asymmetrical trihedral	1) It can provide good RCS in a large azimuth angle range with a small height. 2) The structure is simple to fabricate, which reduces the manufacturing cost.	1) Its profile is low, however, it is still not flat. 2) Its detection gets worse with external coverings like water, etc.
2	Type 1 with slanted standing plates	/	It provides much smaller RCS than Type 1.
3	Metallic balls	1) It provides isotropic reflection in azimuth angle direction. 2) Easy for deployment.	It provides much smaller RCS than Type 1.
4	Type 1 with its standing plates replaced by curved ones	The maximum reflection magnitude at $\beta = 0^\circ$ can be very large with a large R .	1) Its azimuth angle range of reflection depends strongly on R . Dramatic decrease happens with large R . 2) With certain R , its reflection magnitude can be close to that of Type 1, but its fabrication is not as simple as Type 1.

Table 4.5: Advantages of radar versus camera in road marking / lane detection.

Situation	Radar VS. Camera
Fog and haze Sunset / sunrise / glaring sunlight Poor illumination condition including low light conditions and sudden change of the light, e.g. night, headlight from oncoming traffic, at tunnel entrance or exit, etc.	Radar can help camera to determine lane boundary to increase the detection reliability since camera may be shortly blinded.

4.3 Deployment of Dedicated Radar Reflectors on the Road

4.3.1 Single Shot Measurements

A test field as shown in Figure 4.13 is integrated with the reflectors of Type 1 to form a lane containing a right angle turning, a semicircle with an inner radius of 10 m, and two straight lanes with the width of 7 m and 3.5 m, respectively. The photo is taken by a drone and the light yellow dashes are the employed reflectors (radar road markers/markings) with $H = 6$ mm, $L = 0$ mm, and $W = 100$ mm. The reflectors are fabricated according to Figure 4.15 (c) so that they can be placed in all directions. Four separate single shot detection results when the radar is at position 1, 7, 2, and 3 in Figure 4.13 are presented in Figure 4.14. Besides the reflection points of the reflectors, other reflection points come mainly from ground clutter, grass, fence, etc. at the side of the test field, and some of the points also come from the electrical noise or clock interference in the radar hardware itself.

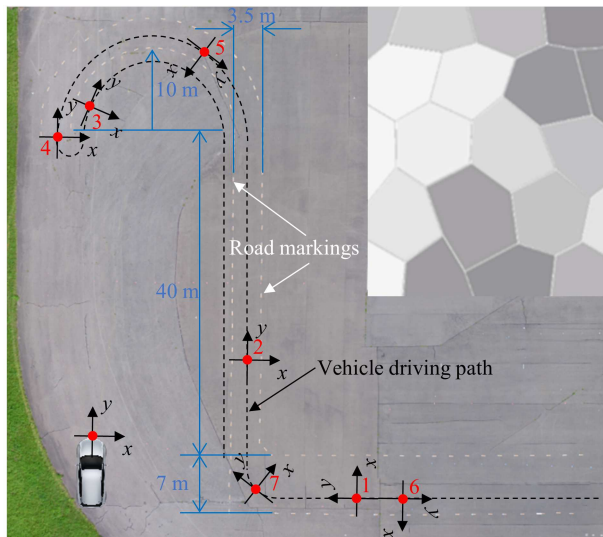


Figure 4.13: Bird view of the test environment taken by a drone.

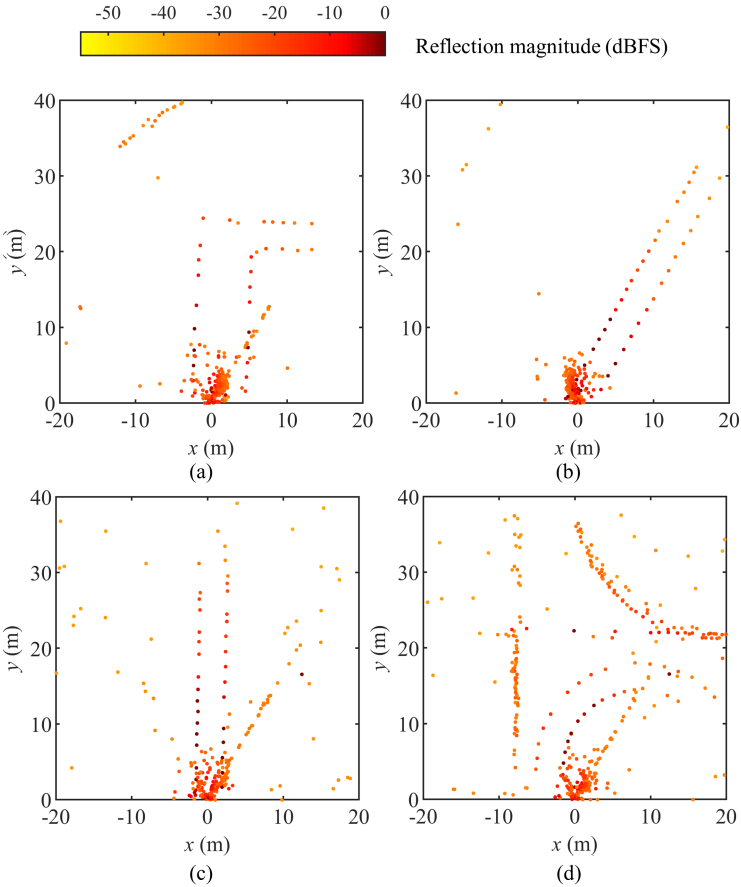


Figure 4.14: Single shot measurement results when the test vehicle is at the position (a) 1, (b) 7, (c) 2, and (d) 3 in Figure 4.13. Test vehicle equipped with radar at its front is at the position of $x = 0$ m and $y = 0$ m.

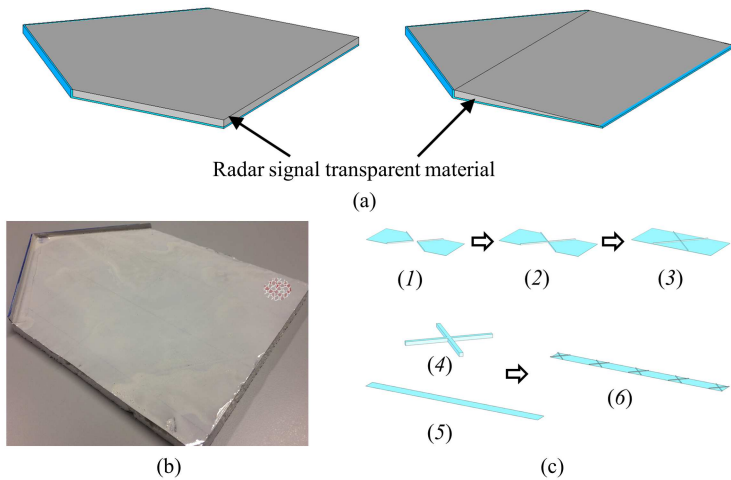


Figure 4.15: A new type of road marking integrated with low profile reflectors for radar detection. (a) Reflectors of Type 1 filled with radar signal transparent material in order to minimize the influence of their height on over-running vehicles by embedding them partly or fully underneath the road surface. (b) Reflectors of Type 1 that are still appropriate for camera detection as normal road marking by painting it with white stripe painting material. (c) Fabrication of the new type of road marking.

4.3.2 Radar Road Signature - a Radar Based Map for Accurate Localization

Figure 4.16 presents two examples of a radar point map by accumulating all the static radar reflection points across all measurement cycles when the test vehicle drives along the trajectory plotted in the black curve. Creating such a map requires the relative movement of the radar during the measurement cycles and this can be accomplished by using a device like ADMA or calculate them through an algorithm like SLAM (Simultaneous Localization and Mapping).

After obtaining the map, it can be stored and used for further accurate vehicle localization after obtaining the rough localization data from GNSS by matching the real time single shot measurement points with the stored map. The way how the points are distributed can be seen as the footprint of the location—a signature of the road. During such a process, the non-static points shall firstly

be filtered out with the help of the detected radial velocity of the points and the velocity of the vehicle itself (v_{EGO}).

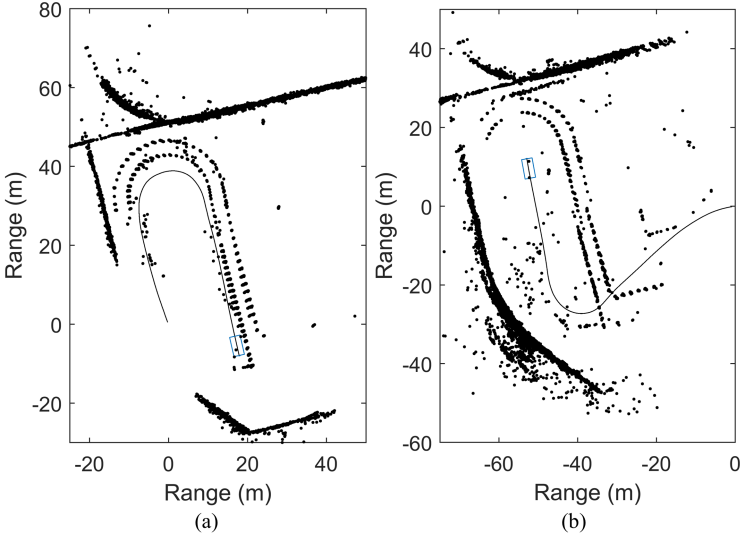


Figure 4.16: Reflection points collected by the radar that can be utilized as radar road signature for accurate vehicle localization. Black curve describes the driving trajectory of the test vehicle.

4.3.3 Roadside Construction Considerations

Although the profile of the reflector is low, to further decrease the influence of its height on the over-running vehicles, the reflector can be partly or totally embedded into the road or underneath the road surface after filling it with low permittivity material like in Figure 4.15 (a). Besides, the reflectors can be still painted with stripe painting materials, in order to make them also appropriate for camera detection, like the one shown in Figure 4.15 (b). According to the measurements, the reflection magnitude of the reflector in Figure 4.15 (b) decreases about 2.5 dB when compared with those without painting. To make the reflectors also detectable from other directions, two such reflectors with opposite orientations can be merged into one reflector like the steps from (1) to

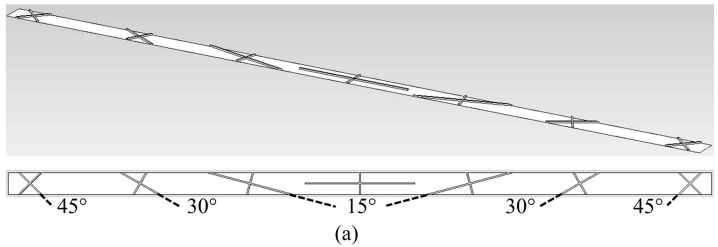
(2) in Figure 4.15 (c), and two additional bottom plates can be added like the steps from (2) to (3) to create other two reflectors. To simplify the fabrication process, a process from step (4) to (6) can be employed where the crossings in step (4), can be either metallic steel or concrete containing high permittivity materials at its surface, are simply integrated onto a substrate in step (5) which also contains high permittivity material. Two specific construction machines can be used to finish such process: the first one paints certain area of the road surface with high permittivity materials; the second one puts and fixes the pre-made crossings onto the painted area finished by the first machine. The pre-made crossings shall be rigid enough, so that they are not deformed by the tires of the vehicles running over them.

In order to make the detection from all directions more robust, the crossings in Figure 4.15 (c) can be rotated one after another with a certain angle. This angle can be determined with the help of the measurement results in Figure 4.6. For example, the crossings in Figure 4.17 (a) has a rotation angle of 15° , leading to a RCS decrease smaller than 3 dB according to Figure 4.6. Figure 4.17 (b) presents the scene where a two-lane road are built with such road markings that can be both detected by radar and camera sensors.

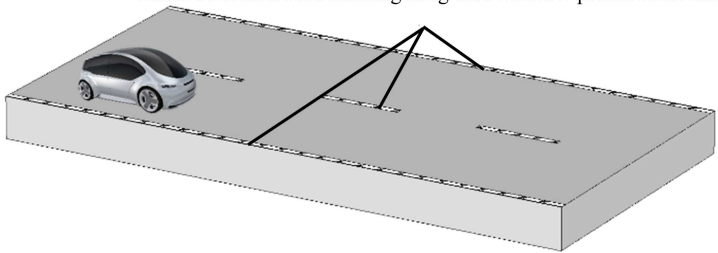
4.3.4 Encoding of Radar Road Markings

As has been mentioned in section 3.6.1, by adjusting the intervals between the reflectors, the driving direction of the vehicle can be determined from the Range–Doppler matrix evaluation. In section 4.3.2, the accurate localization of the vehicle can be accomplished by adjusting the intervals of the reflectors to make them unique within a certain area and matching the single shot detection points with the pre-stored radar reflection map. So the intervals between the reflectors can contain additional information—a smart encoding method to improve the localization accuracy and efficiency with radar.

More generally, not only the intervals between the reflectors, but also the patterns formed by them can be encoded. The encoding can not only be used to locate vehicle, to distinguish between solid and dashed, white and yellow road markings, but can also contain additional road information like the forthcoming of a zebra crossing, sharp and dangerous road curves, the beginning and ending of a tunnel, the maximum allowed driving speed in this area, etc. The



Radar detectable road marking integrated with low profile reflectors



(b)

Figure 4.17: (a) Increase the detection robustness by adjusting the orientations of the integrated reflectors e.g. to rotate them with 15° one after another. (b) Illustration of a two-lane road integrated with the new type of road markings for radar-based lane detection.

corresponding algorithms to decode such constellations shall be able to tolerate the disappearance of certain reflection points belonging to the reflectors and the appearance of certain reflection points not belonging to the reflectors.

4.3.5 Guard Rails and Other Existing Roadside Infrastructure

The above mentioned radar reflectors can be integrated between lanes because of their small height. In contrast, at the sides of the road, existing infrastructure like guard rails, traffic poles, and even curbstone and grass can help the vehicle’s perception system to recognize the boundary of the road with a radar sensor. Figure 4.18 presents two such examples. Different to the reflection points of the grass and curbstone, those from the guard rails are more sparse and regular.

This is because the reflection points of the guard rails come mainly from their standing piles that have a regular distance between each other. A lane detection method with such guard rails and radar road markings employing DL algorithms will be presented more in details in chapter 5.

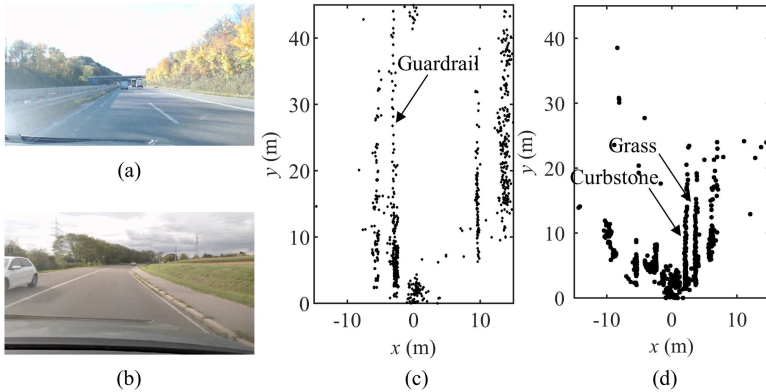


Figure 4.18: Radar reflection points (a) (c) from guard rail, (b) (d) from curbstone and grass. Test vehicle equipped with radar at its front is at the position of $x = 0$ m and $y = 0$ m.

4.4 Summary

Both simulation results in chapters 3 and measurements in chapter 4 indicate that an asymmetrical reflector that has very small height but large azimuth angle range and is also very simple to fabricate, is very appropriate to be used as a radar road maker. By combining several such markers orientating to various directions and integrating them into the current road markings painted with color, lane detection can be accomplished both by radar and camera sensors with higher robustness and reliability when encountering extreme environmental conditions. Despite this, the solution is still not perfect when the reflectors are fully covered by grave, leaves, etc. since such covering makes the detection more difficult. Smart solutions to this problem still need to be investigated in the future. Nevertheless, this chapter presents the opportunity and verifies the feasibility of lane detection with radar sensors.

5 Clustering and Classification of Radar-detectable Roadside Landmarks for Lane Course and Lane Border Determination

In order to determine the lane information after collecting the reflection points, it is necessary to distinguish the reflection points of radar road markers from those of other objects like vehicles, pedestrians, grass, roadside infrastructure, etc. that exist pervasively on the road with corresponding clustering or classification algorithms. This chapter focuses firstly on the non-supervised clustering of the reflection points of the radar road markers based on the on-road measurement data in section 5.1. Then, detection and classification methods with DL—a deep neural network based supervised machine learning technique for lane detection with the help of guard rails and radar road markers will be presented: the radar reflection points are filled into manually created grid maps for grid-based DL in section 5.2 and point-based DL in section 5.3.

5.1 Clustering

The clustering in this section is based on the distance between the reflection points, the spatial arrangement of these points (point pattern), and their reflection magnitudes. A test scene with the radar road markers equidistantly integrated at both sides of a 3 m width straight lane with an interval d_{ps} of about 2 m is set up. All the markers are orientated to the same direction and the test vehicle equipped with radar at its front starts driving orthogonal to the lane direction and then turns right to drive into the lane like the illustration depicted in Figure 5.1.

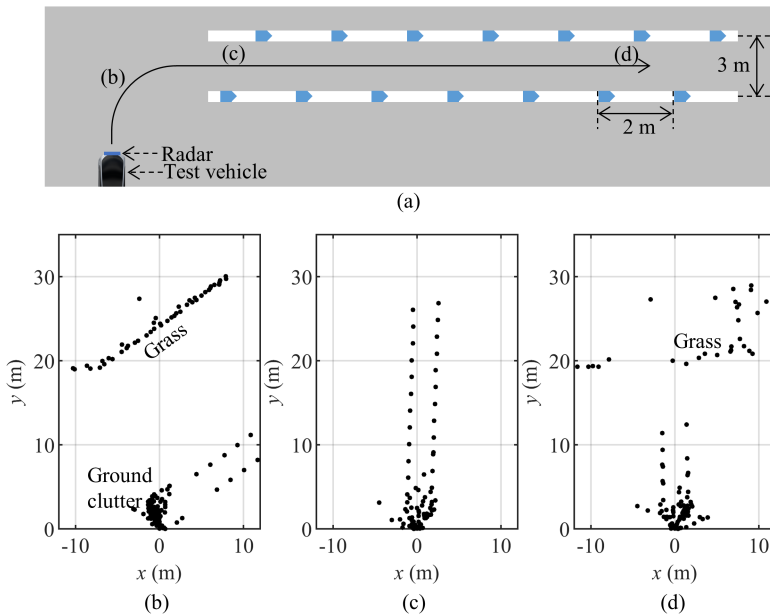


Figure 5.1: (a) Measurement setup for radar road marker clustering. (b) (c) (d) The corresponding radar detection points. Test vehicle equipped with radar at its front is at the position of $x = 0$ m and $y = 0$ m.

5.1.1 Static Point Extraction

The reflection points come from static and moving targets. Since the radar road markers are always static, so first of all, the reflection points of the moving targets shall be excluded.

It has been mentioned previously that the detected velocity v of the object is the relative radial velocity. For static objects, with knowing the velocity v_{EGO} of the test vehicle (or more precisely, the velocity at the position of the radar), the projection of v_{EGO} on the direction of the object shall be equal to v , whereas for moving objects, this equation is not fulfilled.

Besides filtering out the reflection points of the moving objects, part of the points stemming from noise and disturbance can also be filtered out. The v_{EGO}

can be read from the vehicle CAN bus messages, or be calculated from the velocity v_G of the ground clutter reflection points. When the mounting height h of the radar is much smaller than the maximum detection range of the ground clutter, the projection of v_{EGO} on the direction of ground reflection points can be seen equal to v_G : $v_{\text{EGO}} \approx v_G$. Figure 5.2 gives an example with a $v_G = 4.65$ m/s and the ground truth $v_{\text{EGO}} = 4.46$ m/s.

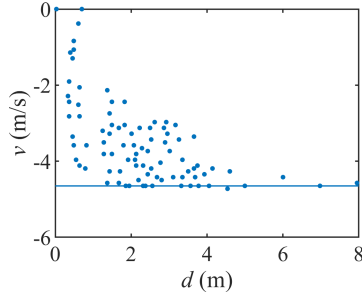


Figure 5.2: Estimation of v_{EGO} from the Range-Doppler matrix of the ground clutter reflection points with $h = 0.15$ m (ground truth: $v_{\text{EGO}} = 4.46$ m/s).

5.1.2 Distance Based Clustering

After excluding the moving points, the distance between the reflection points d_p is calculated. With n denoting the number of static reflection points, $n(n-1)/2$ times of calculation are required to get all the distances. In order to decrease this number, the points within the range of the maximum detection range of ground clutter (5 m in this example according to Figure 5.2) are ignored during the calculation. Since the position of the reflection point is discrete corresponding to the FFT bin location, a distance tolerance d_{pt} of the designed distance d_{ps} is introduced. For description convenience, the process to group all the points according to their intervals is represented by:

$$\text{Clusters} \leftarrow \text{disCluster}(\mathbf{X}, \mathbf{Y}, d_{\text{ps}}, d_{\text{pt}}, n_{\text{min}}) \quad (5.1)$$

where the clusters at the left side of the arrow contain minimum n_{min} points with the length of each edge d_p fulfilling $d_{\text{ps}} - d_{\text{pt}} \leq d_p < d_{\text{ps}} + d_{\text{pt}}$ (an edge is a simple connection between two points) and vectors \mathbf{X} and \mathbf{Y} containing all

x and y values of the input points. The grouped points within the clusters in this step are represented by $\{p_1\}$ and Figure 5.3 (a) presents such results with $d_{ps} = 2$ m, $d_{pt} = 0.2$ m, and $n_{min} = 4$ where three clusters are detected: one cluster from the grass at the boundary of the test field; two clusters from the radar road markers. The edges connecting these clustered points are also drawn in blue color in Figure 5.3 (a) and it can be concluded from the results $\{p_1\}$ that not only the reflection points belonging to road markers are clustered, but also the points of the grass. This is unavoidable when encountering such dense reflection points from vehicles, grass, etc. since the designed distance d_p can easily be found within them.

A method to solve this problem is to exclude the points according to the point density around the points. A simpler way is just to reuse the equation (5.1) with identical \mathbf{X} and \mathbf{Y} , but replacing the input parameters d_{ps} and d_{pt} with d'_{ps} and d'_{pt} according to

$$d'_{ps} = (d_{ps} - d_{pt})/2, d'_{pt} = d'_{ps}. \quad (5.2)$$

With these input parameters, the equation (5.1) returns the points $\{p_2\}$ with their edges fulfilling: $0 \leq d_p < d_{ps} - d_{pt}$ and the corresponding example can be seen in Figure 5.3 (b). It is clear that the dense points in $\{p_1\}$ belong also to $\{p_2\}$, whereas the reflection points of the road markers belong only to $\{p_1\}$. This characteristic can be exploited to get the expected points $\{p\}$ according to

$$\{p\} = \{p_1\} - \{p_1\} \cap \{p_2\} \quad (5.3)$$

and the corresponding result can be seen in Figure 5.3 (c). In process (5.3), $\{p_1\} \cap \{p_2\}$ is used instead of $\{p_2\}$ since not all points in $\{p_2\}$ belong to $\{p_1\}$. This also can be seen in Figure 5.3 (a), (b). If necessary, the points $\{p\}$ can be used again for equation (5.1) to get the final points since certain edges in $\{p_1\}$ could have been deleted in the process of (5.3).

However, the points clustered according to these steps still give many false negatives (the points belonging to the radar road markers are mistakenly not clustered). Consider the scene in Figure 5.3 (d) where a vehicle having dense reflection points (the blue ones in the rectangle) is very close to the radar road markers. Because of this, the three points belonging to the radar road markers are wrongly deleted during the process of (5.3). This is because one

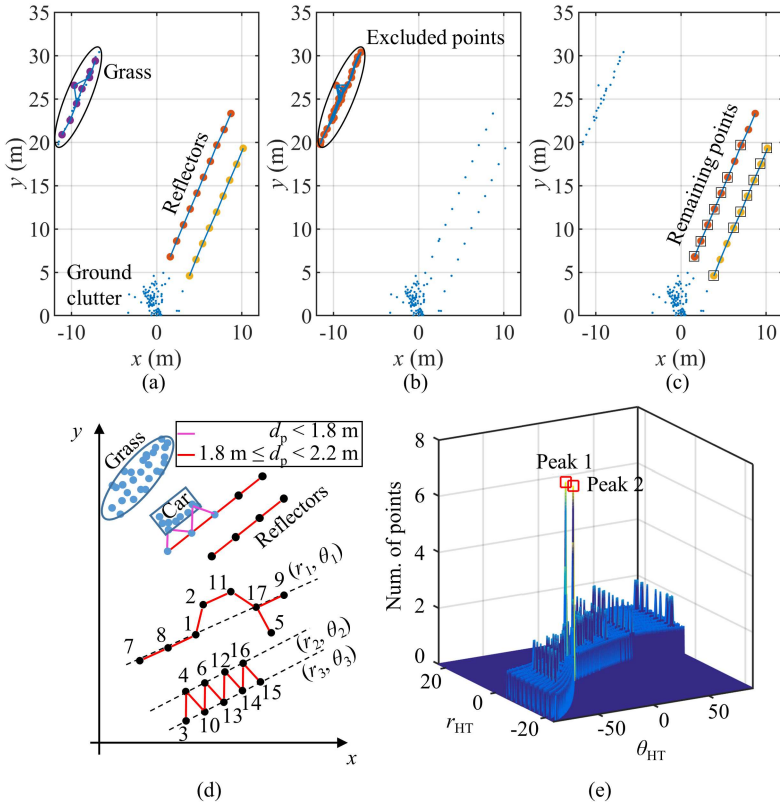


Figure 5.3: Distance based clustering and line extraction. (a) Clustering results $\{p_1\}$ according to the distance between the reflection points. (b) Dense points $\{p_2\}$ that shall be excluded in the clusters in (a). (c) Remaining reflection points $\{p\}$ after excluding points $\{p_2\}$ in (b) from points $\{p_1\}$ in (a). (d) Examples of possible false negatives and false positives. (e) Hough transformation of the points $\{p\}$ in (c). Test vehicle equipped with radar at its front is at the position of $x = 0$ m and $y = 0$ m.

information is still not included during the clustering: the spatial distribution of the points—the point pattern.

5.1.3 Spatial Distribution Characteristic of the Reflection Points - the Point Pattern

As the reflectors in Figure 5.1 are placed in straight lines, their reflection points shall be also in straight lines. A simple way to extract these points is to apply the Hough Transform (HT). In HT, every point in the spatial space will be represented by a curve described by θ_{HT} and r_{HT} in the HT space and every point in HT space can be represented by a curve described by x and y [DH72] in the spatial space. r_{HT} in the HT space is the distance from the origin to the lines going through it in the spatial space and the corresponding θ_{HT} is the angle of the perpendicular vector from the origin to those lines measured clockwise from the positive x axis. For example, the 19 reflection points (red and yellow points) from the radar road markers in Figure 5.3 (c) are converted to 19 curves in HT space in Figure 5.3 (e). The positions where most of the curves intersect in the HT space form peaks and indicate that a line in the spatial space corresponding to this θ_{HT} and r_{HT} has the maximum likelihood. Two peaks in Figure 5.3 (e) can be detected which indicates that two lines exist most likely from the 19 spatial reflection points. The values of the two peaks are both 7, meaning for each line in the spatial space, 7 points are included. These points are marked in black squares in Figure 5.3 (c) and it can be seen that not all 19 points contribute to the HT peaks because not all these 19 points are located in perfect straight lines. This error can stem from the error during the placement of the radar road markers, but can be also from the discrete FFT bins of the detection points. In order to include the remaining points in the spatial space into the peaks in the HT space, the resolution of θ_{HT} and r_{HT} of the HT can be reduced, which will however also include other points not belonging to the road markers. Thus it is always a trade-off that needs to be tuned according to the requirements.

By extracting these lines in the HT space, they can be used to get the points $\{p_2\}$ in equation (5.1) with restricted input points. The restricted points are within the distance r_ε to the extracted line denoted by θ_{HT} and r_{HT} and their positions are represented by \mathbf{X}_ε and \mathbf{Y}_ε instead of \mathbf{X} and \mathbf{Y} . The new $\{p_2\}$ used in the process of (5.3) is then the result of $\text{disCluster}(\mathbf{X}_\varepsilon, \mathbf{Y}_\varepsilon, d'_{ps}, d'_{pt}, n_{\min})$. After this step, the part of the points $\{p\}$ that are within r_ε to the extracted line shall be used again as input points in equation (5.1) to get the final results, otherwise, errors may happen. One such error can be seen in Figure 5.3 (d) where three lines are extracted from HT. For the line (r_3, θ_3) after applying (5.3), the points

4, 6, 12, 16 are excluded from the group. However, the remaining points 3, 10, 13, 14, 15 are not the reflection points from the radar road markers since the intervals between them are not correct. Without applying equation (5.1) again to get the final points, these points will be mistakenly clustered into radar road makers (the reason is that these points are not directly connected, but connected through the points that are excluded in the process of (5.3)). This error can also be found in the line (r_1, θ_1) where the remaining point number after process (5.3) through direct connection is 3 (smaller than the previous setting $n_{\min} = 4$).

Previous discussion focuses mainly on extraction of straight lines, if further kinds of curves need to be extracted, a generalized HT can be employed [Bal81]. For straight lines, only two-dimensional HT of θ_{HT} and r_{HT} (assume two dimensional spatial space) is required. Curves like parabola or clothoids are frequently used to fit the road curves and they require more parameters and consequently higher-dimensional HT space and higher processing requirement. Table 5.1 summarizes the necessary parameters of various curves in HT space (θ_{HT} for parabola in the table describes its orientation).

Table 5.1: Parameters to represent various curves in HT space.

Curve	Parameters	Equation
Line	θ_{HT}, r_{HT}	$x \cos \theta_{HT} + y \sin \theta_{HT} = r_{HT}$
Circle	x_{HT}, y_{HT}, r_{HT}	$(x - x_{HT})^2 + (y - y_{HT})^2 = r_{HT}^2$
Parabola	$x_{HT}, y_{HT}, r_{HT}, \theta_{HT}$	$(y - y_{HT})^2 = 4r_{HT}(x - x_{HT})$

5.1.4 Traverse all Possible Paths

In contrast to HT, this section presents another approach to extract the specified point patterns: to traverse all possible paths in a clustered point group and to evaluate the relation of the angles of the edges (a path is comprised of points and their corresponding edges).

In order to find out all the paths, all 2-combinations of the clustered points from equation (5.1) are listed as the head and tail points of the possible paths. Then, all possible paths from the head point to the tail point will be traversed. At last, the angles of the edges of all these paths will be evaluated according to

pre-defined constraints. Such a process can be seen in the example in Figure 5.4 (a) where 9 points are clustered into 2 groups. For the first group with point 1 to 5, there are 10 possible 2-combinations. If point 1 is the head point and point 3 is the tail point, then there are 3 possible paths:

- point 1 → point 2 → point 3
- point 1 → point 2 → point 5 → point 3
- point 1 → point 2 → point 4 → point 5 → point 3

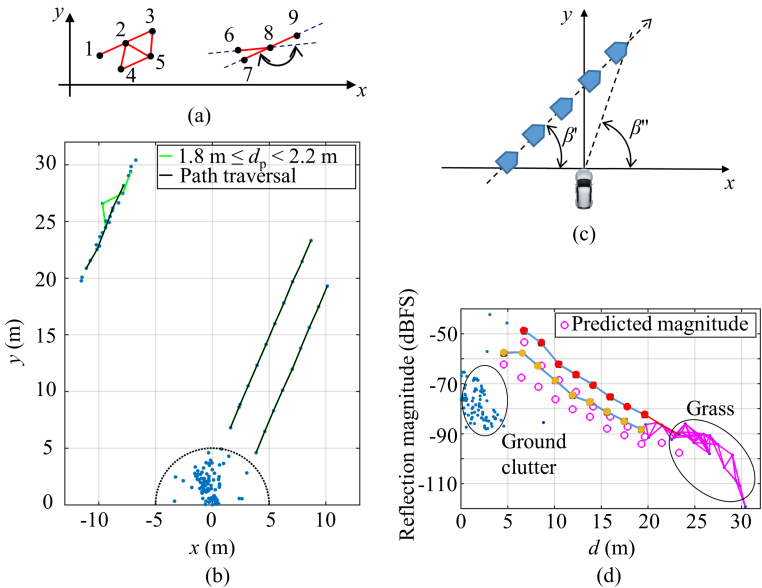


Figure 5.4: (a) Illustration of the path traversal process. (b) Clustering results with the path traversal method (angle variation: smaller than 10° ; minimum point number n_{\min} in one cluster: 5). (c) Reflection magnitude estimation with knowing the orientation of the road markers. (d) Estimated and measured reflection magnitudes of the road markers in Figure 5.3 (c).

Cycles in the path that lead to infinite loop of the path traversal algorithm shall be avoided by constraining each point in every path only be able to be traversed once. For instance, path: point 1 → point 2 → point 5 → point 4 → point 2

→ point 3 is not allowed since point 2 appears twice in this path. After getting all the possible paths, the angles or slopes of the edges connecting the points are calculated and evaluated. It is worth noting that the direction of each path shall be defined at first in order to evaluate the angle differences between the edges. Refer to the second clustered group in Figure 5.4 (a) of point 6 to 9, the angle difference between the edges from point 6 to 8 and 8 to 7 is ϕ , whereas that between from point 6 to 8 and 8 to 9 is $180^\circ - \phi$. If no direction is defined, the angle difference between their edges of the two paths from point 6 to 9 and 6 to 7 could both be ϕ , which will lead to wrong clustering results. Figure 5.4 (b) presents such a clustering result with the path traversal algorithm of the same reflection points as in Figure 5.3 (a) where green connections present all possible edges based on the distance and black connections indicate the 3 clustered groups with their edges fulfilling the following constraints:

- angle difference between all edges in a path shall be smaller than 10° ;
- minimum point number in a path is 5.

These constraints can be adjusted accordingly in order to detect point patterns like circles, parabolas, etc.

5.1.5 Utilize Reflection Magnitude to Increase the Clustering Reliability

The reflection magnitude of the road marker or its RCS is incident angle dependent, so without knowing the incident angle, it is not possible to estimate its reflection magnitude. However, after determining the point pattern of the reflection points with HT or with the path traversal algorithm, the orientation of every road maker can be determined. Together with its position, the incident angle to the marker can be calculated, and together with the antenna gain, its reflection magnitude can be determined, like the one shown in Figure 5.4 (c). Figure 5.4 (d) presents such estimated reflection magnitude of the reflection points in magenta circles and the real measured reflection magnitude of the points in Figure 5.3 (a) in red and yellow points. The reflection magnitude difference between the estimation and measurement can be used as a criterion to determine whether these points come from the radar road markers or not. It is worth noting that the relative reflection magnitude between the points in the

clustered group is preferred to be used since all the reflectors in an area can simultaneously be affected by the same factors like water coverage, resulting in a similar reflection magnitude change of all these radar markers in this area. In the results of Figure 5.4 (c), all the estimated magnitudes have 5 dB to 10 dB decrease when compared to the measured magnitudes (and the slope of the magnitude with respect to d of the estimation and measurement are similar), so they are very likely from the reflection points of the radar road markers.

5.1.6 Summary

The above mentioned algorithm clusters the reflection points of the radar road markers without utilizing training data or labelling data, which is an advantage of this method. Tracking technology can be employed to decrease the processing power requirement and to increase the detection accuracy. This method can handle simple scenarios whereas for more complicated scenarios, supervised clustering and classification can be utilized. The following two sections will focus on this topic.

5.2 Pixel-wise Lane Segmentation with Neural Networks

From 1943 in which year Walter Pitts and Warren McCulloch created a computer model—the neural networks to mimic the working process of a biological brain, DL has evolved significantly over the time. The dramatic improvement in computational performance, especially the introduction of Graphics Processing Unit (GPU) in 1999 has further promoted the evolution of DL. In recent years, the humongous amount of data that can be acquired through various sensors also have boosted the development of DL. For perception tasks of autonomous vehicles (but not only), DL plays a more and more important role. However, most DL for perception tasks nowadays are designed for and applied to camera sensors. In the following sections, the application of DL to radar data for perception purposes, especially for lane segmentation, will be presented.

This section is organized as follows: firstly, the basic concept of DL and its software calculation platforms are introduced. Then, two frequently used

pixel-wise semantic segmentation NN architectures and the input data structure of radar reflection points are presented, followed by the introduction of the evaluation metrics and training parameter setup. After that, lane detection with guard rails on the high way and radar road markings on the test field are discussed.

5.2.1 Basics of Deep Learning - Steps Towards Semantic Segmentation

DL is a branch of machine learning whose models are mostly based on an artificial neural network (ANN). An ANN is a neural network (NN) constructed to imitate the way how the neurons in a biological brain work, however in a much simpler way: in a biological brain, the neurons can be connected in any way as long as they are close to each other; conversely in ANN, the artificial neurons are arranged in different discrete layers, and their connections and the data propagation graph are also predefined. Figure 5.5 shows a simple multilayer perceptron (MLP) ANN used for handwriting recognition with one-hot output encoding. Before the NN can be used for prediction, the training process needs to be completed.

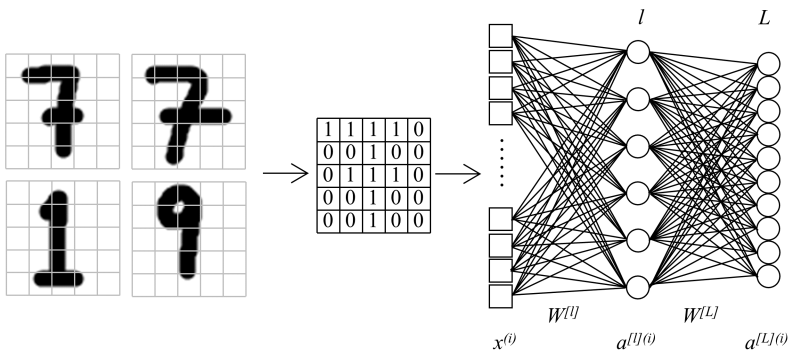


Figure 5.5: Classic DL problem: handwriting digit recognition.

In Figure 5.5, every input image is represented by $5 \times 5 = 25$ pixels. If only the occupancy of the pixel by the digit is considered (1 if the pixel is occupied by the digit, 0 otherwise; other features like grayscale or RGB (Red, Green, Blue)

values can also be used to form the input vector) as the NN input format, the pixels in every image can then be flattened into a vector $x^{(i)}$:

$$\begin{bmatrix} x_1^{(i)} & x_2^{(i)} & \cdots & x_{n^{[l]-1}}^{(i)} & x_{n^{[l]}}^{(i)} \end{bmatrix}^T, \quad (5.4)$$

where $n^{[l]}$ is the number of features in the layer l ($n = 25$ for Figure 5.5, $l = 0$ for input layer). $x^{(i)}$ is then mathematically manipulated by a weight matrix $W^{[l]}$ and a bias vector $b^{[l]}$:

$$W^{[l]} = \begin{bmatrix} w_{1,1}^{[l]} & w_{1,2}^{[l]} & \cdots & w_{1,n^{[l]-1}}^{[l]} \\ w_{2,1}^{[l]} & w_{2,2}^{[l]} & \cdots & w_{2,n^{[l]-1}}^{[l]} \\ \vdots & \vdots & \ddots & \vdots \\ w_{n^{[l]},1}^{[l]} & w_{n^{[l]},2}^{[l]} & \cdots & w_{n^{[l]},n^{[l]-1}}^{[l]} \end{bmatrix}, b^{[l]} = \begin{bmatrix} b_1^{[l]} \\ b_2^{[l]} \\ \vdots \\ b_{n^{[l]}}^{[l]} \end{bmatrix} \quad (5.5)$$

to get the neurons' activation $a^{[l]}$ according to:

$$a^{(i)[l]} = g(z^{[l]}) = g(W^{[l]}a^{(i)[l-1]} + b^{[l]}), (a^{(i)[0]} = x^{(i)} \text{ for } l = 1) \quad (5.6)$$

where $g(\cdot)$ is called the nonlinear activation function which enables the network to solve nonlinear problems. This is a recursion process called forward propagation and for the last layer of the NN, $n^{[l]}$ is the number of the classes to be predicted, $a^{(i)[l]}$ is the hypothesis of the i^{th} input data $x^{(i)}$ and is represented by $\hat{y}^{(i)}$ with the ground truth output represented by $y^{(i)}$.

With both the ground truth output $y^{(i)}$ and the corresponding hypothesis output $\hat{y}^{(i)}$, a loss function $L(y^{(i)}, \hat{y}^{(i)})$ is utilized to indicate their discrepancy. This is only for a single input $x^{(i)}$. In order to characterize the discrepancy for all m training data, an averaged loss function across all these samples—the cost function $J(W, b)$ is used:

$$J(W, b) = \frac{1}{m} \sum_{i=1}^m L(y^{(i)}, \hat{y}^{(i)}), W = \{W^{[l]} | 1 \leq l \leq L\}, b = \{b^{[l]} | 1 \leq l \leq L\} \quad (5.7)$$

As an example of the cost function, if a soft-matrix layer is employed in the last layer, then the output hypothesis is normalized in the range [0 1],

a cross-entropy loss function then can be used to indicate the discrepancy of hypothesis from the ground truth labelling, and the corresponding cost function is expressed as follows:

$$J_0(W, b) = -\frac{1}{m} \sum_{i=1}^m \sum_{k=1}^K (y_k^{(i)} \log \hat{y}_k^{(i)} + (1 - y_k^{(i)}) \log(1 - \hat{y}_k^{(i)})). \quad (5.8)$$

where the subscript k represents the k^{th} output of K classes ($K = n^{[l]}$). For the illustration in Figure 5.5, K equals to 10.

Observing the above equation, it can be found that if the discrepancy between labelling $y_k^{(i)}$ and hypothesis $\hat{y}_k^{(i)}$ gets larger, the loss will increase dramatically, indicating that the loss or cost function will penalize the wrong prediction: when the labelling $y_k^{(i)}$ is 1, if the hypothesis $\hat{y}_k^{(i)}$ is also 1 which means a correct prediction, then the loss will be 0; conversely, if the hypothesis is 0 which means a totally wrong prediction, then the loss will be infinitely large; when the labelling $y_k^{(i)}$ is 0, if the hypothesis $\hat{y}_k^{(i)}$ is also 0 which means a correct prediction, then the loss will be 0, conversely, if the hypothesis is 1 which means a totally wrong prediction, then the loss will be infinitely large. This property is also illustrated in Figure 5.6. Theoretically, the loss or cost can be zero, which is however hardly reachable in practice.

Sometimes, the trained model works well for the training dataset, but not for the testing dataset which is not used for training. This problem is called overfitting in DL. The solutions to such problem are to include more training data, utilize dropout layers, add an additional regularization item in the cost function, etc. In equation (5.9), a Frobenius Norm item is added in the cost function to address this problem where λ is the regularization parameter in the range of [0 1]. This parameter is a manually tuned parameter and when it is set close to 1, the overfitting problem can be addressed whereas the contrary of overfitting—the underfitting problem may arise instead. In contrast, if this parameter is set to be close to 0, then the overfitting problem may arise. So an appropriate selection of λ is very essential.

$$J(W, b) = J_0(W, b) + \frac{\lambda}{2m} \sum_{l=1}^L \sum_{i=1}^{n^{[l-1]}} \sum_{j=1}^{n^{[l]}} (w_{j,i}^{[l]})^2. \quad (5.9)$$

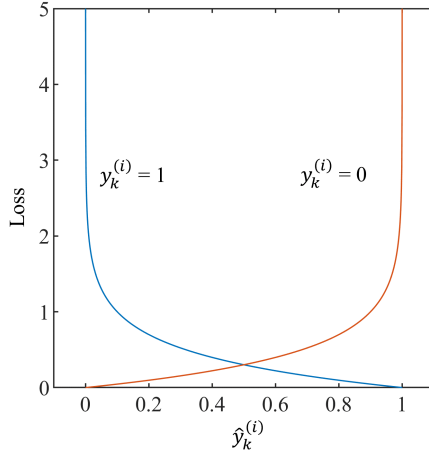


Figure 5.6: Loss function: penalize discrepancy between labelling (ground truth) and hypothesis.

As been mentioned above, the cost function describes the discrepancy between labelling and prediction. So the task of the training process is to minimize the cost function $J(W, b)$ by tuning W and b . Backpropagation is a frequently used method to achieve $\min_{W, b} J(W, b)$ by calculating the gradient of $J(W, b)$ with respect to W and b : $\frac{\partial J(W, b)}{\partial W}$ and $\frac{\partial J(W, b)}{\partial b}$. Then the trained parameters can be updated as follows:

$$\begin{aligned} \text{repeat } \{ & W := W - \kappa \frac{\partial J(W, b)}{\partial W} \\ & b := b - \kappa \frac{\partial J(W, b)}{\partial b} \} \end{aligned} \tag{5.10}$$

where κ represents the learning rate.

After the training is finished, i.e., the values of W and b are updated so that the cost $J(W, b)$ reaches a minimum value, the trained parameters can be used for predicting the hypothesis of the untrained data. The above process is the basic concept of training a DL network and in practice, more techniques like Dropout Regularization, Data Augmentation, Input Normalization, Batch Normalization, Mini Batch, Gradient Descent with Momentum, Adaptive Mo-

ment Estimation (ADAM) Optimization, and Learning Rate Decay, etc. are frequently employed.

Since the basic model mentioned above flattens the input images into vectors, the spatial information of the images are not fully exploited. In order to address this problem, a special structure of MLP—the CNNs is developed and Figure 5.7 (a) illustrates such a simple CNN. Different to MLP where the flattened input vector is multiplied by $W^{[l]}$, in CNN, the input matrix (or pixels for images) does not need to be flattened so that the spatial information can be retained. Instead of $W^{[l]}$ in MLP, matrices called kernels (sometimes also named filters or feature detectors) are used in CNN to get the convolutions of each patch of the input matrices. These kernels are moved all around the input matrix to get the output so that they can be seen as the weights shared by all the patches of the input matrix. These convolutional values are then fed into activation functions to enable non-linear computations which is similar to that of MLP. Several parameters of the convolution are frequently used: kernel size; stride that defines the movement step size of the kernel; padding that defines the extension of the border of the input matrix; dilation rate that defines the spacing between the values in a kernel in order to widen the field of view at the same computational cost. Figure 5.7 (b) gives two examples with dilation rate equal to 0 and 1. The last layers of CNN are usually also MLPs after the output of the convolutional layers are flattened. In practice, in order to improve the prediction robustness, several pooling layers will be added between the convolutional layers.

The training of a CNN calculates the values of the kernels that minimize the cost J and the learned values describe the features in the input matrix that are learned during training. So the kernels are also named feature maps. The feature learning process is a recursive process, indicating those features learned by the latter layers are based on the features learned by the previous layers, so the front layers learn low-features and the latter layers learn high-features based on those low-features.

With this NN, the class of the input can be predicted. Researchers in [BKC17], [SLD16] make a step forward. With the images as the input, they have achieved pixel-level understanding—the semantic segmentation with a CNN-based NN. Figure 5.8 (a) shows a segmentation example with a photo taken on the highway as the input and the trained model [BKC17] for prediction. This architecture can be thought as a structure containing two sub-networks, one to convert

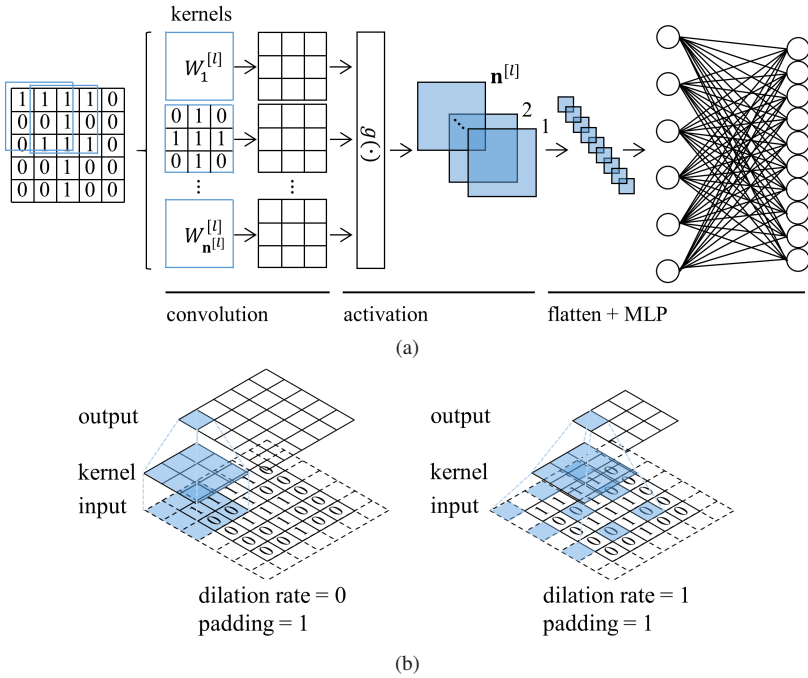


Figure 5.7: (a) Architecture of a CNN and (b) its convolution process.

the input matrix into predictions and the other one to convert the pixel-wise segmentations into the same predictions as from the first half of the network. This process is illustrated in Figure 5.8 (b) where the predictions from both sides meet at the middle of the image. So typically, such segmentation architecture is symmetric (the weights however need to be learned individually). In this chapter, such idea for image semantic segmentation with images recorded with camera sensors will be applied for radar data-based semantic segmentation, especially for lane segmentation.

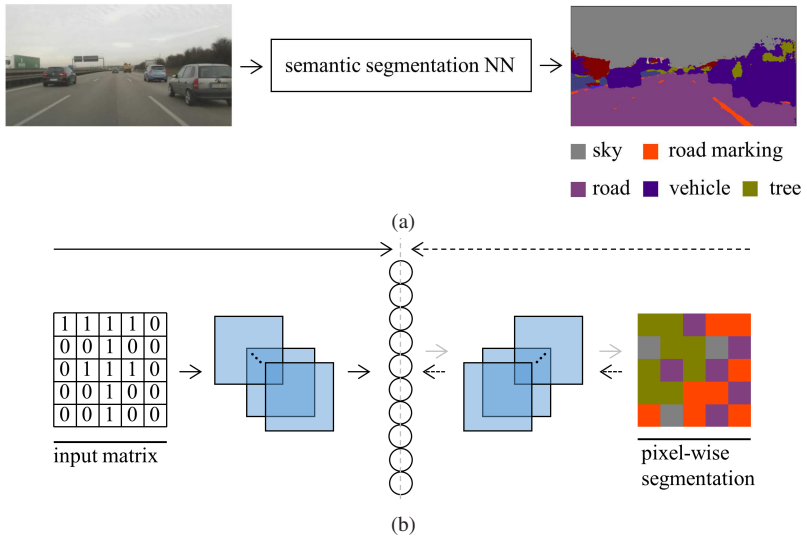


Figure 5.8: (a) Pixel-level image semantic segmentation [BKC17]. (b) Principle of pixel-wise semantic segmentation NN.

5.2.2 Deep Learning Framework

It has been mentioned above that training a NN model is simply to find the optimal weights and biases of this model so that the total cost of all the training data reaches a minimum value. With the help of CPUs, GPUs, TPUs, etc., this calculation process can be significantly accelerated. A graph representing the architecture of the NN, together with training specifications can be created in some platforms to accomplish the computation task. TensorFlow developed by Google Brain Team, Keras, PyTorch, Caffe, Theano, etc. are frequently used DL frameworks. All the results in this dissertation are realized with TensorFlow.

5.2.3 Grid Segmentation Neural Network Architecture

FCN semantic segmentation [SLD16] and SegNet [BKC17] are the first encoder–decoder architectures for image semantic segmentation where the encoder

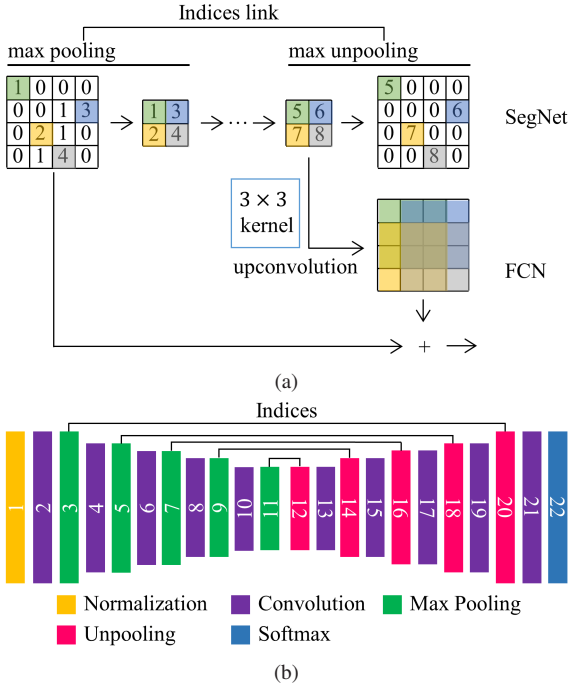


Figure 5.9: (a) Comparison between decoder architectures in SegNet [BKC17] and FCN semantic segmentation [SLD16]. (b) Architecture of a 5-Layer SegNet [BKC17].

converts the input image into feature map vectors and the decoder converts the semantic segmentation back to the input image dimension. The part of the decoder is where various NNs of segmentation differ, for example, in Figure 5.9 (a), two distinct decoders of SegNet and FCN are presented. For the decoder in SegNet, upsampling is performed with max unpooling and the indices link that connects the corresponding encoder layer that indicates the position of the value to be set during upsampling. In the following section, the SegNet is used for the semantic segmentation with the radar data.

Figure 5.9 (b) shows the architecture of a 5-layer SegNet used in this chapter with its parameters described in Table 5.2 where the receptive field describes the region in the input space that is converted into a feature value in correspon-

ding layers. For each convolution layer with batch normalization: stride = 1 and padding = SAME; for each max un-/pooling layer: stride = 2 and padding = SAME; dilation = 1 is for the whole network. Sublayers 1 to 11 belong to the encoder network and the remaining ones belong to the decoder network.

Table 5.2: Configuration of SegNet and its corresponding receptive field.

Layer	1		2		3	
Sublayer	2	3	4	5	6	7
Kernel size	(7,7,64)	(2,2)	(7,7,64)	(2,2)	(7,7,64)	(2,2)
Receptive field	7×7	8×8	20×20	22×22	46×46	50×50
Layer	4		5			
Sublayer	8	9	10	11		
Kernel size	(7,7,64)	(2,2)	(7,7,64)	(2,2)		
Receptive field	98×98	106×106	202×202	218×218		

5.2.4 Input Dataset Preparation

Unlike the pixels in images captured by video sensors, the data collected by radar sensors after CFAR process are discrete reflection points. Figure 5.10 illustrates two different methods to feed such detection points into the NN:

- FFT grid: as has been mentioned in previous chapters, the position of the radar reflection points is determined by target range r and its corresponding azimuth angle β , both of which are equally spaced values. So all possible detection points will fit into a fan-shaped grid map like the one shown in Figure 5.10 in orange color;
- Custom grid: unlike the fan-shaped FFT grid cells, square-shaped grid cells of identical size are manually created, and the reflection points are filled into these cells afterwards, like the one shown in Figure 5.10 in grey color.

In Figure 5.10, two identical grey squares are created to illustrate the possible objects in two distinct ranges and the blue points around them are to represent their possible detection points. If the FFT grid is employed, then the reflection

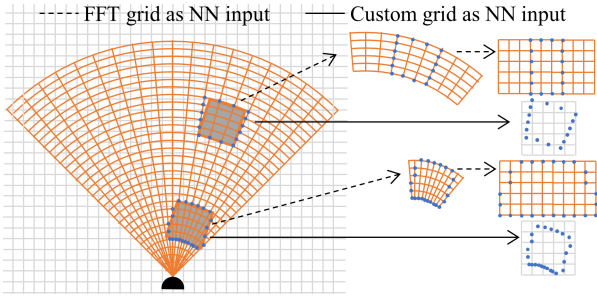


Figure 5.10: Input data for NN.

points of these two objects will form two totally different shapes like shown in Figure 5.10 and this shape deformation is caused by the “deformed” fan shape itself. For the second variant—the custom square, this shape deformation does not exist.

So although both input formats are possible to be used as NN input, the latter one is simpler and thus preferred in this dissertation. Because of the point density variation with respect to range, the reflection points of the same object at all various ranges shall be included in the training dataset.

In the following implementations, several input features are considered:

- Single channel input with binary digit: as the simplest way, when a square grid is filled with at least one reflection point, then this cell is represented with digit 1. When the cell is empty otherwise, it is represented with digit 0. In the following description, the 5-layer NN in Figure 5.9 (b) is represented by model *B5*. Structures with 4 and 3 layers are represented by model *B4* and *B3*, respectively.
- Single channel input with maximum normalized reflection amplitude: instead of binary digits, the cells can store the amplitude value of the reflection points. However, the reflection amplitude of the same object can be different with a different parameter setup of the radar or with different radars. So the RCS or the normalized amplitude of the points are preferred. In this work, the normalized reflection amplitude will be employed and it is calculated as follows: the ground clutter reflection

points are firstly be selected and sorted according to their amplitudes, then the ones with their amplitudes between 20% and 80% among the sorted points are averaged. At last, all the reflection points are normalized with respect to this averaged amplitude value. If several points are located in the same cell, the one with the maximum magnitude will be selected. Such input with 5-layer and 4-layer (with the last layer in encoder and first layer in decoder layer of Figure 5.9 (b) deleted) structures are represented by model *A4* and *A5*, respectively.

- Two-channel input with point number and maximum normalized reflection magnitude: different from single input channels, in this model, two channels are considered. In the first channel, the number of points in every cell is calculated (similar to point density) as the input feature. In the second channel, the maximum normalized reflection magnitude is calculated. Such input with 5-layer structure is represented by model *C2*.
- Four-channel input: the first two channels are identical to those of model *C2*, the last two channels contain additionally the range and angle of the cells. Such input with 5-layer structure is abbreviated with model *C4*.

The radial velocity feature of the reflection points can be used to differentiate moving objects from static objects. In order to prove the ability of the NN to distinguish objects like guard rails, trees and bushes at road side, vehicles in traffic jam also without any velocity information, the feature velocity is not used.

5.2.5 Evaluation Metrics

In order to evaluate the performance of the prediction results, several parameters are used:

- True positive (TP): an actual positive value is correctly predicted as positive.
- False positive (FP): an actual negative value is wrongly predicted as positive.

- True negative (TN): an actual negative value is correctly predicted as negative.
- False negative (FN): an actual positive value is wrongly predicted as negative.
- Accuracy: among all the predictions, the percentage of correct predictions, calculated by: $\frac{TP+TN}{TP+TN+FP+FN}$.
- Precision: the fraction of positive predictions that is correct, calculated by: $\frac{TP}{TP+FP}$.
- Recall: the fraction of actual positive values that is correctly predicted, calculate by: $\frac{TP}{TP+FN}$.
- F1 score: a value considering both precision and recall, calculated by: $\frac{2}{F1\ score} = \frac{1}{Precision} + \frac{1}{Recall}$.
- Intersection over union (IoU): area of overlap over area of union, calculated by: $\frac{TP}{TP+FP+FN}$.

In summary, these definitions are also visualized in Figure 5.11.

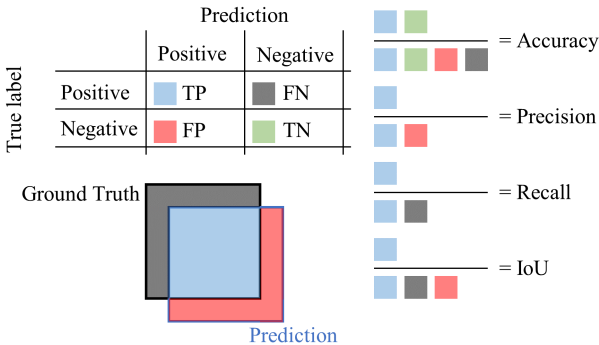


Figure 5.11: Evaluation metrics.

5.2.6 Training Parameters

- Objective loss function: cross entropy loss function.
- Optimization algorithm: ADAM with initial learning rate equal to 0.001, exponential decay rate for the 1st and 2nd moment estimation equal to 0.9 and 0.999 respectively [KB15].
- Dataset distribution: 64% for training, 16% for validation, 20% for testing.
- Activation function: Rectified Linear Unit (ReLU) for encoder network, no activation function for decoder network.
- Input normalization: Local response normalization with depth radius equal to 5, bias equal to 1, alpha and beta equal to 0.0001 and 0.75 respectively [KSH12].
- Intermediate layer normalization: Batch normalization [IC15].

5.2.7 Guard Rail Based Lane Segmentation on the Highway

Output Dataset Preparation - Labelling

In order to calculate the NN parameters W and b , ground truth values $y^{(i)}$ are required which are created through labelling. To detect the lane by the guard rails at the two sides of a highway, 6673 measurement cycles with 300×450 grid cells covering $40 \text{ m} \times 60 \text{ m}$ ($13.3 \text{ cm} \times 13.3 \text{ cm}$ for one single grid cell) in each cycle are labelled. Figure 5.12 shows two measurements and their corresponding labelling examples. Besides the driving lane (purple, class 1), the vehicles on the lane are also labelled (red, class 2) to indicate that the area is not drivable regardless of the lane. The rectangles hitting all the points belonging to one vehicle are labelled to represent the vehicles. All remaining regions are labelled as undefined (class 0). In Figure 5.12, vehicle A is not labelled as a vehicle since there exist no guard rail at its right side; in other words, in this labelling, a lane with guard rails at both sides is the prerequisite for the vehicle. The statistics of the labelling are as follows: class 0 (785,168,388

grids, 87.2%); class 1 (112,777,272 grids, 12.5%); class 2 (2,909,340 grids, 0.3%).

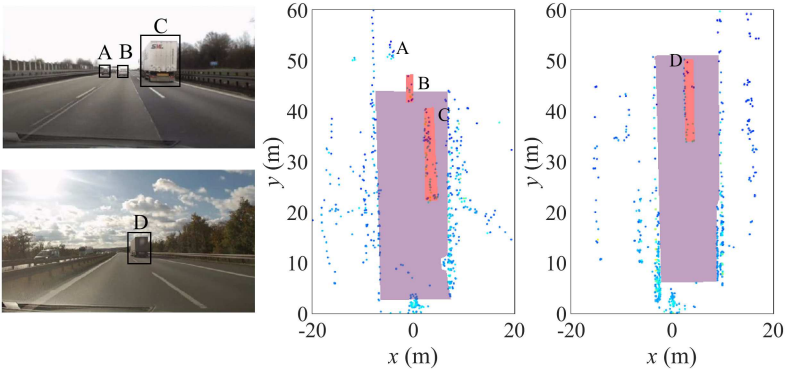


Figure 5.12: Labelling of the driving lane on a high way between guard rails (purple, class 1) and relevant vehicles (red, class 2). Test vehicle equipped with radar at its front is at the position of $x = 0$ m and $y = 0$ m.

Training Metrics and Predictions

Figure 5.13 presents the training metrics of the validation dataset up to Epoch 65. An Epoch consists of one full training of all the training data, meaning equation (5.10) is updated 65 times during training (actually, the training data is divided into several sub-datasets, called mini-Batches in order to decrease the memory requirements and to accelerate the training process).

Figure 5.14 (a) shows the prediction results with trained model *B5*. It can be found that although vehicle *A* is not labelled as vehicle in Figure 5.12, it is recognized partly as a vehicle, which reduces the precision score of class 2 in Figure 5.13. So in another variant, all the vehicles are labelled regardless of the presence of the guard rails (e.g. vehicle *A* in Figure 5.12 is also labelled as a vehicle) and its corresponding prediction result of Figure 5.14 (a) is shown in Figure 5.14 (b). The corresponding training metrics are also plotted in Figure 5.13 with the model name *B5-AllVeh*. All the testing metrics can be found in Table 5.3 where the precision of class 2 improves from 0.46 with model *B5* to 0.61 with model *B5-AllVeh*.

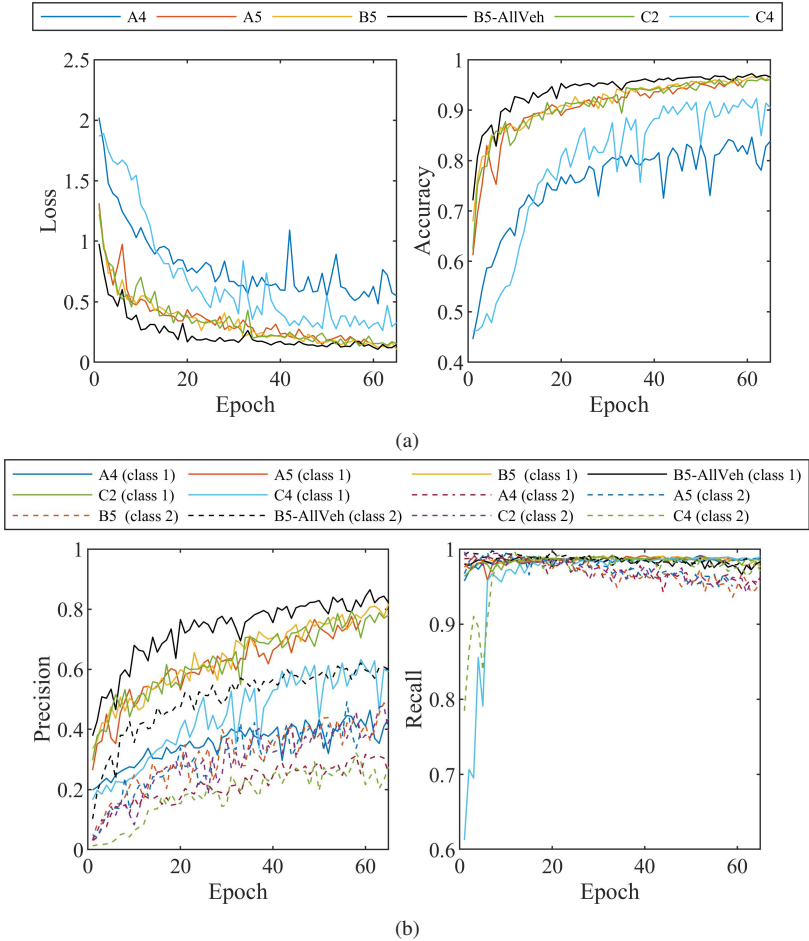


Figure 5.13: Validation metrics during training. (a) Loss and accuracy of the validation dataset up to training Epoch 65. (b) Precision and recall of the validation data set up to training Epoch 65.

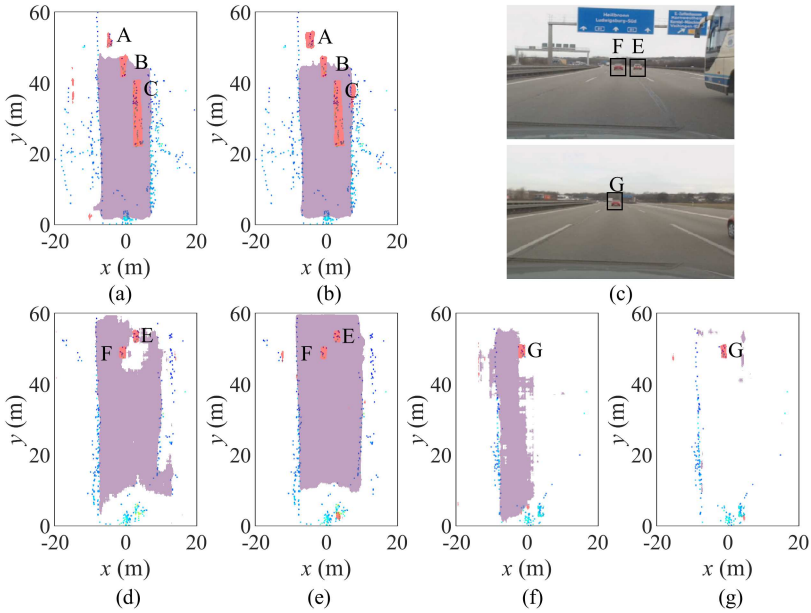


Figure 5.14: (a) (b) Segmentation results of Figure 5.12 with model *B5* and model *B5-AllVeh* at Epoch 65. (d) (e) Segmentation results of model *A4* and model *A5* with the lane width equal to about 20 m. (f) (g) Segmentation results of model *A4* and model *A5* with no guard rail existing at the right side (no defined lane). (c) The corresponding measurement scene of (d), (e), (f), (g) recorded with a camera mounted in the test vehicle. Test vehicle equipped with radar at its front is at the position of $x = 0$ m and $y = 0$ m.

From the training metrics, it can be concluded that the results of model *B5*, *A5*, *C2* present nearly no difference, indicating the amplitudes of the reflection points do not contribute to the prediction performance. In contrast, those of model *A4* and *C4* are much worse. Table 5.2 shows that the receptive field of model *A4* used in this section is 106×106 and for certain datasets, the space between the guard rails at two sides of the road can be up to about 20 m (150 grid cells with $13.3 \text{ cm} / \text{grid cell}$) like the example shown in Figure 5.14 (c). In this case, the receptive field is not large enough to cover the width of the lane where the guard rails at both sides are the critical feature for learning (with guard rails at only one side of the lane, no area will be recognized and

Table 5.3: Test metrics of guard rail-based lane detection with a segmentation network.

Class	Epoch	65					93			
		A4	A5	B5	B5-AllVeh	C2	C4	B5	C4	
1	Precision	0.54	0.88	0.85	0.88	0.71	0.49	0.86	0.84	
	Recall	0.95	0.88	0.97	0.95	0.99	0.99	0.97	0.94	
	F1 score	0.69	0.88	0.90	0.92	0.83	0.65	0.91	0.89	
	mIoU	0.52	0.79	0.83	0.85	0.71	0.49	0.83	0.80	
2	Precision	0.42	0.50	0.46	0.61	0.38	0.24	0.56	0.54	
	Recall	0.93	0.93	0.95	0.97	0.95	0.98	0.93	0.93	
	F1 score	0.58	0.65	0.62	0.75	0.54	0.38	0.70	0.68	
	mIoU	0.41	0.49	0.45	0.60	0.37	0.24	0.54	0.52	

labelled as lane). For model A5, the receptive field is 218×218 corresponding to about 29 m width. Figure 5.14 (d), (e), (f), (g) present the prediction results with model A4 and A5 for a road width equal to about 20 m and a lane without guard rail at its right side, respectively. For model C4 with 4-channel input, the learning procedure is much slower than the others since it contains more input data: its performance is much worse than that of model A5, B5, C2 up to Epoch 65. Up to Epoch 93 in Table 5.3, its performance gets closer to that of model B5, which is however still not better. Since training curve up to Epoch 93 is already flat, no obvious performance improvement can be expected. It can be concluded that input data with more channels including point density, point amplitude, and point positions bring us no advantages over the simple binary input data format. So they just increase the calculation consumption and training time without benefit.

Besides the prediction accuracy, another very important indicator for the model is the prediction efficiency. In this section, the number of measurement cycles predicted per second—the prediction frequency with various GPUs is summarized in Table 5.4. The two single channel models with amplitude values and binary digits have no difference. Models with fewer layers consume less time, but the trade-off between precision and prediction efficiency shall be considered.

Table 5.4: Prediction frequency (cycle/s = Hz) of guard rail-based lane detection with a segmentation network.

GPU	Processing power –single precision (TFLOPS)	Model			
		A5	B5	B4	B3
NVIDIA M2000M	1.4	3.1	3.1	3.3	3.5
NVIDIA Quadro P6000	10.9	24.1	24.1	25.7	27.3
NVIDIA Quadro GV100	16.7	37.0	37.0	39.4	41.8

5.2.8 Radar Road Marking Based Lane Segmentation

The lane segmentation in the last section relies on guard rails at two sides of the road. However, not all roads have such guard rails at both sides. Furthermore, for a road with multiple lanes, it is not possible to build such guard rails between all these lanes.

In chapter 3, a radar detectable road marking / marker with low profile and wide reflection angle range is introduced. In section 5.1, corresponding clustering algorithm based on the intervals between points and the patterns formed by the points are presented. In this section, the lane semantic segmentation results with such radar road markings will be given.

Output Dataset Preparation - Labelling and Data Augmentation

Similar to section 5.2.7, but with reflection points of guard rails replaced by radar road markings, the areas between these reflection points are defined and labelled as driving lanes. Examples can be seen in Figure 5.15 (a). There are two classes in these measurements: lane (purple, class 1) and no lane (no color, class 0). Totally, 680 measurements cycles with 227×227 grid cells in $40\text{ m} \times 40\text{ m}$ in each cycle are labelled under which 96.2% (33714144 grid cells) are class 0 and 3.8% (1325576 grid cells) are class 1.

In order to increase the volume of the training data set, the reflection points in 680 measurement cycles are randomly rotated and transformed before they are added in the training dataset—the data augmentation. Before the transformation,

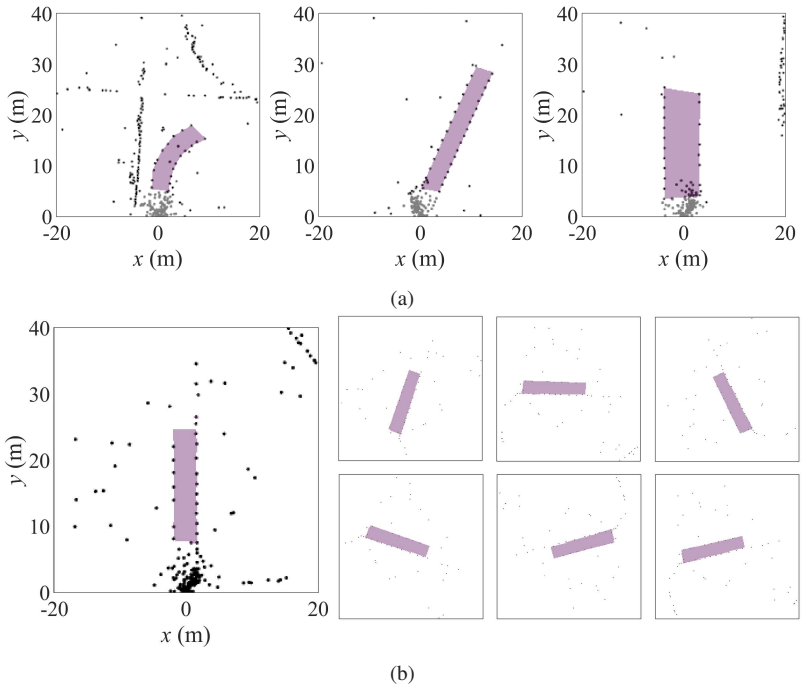


Figure 5.15: (a) Lane labelling on a test field when the vehicle is at position 4, 5, and 6 in Figure 4.13. (b) Training data augmentation with rotating and translating all the reflection points with respect to radar position after excluding the ground clutter reflection points. Test vehicle equipped with radar at its front is at the position of $x = 0$ m and $y = 0$ m.

the reflection points from ground clutter need to be excluded since these points appear only in the near range of the radar sensor. Besides, the data augmentation also helps to avoid the problem of data over fitting during training. Figure 5.15 (b) shows one example of data augmentation of one measurement data used for training by transforming the positions of the reflection points after excluding ground clutter in the near range.

Data augmentation for reflection points only makes sense for binary input features. For features like reflection amplitude, radial velocity, the data aug-

mentation through point transformation is not appropriate since these values change when the positions of the reflection points are transformed.

Training Metrics and Predictions

The prediction performance is compared with various layer numbers of the NN and input formats and the results are presented in Table 5.5. Similar to the results in section 5.3.3, the accuracy with including amplitude features of the reflection points is not improved. For binary input with various NN layers, there is a performance surge from 1 layer to 2 layers and from 2 layers to 3 layers. This improvement decreases after 3 layers and the result stays stable after 5 layers. The receptive field of a 3-layer NN is 50 × 50 grid cells (8.8 m × 8.8 m) according to Table 5.2 whereas that of a 2-layer NN is 3.9 m × 3.9 m. For the measurements, the maximum width of a lane is 7 m (refer to Figure 4.13), so a minimum layer number of 3 is required to cover these measurements which matches good with the results in Table 5.5. In the following sections, a 5-layer model with binary feature input is applied.

Table 5.5: Test metrics of class 1 with respect to the number of layers of the segmentation neural network and input data format.

Input format	Layer number	1	2	3	4	5	6
Single channel binary digit	Precision	0.20	0.52	0.91	0.87	0.89	0.94
	Recall	0.06	0.67	0.79	0.99	0.92	0.86
	F1 score	0.10	0.58	0.85	0.89	0.91	0.90
Single channel normalized amplitude	Precision	0.24	0.31	0.91	0.89	0.86	
	Recall	0.23	0.81	0.87	0.92	0.94	
	F1 score	0.24	0.44	0.89	0.91	0.90	

Feature Map - Features Learned by the Neural Network

After the training process is finished, the learned parameters $\mathbf{W}_{\mathbf{n}^{[l]}}^{[l]}$ can be visualized—the so called feature maps. In Figure 5.16 (a), 64 feature maps of the first layer are presented ($l = 1$ for the first layer and kernel number $\mathbf{n}^{[1]} = 64$ according to the kernel size in Table 5.2). To better understand the features

learned by the NN, synthetic datasets can be generated and fed into the trained model. Part of the tested synthetic datasets can be seen in Table 5.6 where the parameters like the intervals between the points, the lane width, the number of noise points and the points of other objects are adjusted. These parameters of the trained datasets (datasets that are used for network training, not the synthetic data) and the corresponding prediction metrics are also added at the top of the table for comparison. Part of the synthetic data prediction results are plotted in Figure 5.16 (b)–(f).

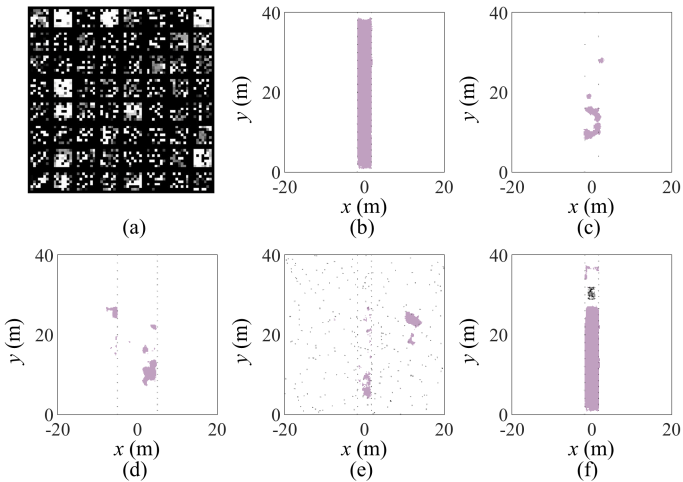


Figure 5.16: (a) Feature map at the first layer of NN learned during training. Segmentation results of synthetic (b) data set 3, (c) data set 5 with larger point intervals, (d) data set 9 with larger lane width, (e) data set 13 with noise, and (f) data set 17 with part of the lane occupied by other objects. Test vehicle equipped with radar at its front is at the position of $x = 0$ m and $y = 0$ m.

From the Table 5.6, it can be seen that if the point interval between the points is increased or decreased (synthetic datasets 1 to 5 and Figure 5.16 (c)), the prediction score decreases dramatically. This is also valid for the results of a changed lane width (synthetic datasets 6 to 10 and Figure 5.16 (d)). This proves also that the learned features of the NN is the width of the lane and the interval between the reflection points. With more points of the noise (synthetic datasets 11 to 14 and Figure 5.16 (e)) and other objects (datasets 15 to 17 and Figure 5.16 (f)), the prediction performance also deteriorates which is within

Table 5.6: Test metrics of synthetic datasets with trained model.

		Point in- interval (m) (left, right)	Lane width (m)	Noise point number	Object point number	Precision	Recall	F1 score	
Measurement data / training data		(1.5, 2.0)	3.5	N.A.		0.89	0.92	0.91	
		(2.0, 1.5)	3.5						
		(2.0, 2.0)	7.0						
Synthetic datasets	1	(0.7, 0.7)	3.5	0		1.00	0.69	0.82	
	2	(1.5, 2.0)				0.91	0.93	0.92	
	3	(2.0, 1.5)				0.95	0.94	0.95	
	4	(4.0, 3.0)				0.82	0.79	0.80	
	5	(8.0, 6.0)				0.85	0.12	0.21	
	6	(2.0, 1.5)	2.6	0		0.68	0.74	0.71	
	7		6.0			0.98	0.64	0.77	
	8		8.0			1.00	0.80	0.89	
	9		10.0			0.77	0.05	0.09	
	10		14.0			0.46	0.03	0.06	
	11		3.5	16	0		0.95	0.93	0.94
	12			64			0.98	0.90	0.94
	13			256			0.49	0.08	0.14
	14			1024			0.11	0.03	0.05
	15		0		8	0.97	0.91	0.94	
	16				32	0.93	0.89	0.91	
	17				128	0.94	0.66	0.78	

expectation since such cases are not included in the training dataset. These synthetic datasets can also be included into the training datasets to improve the segmentation performance and robustness, and also to decrease the work to measure and record data in such cases in the real world.

Improve Segmentation Stability with Bayes’ Theorem

With data augmentation, the segmentation performance increases. However, some prediction errors appear in certain single measurement cycles which makes the prediction a bit unstable. Figure 5.17 (a), (b), (c) present such errors, and most of them are FP errors (lane as the detection target). In order

to increase the prediction stability, several consecutive predictions p_n can be combined to get a joint probability P_n according to Bayes' Theorem:

$$\log \frac{P_n}{1 - P_n} = \sum_{i=n-k+1}^n \log \frac{p_i}{1 - p_i} \quad (5.11)$$

where p is the NN inferred probability from i^{th} single measurement that a grid belongs to the lane, n is the current measurement cycle, and k is the number of consecutive preceding predictions.

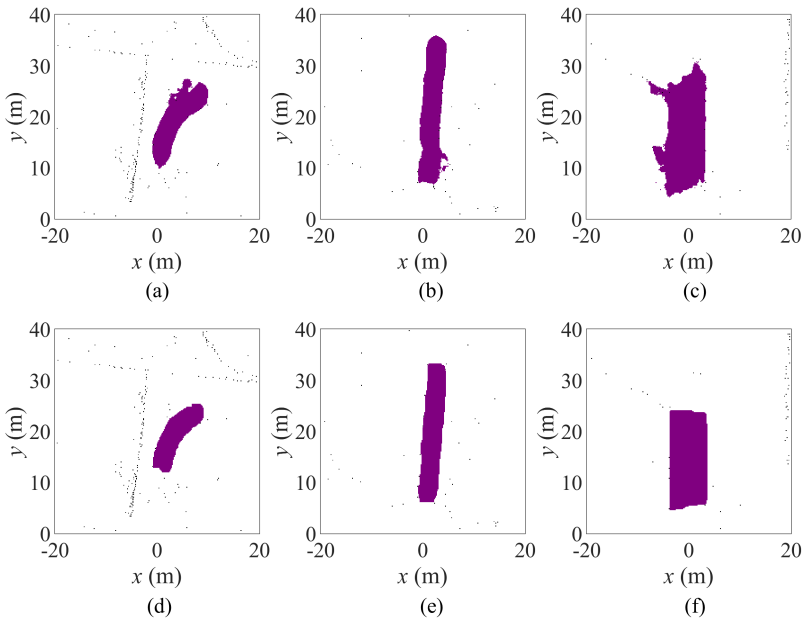


Figure 5.17: Segmentation results with ((d) to (f)) and without ((a) to (c)) Bayes' recursion.

Generally, there are two approaches to get the joint predictions P_n like shown in Figure 5.18 (a) where two consecutive measurements A and B are considered as example:

- in the first approach, a global grid map is used as the reference grid map and all the reflection points from related measurement cycles are filled

into this reference grid map. In the example of Figure 5.18 (a), the vehicle makes a rotation from position A to B . The reflection points of these two measurements are both filled into the same grid map in grey color. For the first measurement, the orientation of the detected area (solid blue rectangle, assumed that the radar is mounted in front of the vehicle) is identical to that of the reference grid map, whereas for the second measurement, the detected area by the radar (dashed green rectangle) is not. Then a minimum rectangle that is aligned with the reference grid map cells is created (solid green rectangle) and the cells inside this rectangle are used as the NN input data for the second measurement. With this method, the prediction cells of both measurements (filled rectangles in green and blue color) will overlap with each other without offset. During Bayes calculation step, the prediction cells that are not overlapped with preceding prediction cells are set to 0.5, indicating that the prediction cell of this measurement will not influence the value of the joint prediction P_n . This approach also shows that for predicting test data with the trained models, the input dimension of the test data can be different from that of the trained data (like the solid green and blue rectangles can be both predicted by the trained model but only the dimension of the blue rectangle is identical to that of the trained data). This indicates that the features learned by the NN depend not on the absolute positions of the features, but on the local features.

- in the second approach, after the detection points are collected (solid blue and dashed green rectangles), they are immediately sent to the NN to conduct predictions (filled solid blue and dashed green rectangles). However, the prediction cells of these two measurements will not overlap totally with each other, meaning additional algorithms are needed to merge their prediction results besides Bayes' Theorem. Like the approach 2 in Figure 5.18 (a), the prediction cell $p_n(1)$ aligns with none of $p_{n-1}(1)$, $p_{n-1}(2)$, $p_{n-1}(3)$, and $p_{n-1}(4)$. So the value p_{n-1} to calculate the joint prediction P_n is unclear. One solution is to calculate the weighted average based on the percentage of the overlapped area between cell $p_n(1)$ and $p_{n-1}(1)$, $p_{n-1}(2)$, $p_{n-1}(3)$, $p_{n-1}(4)$. Since this approach is more complex and consumes more calculation time, approach 1 is preferred.

To calculate the joint predictions after the movement of the vehicle, the relative position after the movements are needed. To get these data, CAN (Controller

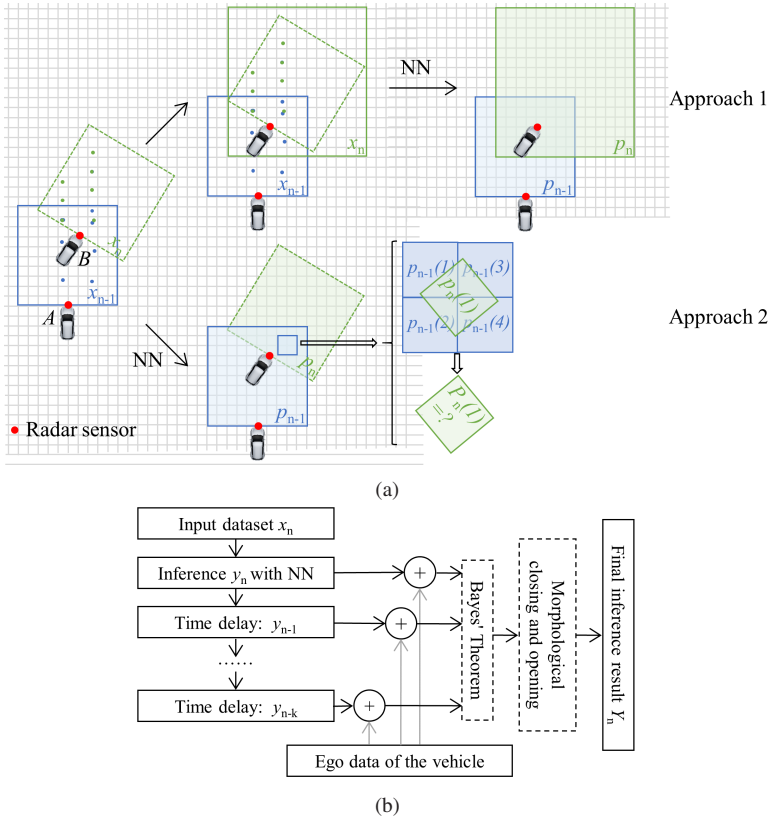


Figure 5.18: (a) Two approaches to calculate the joint probability P_n from consecutive preceding predictions. (b) Calculation flow of a joint prediction with Bayes' Theorem and morphological closing and opening algorithm.

Area Network) data, ADMA data, or radar based SLAM algorithm can be utilized.

After getting the joint prediction P_n , morphological closing and opening algorithms are employed in order to eliminate minor outliers, to fill small gaps, and to smooth the contours. The whole processing chain can be seen in Figure 5.18 (b). The improved joint prediction results of Figure 5.17 (a), (b) and (c) are correspondingly presented in Figure 5.17 (d), (e) and (f).

Contour and Bounding Box Detection

After each pixel is classified, a contour or bounding box describing the shape, size and orientation of the object can be created. This can be finished by processing the prediction results of the semantic segmentation NN. However, if only the boxes need to be detected, it is not necessary to carry out the pixel-wise prediction any more. Because the number of the parameters to describe such boxes is much smaller than the number of the pixels to be predicted, by employing an NN architecture that predicts the boxes directly without pixel-wise classification, the prediction efficiency can be increased.

Figure 5.19 (a) and (b) present two labelling examples of the detection points in Figure 5.12. The labelling boxes are irregular quadrilaterals that are defined with eight geometric parameters like shown in Figure 5.19 (c). To create the ground truth vector $\hat{y}^{(i)}$ and to describe the NN output $y^{(i)}$, a confidence score p_e that denotes the probability of the existence of an object and a class score p_k that predicts the class of the object are added. By taking the NN architecture of YOLO in [RF18] but replacing the prediction output of rectangles with irregular quadrilaterals defined in Figure 5.19 (c), the prediction results of the detection points in Figure 5.12 are presented in Figure 5.20 where the numbers beside the predicted boxes are $p_e p_k$.

Table 5.7 presents the evaluation results of the predictions (AP_{50} denotes the average precision of the predictions whose detection boxes having the IoU with the ground truth boxes larger than 0.50 considered as correct predictions). Because the results of AP_{90} are nearly zero, it can be concluded that the predicted boxes match not perfectly with the labellings. This conclusion can also be found in the visualized prediction result in Figure 5.20 (a) where the predicted contour does not match perfectly with the road (the predicted box

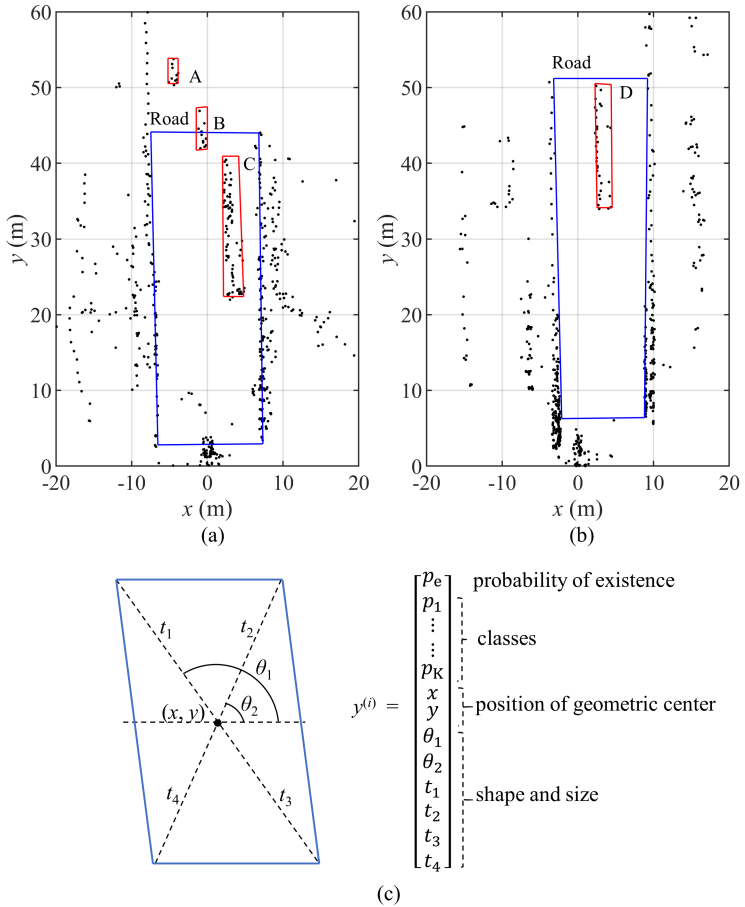


Figure 5.19: (a) Contour and bounding box labelling of the detection points in Figure 5.12. (b) Parameters to describe the box.

is shifted to left). If we compare the mIoU in Table 5.7 with that in Table 5.3 (model *B5-AllVeh*), the results in Figure 5.20 (a) with those in Figure 5.14 (a), (b), we can conclude that the prediction accuracy of such a NN is not as good as the previous presented semantic segmentation NN. However, the prediction

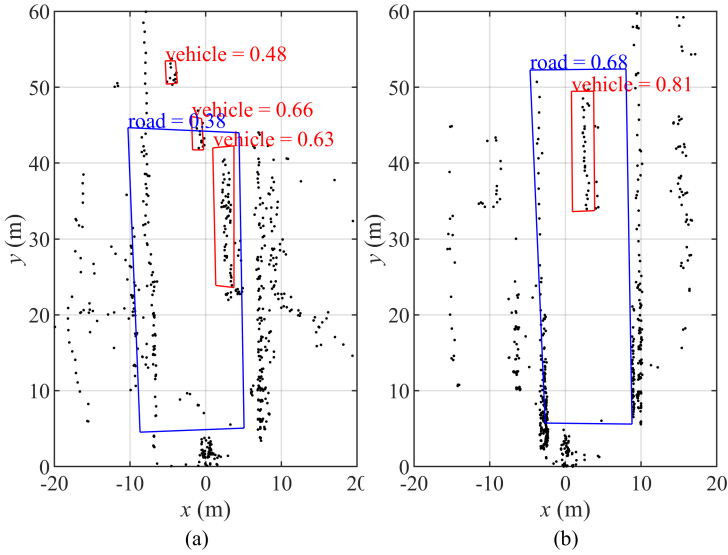


Figure 5.20: Contour and bounding box prediction results of the detection points in Figure 5.12 with YOLO [RF18] by replacing the prediction output of rectangles in [RF18] with irregular quadrilaterals defined in Figure 5.19 (c).

frequency with such a NN (GPU: NVIDIA M200M) is about 6.2 Hz, which is faster than the prediction with the segmentation NN in Table 5.4.

Table 5.7: Evaluation results of contour and bounding box prediction.

	AP ₅₀	AP ₇₅	AP ₉₀	mIoU
Road	0.76	0.20	0.02	0.66
Vehicle	0.73	0.08	0.01	0.60

5.2.9 Summary

This section presents the working principle of NNs and applies a segmentation network for radar reflection point-based lane segmentation. It shows the po-

tential of DL in road segmentation with high resolution radar data, a method which is currently mostly implemented with optical sensors like camera or LiDAR. A low level sensor fusion and its joint-segmentation carried out by different sensors (e.g. radar and video) can support to improve the robustness of the system for autonomous driving functions like free space detection, lane course prediction and automated vehicle steering. In the next section, instead of pixel-wise semantic segmentation, point-wise segmentation is discussed.

5.3 Point Cloud Lane Segmentation with Neural Networks

In section 5.2, segmentation is based on grid cells by filling radar reflection points into them like shown in Figure 5.10. This approach is similar to segmentation on pixel-level for video images. However, such a filling process by manually creating a grid map causes problems. For example, the filling of the points into the grid cells will unavoidably introduce additional errors to these point features. So the feasibility of taking directly the point itself as the NN input is worth discussing. Besides, using points as input also decreases the input data size. For example, we have counted the number of reflection points collected by the high-resolution automotive radar prototype [MSK15], [MSK17] tested on highways: there exist in total 6,234,499 reflection points in 10,154 measurement cycles with the lateral range of the receptive region from -20 m to 20 m and longitudinal range from 0 m to 60 m, resulting in about 614 reflection points in one measurement cycle on average. If a grid map is created in this receptive region with 0.5 m resolution, then 120×80 grid cells are generated for every measurement cycle, which is much larger than 614. This comparison has not yet considered that if a 3D grid cubic is employed or if the resolution of the created grid map is better than 0.5 m (the resolution of an automotive radar can be much better than 0.5 m), this difference will be even much larger. So it is advantageous to make predictions directly based on the points also from the view of input data size.

However, to use reflection points directly as the NN input data, several problems need to be solved:

- Unstructured input data: unlike the grid cells, the reflection points have no fixed structure, so the conventional CNN and CNN-based segmentation NN can not be applied to these reflection points.
- Varying point number: the number of the collected reflection points varies with respect to the measurements. The number of reflection points of the same object can be different even with the same radar and radar setup. However logically, this point number variation shall not influence the prediction results.
- No defined point sequence: the input sequence of the reflection points into the NN is not defined and can be different, which however shall also not lead to different predictions. In other words, the prediction shall be independent of the input point permutation. So sequence-related NNs like RNN (Recurrent Neural Network), LSTM (Long Short-Term Memory) are not appropriate.

In this chapter, the reflection points collected by a high-resolution radar (point cloud) in single-cycles are semantically segmented, especially w.r.t. lanes, or rather, guard rails on the highway and radar road markings on the test field. A NN originally designed for LiDAR point cloud segmentation is modified to improve the prediction performance for radar data.

5.3.1 Classification with Support Vector Machine (SVM)

SVM is a branch of supervised machine learning and is a simpler method that requires less computational effort to classify points compared with DL. A SVM is a classifier that utilizes a trained hyperplane (mostly with a transformation kernel to convert the inputs to higher dimensions) to accomplish the point cloud classification. However, SVM is usually only effective in cases where the number of the data dimension is larger than the number of training data, which is not the case in this chapter.

5.3.2 PointNet and PointNet++

In order to solve the problems raised at the beginning of this section, authors in [QSKG17] and its improved version [QYSG17] proposed point-wise segmentation NNs called PointNet and PointNet++ for classification of the reflection points collected by LiDAR sensors. The main principle of PointNet is to integrate a symmetric function into the NN. Typical symmetric functions can be a *max* function, a *sum* function, etc. With a symmetric function integrated in the NN, the input data is converted into a feature vector that is not dependent on the number of the input reflection points and its permutation. Figure 5.21 (a) illustrates such a process where N is the number of input points, $C^{[l]}$ is the number of features of a reflection point. The input points are organized like shown in this plot. Then, $C^{[l+1]}$ kernels are employed to convolve with the input data. The height of the kernel is 1 and its width equals to the feature number of the input data $C^{[l]}$ which is called a single layer perceptron. After that, a $N \times C^{[l+1]}$ matrix is generated and for each column of the matrix, a symmetric function is applied to get single elements like the filled squares in the figure, so for a matrix with $C^{[l+1]}$ columns, a vector containing $C^{[l+1]}$ elements is created. This vector features the whole input data points and thus is called the global feature. Figure 5.21 (b) shows a PointNet architecture [QSKG17]. The MLP consists of multiple layers of a single layer perceptron in Figure 5.21 (a) and the number in the parentheses are the feature numbers $C^{[l]}$. Additional transformation T-nets are added to take the point cloud geometrical transformation (like move, rotate) into account. The global feature after the symmetric function (*max* function here) is repeated with the number of points and concatenated with point features to generate a feature matrix. Another MLP is used with the feature number of the last layer equal to the number of classes c . So the output provides the probability of every point belonging to each class.

However, such a network features only the global behavior of the input point cloud with the global feature. As mentioned in section 5.2 that a grid-based segmentation network is able to learn local features, in order also to be able to learn local features of the point cloud, [QYSG17] proposes a network based on PointNet—the PointNet++.

The basic idea of PointNet++ is to divide the point cloud into several groups and for each group, a PointNet is used. So this is a hierarchical structure with the feature of each group—the local feature constituting the feature of

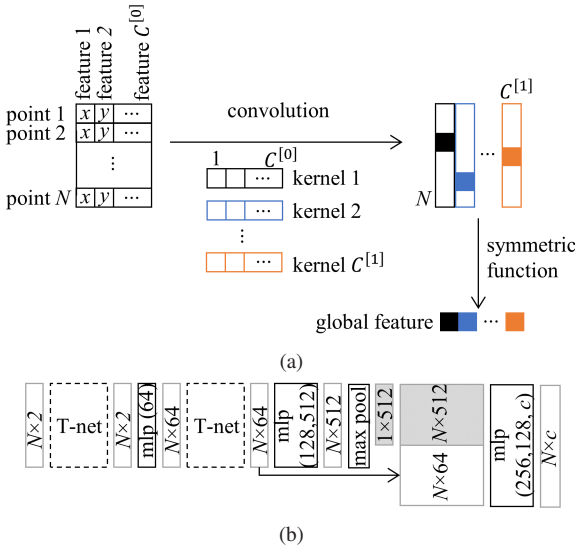


Figure 5.21: (a) Method to get global feature independent of input point number and its permutation by utilizing symmetric functions. (b) Architecture of a PointNet [QSKG17].

the higher hierarchy. Figure 5.22 illustrates the architecture of a PointNet++ with 5 hierarchies. Similar to a grid-based CNN, this architecture consists mainly of two parts: the set abstraction part for feature learning and the feature propagation part for reverse feature mapping to every point.

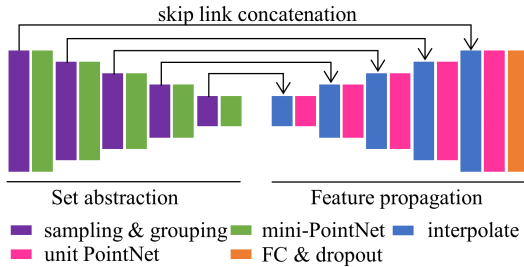


Figure 5.22: Architecture of a 5-layer (hierarchies) PointNet++ [QYSG17].

One layer in the set abstraction part includes a sampling layer, a grouping layer, and a mini-PointNet layer. The sampling layer samples N' centroids from the N input points and each centroid is responsible for its surrounding points in a local region. So N' groupings corresponding to N' local regions exist after this step. A mini-PointNet, which is a simplified version of PointNet based on the structure in Figure 5.21 (a) is employed to get the features of these N' point groupings with N' feature vectors. These N' feature vectors are then used as input points of the following layers recursively.

After the features in the set abstraction part are extracted, the feature propagation part will reverse these features into class classifications for each point. Every layer in this part includes interpolation, unit PointNet, FC (Fully Connected) and dropout layers. The interpolation layer gets the point positions from the corresponding set abstraction layer and unit PointNet is a simplified mini-PointNet with the column number of the convolution kernel equal to 1.

In [QYSG17], FPS (Farthest Point Sampling) is used for selecting the N' centroids, ball query or kNN (k Nearest Neighbors) is used for finding surrounding reflection points around each centroid. Additionally, MSG (Multi-Scale Grouping) or MRG (Multi-Resolution Grouping) is employed to address the problem of point density variation with respect to different ranges between the reflection points and the radar. For the following implementations, the script in Tensorflow is extended based on the script of the author [CWZZ] where ball query and MRG are employed.

5.3.3 Guard Rail Based Lane Segmentation

Labelling and Training Datasets

In this section, all points are assigned to three classes: vehicles (class 1), guard rails (class 2), and others like lawn, trees, and bushes at the road side (class 0). For the guard rails, when several guard rails exist at the same side of the vehicle, the nearest one will be labelled as guard rail, and the other one as unlabeled since only the guard rail closest to the vehicle defines the drivable lane for this vehicle. Figure 5.23 shows two labelling examples of single-cycle radar detection points on a highway. A, B, C, and D are vehicles (class 1), E and F are reflection points from guard rails at both sides of the vehicles.

Although G is guard rail, these points are not labelled as class 2 because it is at the outer side of F.

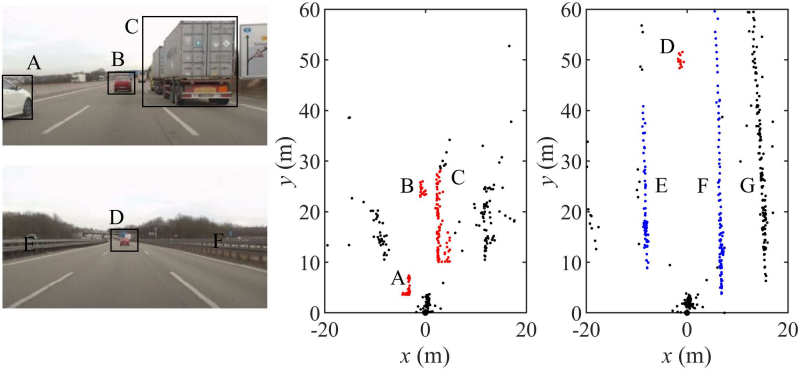


Figure 5.23: Single-cycle radar detection points on a highway and point-level labelling (red for class 1 of vehicles, blue for class 2 of guard rails, black for class 0 of others). Test vehicle equipped with radar at its front is at the position of $x = 0$ m and $y = 0$ m.

Two datasets are separately trained for comparison:

- Dataset A: 6,673 measurement cycles, under which are 2,249,855 points of class 0 (63.2%), 469,179 points of class 1 (13.2%), and 838,745 points of class 2 (23.6%).
- Dataset B: 10,154 measurement cycles, under which are 4,329,962 points of class 0 (69.5%), 743,185 points of class 1 (11.9%), and 1,161,352 points of class 2 (18.6%).

80% of the training datasets are used for training, the remaining 20% are used for evaluating trained models.

Feature Adjustment

As mentioned in the previous section, the NN requires to divide the reflection points into groups, this grouping however, depends only on the geometric features x and y . It can be proven that if non-geometric features like reflection

magnitude, velocity are also used for grouping, the training and testing results of the NN will be very poor.

Additionally, [QYSG17] is proven to be very robust to point density variation. However, the point density is a very important feature, for example, the reflection points from the guard rails and the grass at the road side can both comprise straight lines, whereas the ones of the guard rails have more regular intervals between them than the ones of the grass. So in addition to the pattern of the points, the point distribution property shall be also considered in the NN.

Figure 5.24 shows two approaches to incorporate such an additional feature where (a) illustrates a method to concatenate the feature r_{\min} into the NN during grouping process, like MRG. r_{\min} is the distance from the centroid point to the nearest point excluding the points within a small value $r_{\text{threshold}}$ that is used to exclude the points coming from the side lobe of FFT / angle estimation of the centroid point. For multilayer NN, this feature can be selectively concatenated in all layers or only in certain layers and it is also possible to concatenate other point distribution features during this step. Such concatenation is proven to be very time- and processing-consuming when compared with the following method.

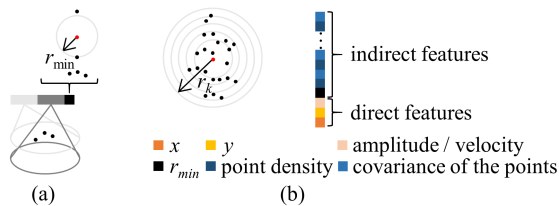


Figure 5.24: (a) NN incorporating point distribution features in MRG or (b) include additional features in input dataset.

Instead of concatenating the additional features in the NN, they can be also added as additional input features (indirect features) besides the geometric features (direct features), like the example shown in Figure 5.24 (b). In order to describe the point distribution features, additional indirect features like point density and point coordinate covariance can be used. In this example, for each centroid, k concentric circles with radii r_k are created and the number of the reflection points and the covariance of the points within each circle is counted and calculated. As mentioned previously, these additional features shall not be

used for sampling and grouping to prevent poor training and prediction results. At last, all these features need to be normalized (feature normalization) before they are concatenated as the input features.

The detected velocity v of each point can be used to distinguish static objects from moving objects. On the one hand, [SHDW18] has proven that v helps to improve the training and prediction performance, so this is no longer the emphasis of this section. On the other hand, using v can be limited, for example, guard rail and grass are all static and the vehicles are also static if a traffic jam is encountered.

At last, various radii values of grouping can be selected in various layers of the NN. So the influence of various radii, together with the number of NN layers on the prediction performance, will both be investigated in the following section.

Segmentation Results

This section presents 4 different tests as listed in Table 5.8. The parameter setup for every test and their corresponding evaluation results are listed in Table 5.9. For example, Radii 1 describes a 4-layer NN with the grouping radii equal to 4 m, 8 m, 16 m, and 32 m. Analyses are as follows:

- Compare Test 1 and Test 2: in Test 2, an additional feature is added into the feature vector during grouping process and its evaluation F1 score is much more stable than that of Test 1. In Test 1, with the change of the radii, the F1 score of class 0 varies in the range from 0.87 (radii 5) to 0.95 (radii 2) whereas for Test 2, the range is from 0.90 (radii 4) to 0.92 (radii 1). So the performance of Test 1 depends strongly on the radii and when an additional feature is added, this dependency disappears. From another point of view, the F1 score of Test 2 shows advantages over Test 1 only with larger radii (radii 4 and radii 5). Similar conclusions can be also drawn from Test 1 and Test 3.
- Compare Test 2 and Test 3: For all radii, Test 3 shows better results than Test 2.
- Compare Test 3 and Test 4: the only difference between Test 3 and Test 4 is the volume of the training dataset. Test 4 has 52.2% more training data

than Test 3 and their evaluation results are very similar. This indicates that the tests are repeatable and stable.

- The number of NN layers: in Test 3, the number of NN layers is decreased down to one layer. However, the F1 score keeps nearly unchanged until layer 1, where that of class 0, class 1, class 2 decreases from 0.94 to 0.92, from 0.95 to 0.93, from 0.89 to 0.85, respectively. So for this application, the minimum layer number shall be 2.

Table 5.8: Various tests of point-wise semantic segmentation.

	Test 1	Test 2	Test 3	Test 4
Concatenate features in NN	No	Yes	No	No
Concatenate features in input	No	No	Yes	Yes
Training and evaluation dataset	dataset A	dataset A	dataset A	dataset B

Table 5.9: Evaluation metrics and parameter setups of various measurements on a highway.

Name	Radii (m)	Layer number	Evaluation F1 score (class 0, class 1, class 2)			
			Test 1	Test 2	Test 3	Test 4
Radii 1	(4, 8, 16, 32)	4	(0.92, 0.93, 0.85)	(0.92, 0.92, 0.85)	(0.93, 0.94, 0.86)	(0.94, 0.94, 0.86)
Radii 2	(8, 16, 32, 64)		(0.95, 0.95, 0.90)	(0.92, 0.91, 0.85)	(0.93, 0.94, 0.87)	(0.95, 0.95, 0.88)
Radii 3	(16, 32, 64, 64)		(0.93, 0.93, 0.88)	(0.91, 0.91, 0.85)	(0.94, 0.95, 0.89)	(0.95, 0.96, 0.89)
Radii 4	(32, 64, 64, 64)		(0.89, 0.86, 0.79)	(0.90, 0.88, 0.81)	(0.94, 0.94, 0.88)	(0.95, 0.95, 0.88)
Radii 5	(64, 64, 64, 64)		(0.87, 0.85, 0.78)	(0.91, 0.88, 0.84)	(0.94, 0.94, 0.89)	(0.95, 0.95, 0.89)
Radii 6	(16, 32, 64)	3			(0.94, 0.95, 0.89)	
Radii 7	(16, 32)	2	/	/	(0.94, 0.95, 0.89)	/
Radii 8	(16)	1			(0.92, 0.93, 0.85)	

Besides the comparison of the numerical metrics in Table 5.9, the prediction results of untrained datasets with trained models are also visualized and che-

cked. It can be proven that the trained model in Test 3 is more stable and accurate than that in Test 1, even though the numerical metrics show similar results (like radii 2 in Test 1 and radii 3 in Test 3). One such example can be seen in Figure 5.25 where three results that are predicted with the three distinct trained models are compared: model $M1$ in Test 1 with radii 5; model $M2$ in Test 1 with radii 2 (best in Test 1); mode $M3$ in Test 3 with radii 3 (best in Test 3). Following conclusions can be drawn from these results:

- The reflection point group A shall be predicted as class 0 (others, black), so the best prediction comes from model $M3$ and the worst comes from model $M1$.
- The reflection point group B shall be predicted as class 2 (guard rails, blue), but with model $M2$, one point is mistakenly predicted as class 1 (vehicle, red). Otherwise, the prediction results of the three models of this group are similar.
- The sparse reflection point group C comes from noise or ground clutter and shall be predicted as class 0. However both with model $M1$ and $M2$, these points are wrongly predicted as class 1. The point distribution feature of these sparse points are quite different from the reflection points from vehicles and they are correctly predicted by model $M3$. The number of these sparse points is quite small, so their predictions may not correctly be reflected in the numerical metrics in Table 5.9, even though they can be very critical since such incorrect predictions could trigger functions like automatic braking by mistake.
- The reflection points in group D come from the truck. They are best predicted with model $M3$.

Prediction Efficiency

Besides the prediction accuracy, the time consumed for a prediction is also a very important criterion. The number of measurements that the NN predicts in one second—the prediction frequency of Test 1 and Test 3 is listed in Table 5.10. The results show that:

- the influence of radii on prediction frequency is very small;

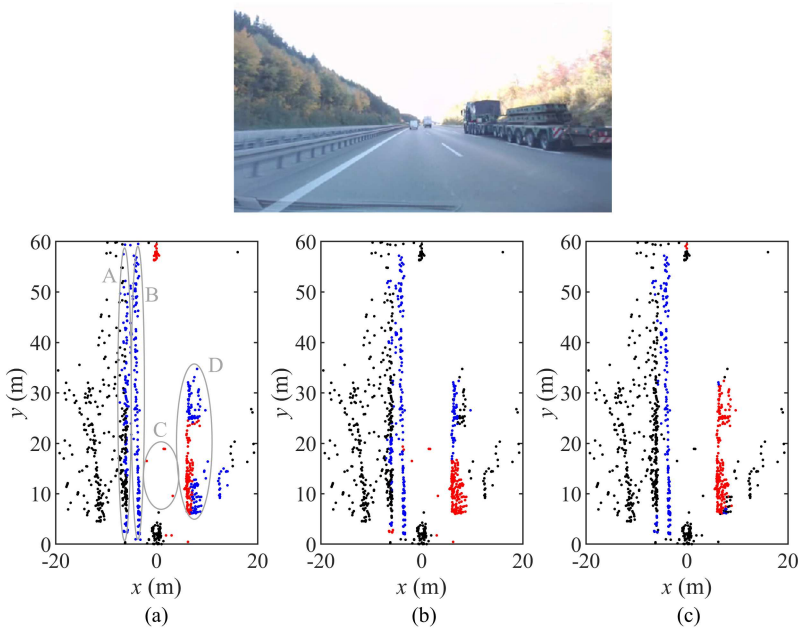


Figure 5.25: Comparison of prediction results with various trained models: (a) model $M1$; (b) model $M2$; (c) model $M3$.

- by adding additional features in the input, the prediction performance is improved, and the prediction efficiency is nearly not affected;
- with fewer number of NN layers, the prediction efficiency increases, however, the prediction performance degrades. With considering the trade-off between these two criteria, radii 7 is the best choice;
- when comparing Table 5.11 with Table 5.4, it can be concluded that although the input data size of the PointNet++ is much smaller than that of the grid-based input data of SegNet, the prediction efficiency is roughly similar. This is because during the sampling and grouping process of PointNet++, a lot of time is consumed to calculate the distances between the points.

Table 5.10: Prediction frequency comparison in Hz with respect to radii of Test 1 and Test 3 (GPU: M2000M).

Radii	1	2	3	4	5	6	7	8
Test 1	2	1.8	2	2	2	/		
Test 3	2	/	2	/	2	2.6	4.4	8.9

In order to increase the prediction frequency, model compression [CWZZ18] without losing prediction accuracy can be considered. A GPU with higher computational power can be employed, too. Table 5.11 shows the estimated prediction frequency with two additional NVIDIA GPUs for this application.

Table 5.11: Estimated prediction frequency with various GPUs (Test 3, radii 7).

GPU (NVIDIA Quadro)	Processing power (TFLOPS)	Estimated prediction frequency (Hz)
M2000M	1.4	4.4
P6000	10.9	34.4
GV100	16.7	52.5

5.3.4 Radar Road Marking Based Lane Segmentation

Labelling and Training Datasets

For the tests in the test track like shown in Figure 4.13, the reflection points are classified into two classes: radar road markings (class 1) and others (class 0). In Figure 5.26 (a), a labelling example (the red color stands for class 1 and the black for class 0) when the test vehicle is at position 3 in Figure 4.13 is presented.

The training dataset in this section (dataset *C*) includes 289,074 points of class 0 (95.6%) and 13,172 points of class 1 (4.4%). Two tests are compared in this section: Test 5 where only direct point coordinate values are used as input features and Test 6 where additional indirect point distribution features are added as input features. The corresponding trained models are named model *M5* and model *M6*, respectively.

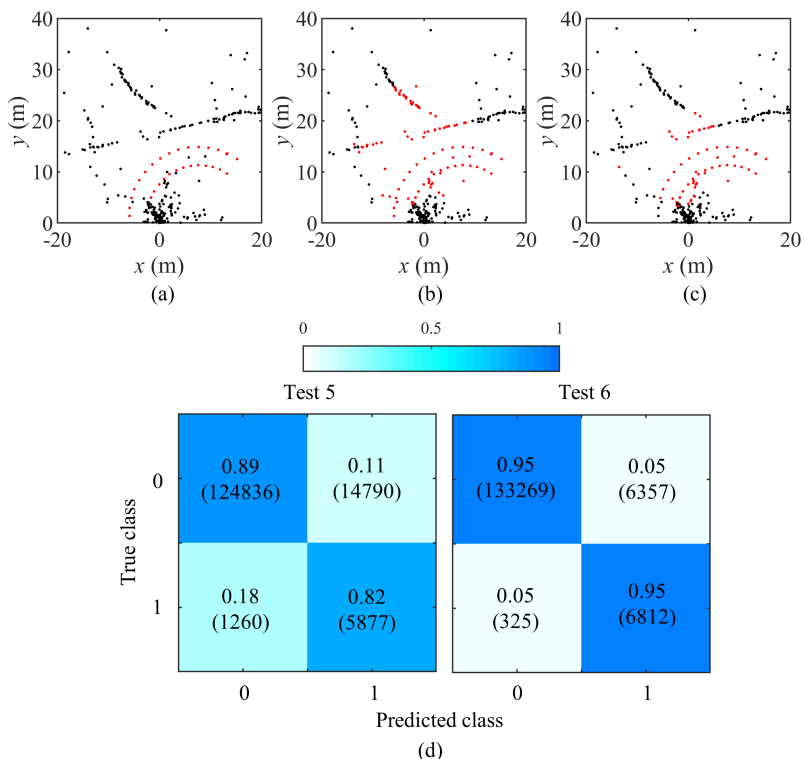


Figure 5.26: (a) Labelling example of radar road markers. (b) Prediction results with model $M5$. (c) Prediction results with model $M6$. (d) Evaluation confusion matrices of Test 5 and Test 6. Test vehicle equipped with radar at its front is at the position of $x = 0$ m and $y = 0$ m.

Segmentation Results

Similar to section 5.3.3, the NN parameters are tuned for comparison and the results are shown in Table 5.12. Similar conclusions of section 5.3.3 can be drawn except that the performance improvement with the additional input point distribution features is more obvious in this section. Figure 5.26 (b) and (c) present two corresponding prediction results with model $M5$ and $M6$ and Figure 5.26 (d) shows the evaluation confusion matrices of Test 5 and Test 6,

where the number in the parentheses indicate the number of points. From all these metrics, it can be concluded that the additional input distribution features help to improve the prediction performance.

Table 5.12: Evaluation F1 score of point-wise radar road marking segmentation.

Radii	Evaluation F1 score (class 0, class 1)	
	Test 5	Test 6
1	(0.93, 0.39)	(0.97, 0.65)
2	(0.91, 0.34)	(0.97, 0.60)
3	(0.94, 0.42)	(0.98, 0.67)
4	(0.89, 0.31)	(0.97, 0.61)
5	(0.85, 0.25)	(0.98, 0.70)
6		(0.98, 0.70)
7	/	(0.98, 0.67)
8		(0.97, 0.61)

5.3.5 Summary

This section presents point-wise segmentation of radar point clouds, especially for the application of guard rail and radar road marking based lane segmentation. The PointNet++, primary designed for LiDAR point cloud segmentation, is adapted and utilized in this section. Better prediction results are achieved when additional point distribution features are concatenated to the geometric features of the points. The influence of NN parameters like grouping radii and number of layers are analyzed and compared. With the further improvement of the detection precision of the automotive radar, environmental perception with automotive radar sensors by using NNs and DL methods will become more and more likely and applicable. To step forward, further improvements can be made: Firstly, a NN with less processing and storage requirements, but without losing or even with higher prediction accuracy shall be developed; Secondly, with adding timing information (multiple consecutive measurements) to the NN, the prediction accuracy can be expected to become much better.

6 Summary and Outlook

To complement the weakness that the lane detection function carried out solely by video cameras works not well under certain adverse environmental conditions, and to increase the robustness and reliability of the system by sensor data fusion with the currently existing massively equipped automotive radars, this dissertation discusses the capability and feasibility to detect the lane markings with a high-resolution automotive FMCW radar. Both simulations and on-road measurements with various radar road markers are conducted. An asymmetric corner reflector with a large bottom plate and a low vertical profile is preferred. This reflector can be integrated into the current road markings or can be used solely as a radar road marker. When these reflectors are integrated at the two sides of the lane, it is also possible to determine the moving status of the vehicle by analyzing their reflection characteristic in the Range-Doppler domain. With a geometrical coding of these reflectors, more information like the indication of oncoming specific zones or the maximum allowed driving velocity, etc. can be incorporated in these reflectors. The reflection points of these low-profile reflectors can be stored and used to create a “signature“ map of the road with algorithms like SLAM—a radar road signature for accurate vehicle localization by matching the real-time collected reflection points with the map, as a complement to GNSS-based vehicle localization. With such reflectors and currently existing guard rails, traffic poles, etc., a radar-based lane detection system can make the autonomous vehicle more reliable and safer. External coverings like leaves, gravel, etc. on these novel radar reflectors still need a practical solution before its industrialization. A larger detection range by improving the radar sensitivity or the RCS of the reflector is always an option for further improvements in the near future.

Suitable unsupervised and supervised clustering and classification algorithms are elaborated in this dissertation. In unsupervised clustering, the reflection points of the radar road markers are clustered by analyzing their intervals, patterns and reflection magnitudes. With a 2D antenna array, the height of

the objects can be determined, too. This enhances the classification performance for the radar road markers by selecting the reflection points according to the radar mounting height. In the supervised clustering and classification algorithm—the neural network based DL algorithm, both grid- and point-based networks are introduced. Very promising results are achieved, which proves the feasibility and potential of DL for radar application. Further work to increase the accuracy by adjusting the architecture of the network, incorporating timing information, and increasing the processing efficiency of the algorithm by model compression algorithms is proposed for further performance improvement.

By incorporating the radar road markers in the lane markings painted with color, sensor fusion algorithms for lane detection based on both camera and radar data can be developed. The fusion can be both carried out for low- and high-level data. A sensor fusion algorithm with a DL NN that reads both the camera and radar data can be a very promising approach (low-level fusion). An alternative is, of course, also to feed the camera and radar data in separate NNs and merge them together afterwards (high-level fusion).

Bibliography

- [Bal81] D. Ballard. Generalizing the Hough Transform to Detect Arbitrary Shapes. *Pattern Recognition*, 13(2):111–122, 1981.
- [BKC17] V. Badrinarayanan, A. Kendall, and R. Cipolla. SegNet: A Deep Convolutional Encoder-Decoder Architecture for Image Segmentation. *IEEE Tran. on Pattern Analysis and Machine Intelligence*, 39(12):2481–2495, 2017.
- [Bog12] O. Bogatine. Tracking Lane Marker Position Through Use of Information-transmitting Device. Apr. 2012. USA Patent US2012/0098657A1.
- [CSSW17] L. Caltagirone, S. Scheidegger, L. Svensson, and M. Wahde. Fast LIDAR-based Road Detection Using Fully Convolutional Neural Networks. In *IEEE Intelligent Vehicles Symposium (IV)*, pages 1019–1024, Los Angeles, CA, USA, Jun. 2017.
- [CT03] C.-Y. Chan and H.-S. Tan. Evaluation of Magnetic Markers as a Position Reference System for Ground Vehicle Guidance and Control. 2003. California Partners for Advanced Transportation Technology, University of Berkeley.
- [CWZZ] Yu Cheng, Duo Wang, Pan Zhou, and Tao Zhang. PointNet++: Deep Hierarchical Feature Learning on Point Sets in a Metric Space (GitHub). [Online]. Available: PointNet++: Deep Hierarchical Feature Learning on Point Sets in a Metric Space (GitHub).
- [CWZZ18] Yu Cheng, Duo Wang, Pan Zhou, and Tao Zhang. Model compression and acceleration for deep neural networks: The principles, progress, and challenges. *IEEE Signal Processing Magazine*, 35:126–136, 2018.
- [DH72] R. O. Duda and P. E. Hart. Use of the Hough Transformation to Detect Lines and Curves in Pictures. *Communications of the ACM*, 15(1):11–15, 1972.

- [dPJ13] M. Braga de Paula and C. Rosito Jung. Real-time Detection and Classification of Road Lane Markings. In *Proc. 26th Conference on Graphics, Patterns and Images*, pages 83–90, Arequipa, Peru, Aug. 2013.
- [FKMW16] Z. Feng, M. Kunert, W. Minker, and C. Waldschmidt. Antenna and Signal Path Calibration of an Experimental MIMO Radar Prototype, 2016.
- [FOTa] Fundamentals of Transportation / Grade. [Online]. Available: Fundamentals of Transportation / Grade.
- [FOTb] Fundamentals of Transportation / Vertical Curves. [Online]. Available: Fundamentals of Transportation / Vertical Curves.
- [GDDM14] R. Girshick, J. Donahue, T. Darrell, and J. Malik. Rich Feature Hierarchies for Accurate Object Detection and Semantic Segmentation. In *IEEE Conference on Computer Vision and Pattern Recognition*, pages 580–587, Columbus, OH, USA, Jun. 2014.
- [Gir15] R. Girshick. Fast R-CNN. In *IEEE International Conference on Computer Vision (ICCV)*, pages 1440–1448, Santiago, Chile, Dec. 2015.
- [GLM⁺01] P. Griffiths, D. Langer, J. A. Misener, M. Siegel, and C. Thorpe. Sensor-friendly Vehicle and Roadway System. In *Proc. IEEE Instrumentation and Measurement Technology Conference*, pages 1036–1040, Budapest, Hungary, Aug. 2001.
- [HK03] J. Hernandez and C.-Y. Kuo. Steering Control of Automated Vehicles Using Absolute Positioning GPS and Magnetic Markers. *IEEE Tran. on Vehicular Technology*, 52(1):150–161, 2003.
- [IC15] S. Ioffe and S. Christian. Batch Normalization: Accelerating Deep Network Training by Reducing Internal Covariate Shift. In *Proc. of the 32nd International Conference on Machine Learning*, pages 1–11, Lille, France, Mar. 2015.
- [ITS⁺09] A. Isogai, K. Takagi, R. Schubert, E. Richter, and P. Lindner. Lidar Based Lane Recognition. In *Proc. 16th ITS World Congress and Exhibition on Intelligent Transport Systems and Services*, pages 4569–4576, Stockholm, Sweden, Sep. 2009.
- [JA17] R. Joseph and F. Ali. YOLO9000: Better, Faster, Stronger. In *IEEE Conference on Computer Vision and Pattern Recognition (CVPR)*, pages 6517–6525, Honolulu, HI, USA, Jul. 2017.

- [KB15] D. P. Kingma and J. L. Ba. ADAM: A Method for Stochastic Optimization. In *International Conference on Learning Representations*, pages 1–15, San Diego, CA, USA, May 2015.
- [KP17] R. S. Kulikov and A. I. Perov. Navigation of Vehicle in Urban Canyon via Two-satellite GNSS and Map Aiding. In *Dynamics of Systems, Mechanisms and Machines (Dynamics)*, pages 1–7, Omsk, Russia, Nov. 2017.
- [KSH12] A. Krizhevsky, I. Sutskever, and G. E. Hinton. ImageNet Classification with Deep Convolutional Neural Networks. *Communications of the ACM*, 60(6):84–90, 2012.
- [LLMHW17] J. Lombacher, K. Lautdt, J. Dickmann M. Hahn, and C. Wählher. Semantic Radar Grids. In *IEEE Intelligent Vehicles Symposium (IV)*, pages 1170–1175, Los Angeles, CA, USA, Jun. 2017.
- [MH96] B. Money and G. Hodgson. *Manual of Contract Documents for Highway Work - a User's Guide and Commentary*. Thomas Telford, 1996.
- [MSK15] F. Meinl, E. Schubert, and M. Kunert. Realtime FPGA-based Processing Unit for a High-resolution Automotive MIMO Radar Platform. In *European Radar Conference (EuRAD)*, pages 213–216, Paris, France, Dec. 2015.
- [MSK17] F. Meinl, M. Stolz, and M. Kunert. An Experimental High Performance Radar System for Highly Automated Driving. In *IEEE MTT-S International Conference on Microwaves for Intelligent Mobility (ICMIM)*, pages 71–74, Nagoya, Japan, Mar. 2017.
- [MWS16] W. McCarthy, K. H. White, and G. Sill. Pavement Marking Tape Incorporating Advanced Materials for Improved Visibility. Jul. 2016. USA Patent US2016/0209559A1.
- [NU17] H. Nakamura and K. Ushiro. Development and Verification of a Lane Marker Detection System in All-Weather Conditions. In *JARI Research Journal*, pages 1–6, Japan, Feb. 2017.
- [oSHO04] American Association of State Highway and Transportation Officials. A Policy on Geometric Design of Highways and Streets, 2004.

- [OT06] T. Ogawa and K. Takagi. Lane Recognition Using On-Vehicle LIDAR. In *Proc. IEEE Intelligent Vehicles Symposium*, pages 540–545, Tokyo, Japan, Jun. 2006.
- [oT14] Massachusetts Institute of Technology. Vehicle Localization Using Surface Penetrating Radar. May 2014. USA Patent US2014/0121964A1.
- [PKK⁺15] G. Protzmann, J. Kiwitt, D. Kiefer, G. Schmitt, M. Kaufmann, and M. Olapoju. New Type of Road Markings for Supporting the Environment Detection of Vehicles. Sep. 2015. USA Patent US2015/0247297A1.
- [QSKG17] C. R. Qi, H. Su, M. Kaichun, and L. J. Guibas. PointNet: Deep Learning on Point Sets for 3D Classification and Segmentation. In *IEEE Conference on Computer Vision and Pattern Recognition (CVPR)*, pages 77–85, Honolulu, HI, USA, Jul. 2017.
- [QYSG17] Charles Ruizhongtai Qi, Li Yi, Hao Su, and Leonidas J. Guibas. Pointnet++: Deep hierarchical feature learning on point sets in a metric space. In *NIPS*, 2017.
- [RDGF16] J. Redmon, S. Divvala, R. Girshick, and A. Farhadi. You Only Look Once: Unified, Real-Time Object Detection. In *IEEE Conference on Computer Vision and Pattern Recognition (CVPR)*, pages 779–788, Las Vegas, NV, USA, Jun. 2016.
- [RF18] Joseph Redmon and Ali Farhadi. Yolov3: An incremental improvement. *arXiv*, 2018.
- [RHG17] S. Ren, K. He, and R. Girshick. Faster R-CNN: Towards Real-Time Object Detection with Region Proposal Networks. *IEEE Tran. on Pattern Analysis and Machine Intelligence*, 39(6):1137–1149, 2017.
- [Ric05] M. A. Richards. *Fundamentals of Radar Signal Processing*. McGraw-Hill, 2005.
- [Ruc70] George T Ruck. *Radar Cross Section Handbook*. Plenum Press, 1970.
- [SAC05] D. Schreiber, B. Alefs, and M. Clabian. Single Camera Lane Detection and Tracking. In *Proc. IEEE Intelligent Transportation Systems*, pages 1114–1119, Vienna, Austria, Sep. 2005.

- [SHDW18] Ole Schumann, Markus Hahn, Jürgen Dickmann, and Christian Wöhler. Semantic segmentation on radar point clouds. *2018 21st International Conference on Information Fusion (FUSION)*, pages 2179–2186, 2018.
- [SLD16] E. Shelhamer, J. Long, and T. Darrell. Fully Convolutional Networks for Semantic Segmentation. *IEEE Tran. on Pattern Analysis and Machine Intelligence*, 39:640–651, 2016.
- [SWM⁺18] M. Stolz, M. Wolf, F. Meinl, M. Kunert, and W. Menzel. A New Antenna Array and Signal Processing Concept for an Automotive 4D Radar. In *15th European Radar Conference (EuRAD)*, pages 63–66, Madrid, Spain, Sep. 2018.
- [TMBP09] R. Toledo-Moreo, D. Betaille, and F. Peyret. Fusing GNSS, Dead-reckoning, and Enhanced Maps for Road Vehicle Lane-level Navigation. *IEEE Journal of Selected Topics in Signal Processing*, 3(5):798–809, 2009.
- [VHJW] Alexey Voronov, Johan Hultén, and Cristofer Englund Johan Wedlin. Radar Reflecting Pavement Markers for Vehicle Automation. [Online]. Available: <https://ri.diva-portal.org/smash/get/diva2:1132434/FULLTEXT02.pdf>.
- [WR87] W. Wiesbeck and S. Riegger. Measurement of The Complex RCS-matrix for Small Metallic and Dielectric Objects. In *Proc. International Conference, RADAR 87*, pages 360–364, London, England, Oct. 1987.
- [Yau13] Kin Shing Bobby Yau. Development of a Passive Retrodirective Van Atta Array Reflector at X-band. In *International Conference on Radar*, pages 1097–5764, Adelaide, SA, Australia, Sep. 2013.

Own publications

Journal publications

- [1] Z. Feng, M. Li, M. Stolz, M. Kunert, and W. Wiesbeck. Lane Detection with a High-resolution Automotive Radar by Introducing a New Type of Road Marking. *IEEE Trans. on Intelligent Transportation Systems*, 0(0-0):1–18, 2018.

Conference publications

- [2] Z. Feng, M. Stolz, M. Li, M. Kunert, and W. Wiesbeck. Verification of a lane detection method with automotive radar based on a new type of road marking. In *IEEE International Conference on Microwaves for Intelligent Mobility (ICMIM)*, pages 1–4, Munich, Germany, April 2018.
- [3] Z. Feng, S. Zhang, M. Kunert, and W. Wiesbeck. Applying neural networks with a high-resolution automotive radar for lane detection. In *Automotive meets Electronics (AmE)*, pages 1–6, Dortmund, Germany, March 2019.
- [4] Z. Feng, S. Zhang, M. Kunert, and W. Wiesbeck. Point Cloud Segmentation with a High-Resolution Automotive Radar. In *Automotive meets Electronics (AmE)*, pages 1–5, Dortmund, Germany, March 2019.
- [5] M. Li, Z. Feng, M. Stolz, M. Kunert, R. Henze, and F. Küçükay. High resolution radar-based occupancy grid mapping and free space detection. In *4th International Conference on Vehicle Technology and Intelligent Transport Systems (VEHITS)*, pages 1–12, Funchal, Portugal, March 2018.
- [6] M. Li, Z. Feng, M. Stolz, M. Kunert, R. Henze, and F. Küçükay. Static Environment Perception Based on High-Resolution Automotive Radars. *Smart Cities, Green Technologies, and Intelligent Transport Systems*, 0(0-0):1–25, 2018.

- [7] M. Li, M. Stolz, Z. Feng, M. Kunert, R. Henze, and F. Küçükay. An adaptive 3d grid-based clustering algorithm for automotive high resolution radar sensor. In *IEEE International Conference on Vehicular Electronics and Safety*, pages 1–7, Madrid, Spain, September 2018.
- [8] M. Stolz, M. Li, Z. Feng, M. Kunert, and W. Menzel. Direction of movement estimation of cyclists with a high-resolution automotive radar. In *IEEE MTT-S International Conference on Microwaves for Intelligent Mobility (ICMIM)*, pages 1–4, Munich, Germany, April 2018.
- [9] M. Stolz, M. Li, Z. Feng, M. Kunert, and W. Menzel. High resolution automotive radar data clustering with novel cluster method. In *IEEE Radar Conference*, pages 164–168, Oklahoma City, USA, April 2018.